

# Climate-Triggered Drought as Causes for Different Degradation Types of Natural Forests: A Multitemporal Remote Sensing Analysis in NE Iran

Dissertation for awarding the academic degree

Doctor of Engineering (Dr.-Ing.)

Submitted by:

M.Sc. Omid Abdi

born on 24 August 1981 in Mahabad, Iran

Supervisors:

Prof. Dr. Manfred F. Buchroithner, Technische Universität Dresden

Prof. Dr. Elmar Csaplovics, Technische Universität Dresden

Prof. Dr. Mathias Schardt, Technische Universität Graz

Dresden, 28 May 2020



# Erklärung des Promovenden

---

Die Übereinstimmung dieses Exemplars mit dem Original der Dissertation zum Thema:

**“Climate-Triggered Drought as Causes for Different Degradation Types of Natural Forests: A Multitemporal Remote Sensing Analysis in NE Iran”**

wird hiermit bestätigt.

.....  
Ort, Datum

.....  
Unterschrift





# Abstract

---

Climate-triggered forest disturbances are increasing either by drought or by other climate extremes. Droughts can change the structure and function of forests in long-term or cause large-scale disturbances such as tree mortality, forest fires and insect outbreaks in short-term. Traditional approaches such as dendroclimatological surveys could retrieve the long-term responses of forest trees to drought conditions; however, they are restricted to individual trees or local forest stands. Therefore, multitemporal satellite-based approaches are progressing for holistic assessment of climate-induced forest responses from regional to global scales. However, little information exists on the efficiency of satellite data for analyzing the effects of droughts in different forest biomes and further studies on the analysis of approaches and large-scale disturbances of droughts are required. This research was accomplished for assessing satellite-derived physiological responses of the Caspian Hyrcanian broadleaves forests to climate-triggered droughts from regional to large scales in northeast Iran.

The 16-day physiological anomalies of rangelands and forests were analysed using MODIS-derived indices concerning water content deficit and greenness loss, and their variations were spatially assessed with monthly and inter-seasonal precipitation anomalies from 2000 to 2016. Specifically, dimensions of forest droughts were evaluated in relations with the dimensions of meteorological and hydrological droughts. Large-scale effects of droughts were explored in terms of tree mortality, insect outbreaks, and forest fires using field observations, multitemporal Landsat and TerraClimate data. Various approaches were evaluated to explore forest responses to climate hazards such as traditional regression models, spatial autocorrelations, spatial regression models, and panel data models.

Key findings revealed that rangelands' anomalies did show positive responses to monthly and inter-seasonal precipitation anomalies. However, forests' droughts were highly associated with increases in temperatures and evapotranspiration and were slightly associated with the decreases in precipitation and surface water level. The hazard intensity of droughts has affected the water content of forests higher than their greenness properties. The stages of moderate to extreme dieback of trees were significantly associated with the hazard

intensity of the deficit of forests' water content. However, the stage of severe defoliation was only associated with the hazard intensity of forests' greenness loss. Climate hazards significantly triggered insect outbreaks and forest fires. Although maximum temperatures, precipitation deficit, availability of soil moisture and forest fires of the previous year could significantly trigger insect outbreaks, the maximum temperatures were the only significant triggers of forest fires from 2010–2017. In addition to climate factors, environmental and anthropogenic factors could control fire severity during a dry season.

The overall evaluation indicated the evidence of spatial associations between satellite-derived forest disturbances and climate hazards. Future studies are required to apply the approaches that could handle big-data, use the satellite data that have finer wavelengths for large-scale mapping of forest disturbances, and discriminate climate-induced forest disturbances from those that induced by other biotic and abiotic agents.

# Kurzfassung

---

Klimabedingte Waldstörungen nehmen entweder durch Dürre oder durch andere Klimaextreme zu. Dürren können langfristig die Struktur und Funktion der Wälder verändern oder kurzfristig große Störungen wie Baumsterben, Waldbrände und Insektenausbrüche verursachen. Traditionelle Ansätze wie dendroklimatologische Untersuchungen könnten die langfristigen Reaktionen von Waldbäumen auf Dürrebedingungen aufzeigen, sie sind aber auf einzelne Bäume oder lokale Waldbestände beschränkt. Daher werden multitemporale satellitengestützte Ansätze zur ganzheitlichen Bewertung von klimabedingten Waldreaktionen auf regionaler bis globaler Ebene weiterentwickelt. Es gibt jedoch nur wenige Informationen über die Effizienz von Satellitendaten zur Analyse der Auswirkungen von Dürren in verschiedenen Waldbiotopen. Daher sind weitere Studien zur Analyse von Ansätzen und großräumigen Störungen von Dürren erforderlich. Diese Forschung wurde durchgeführt, um die aus Satellitendaten gewonnenen physiologischen Reaktionen der im Nordosten Irans gelegenen kaspischen hyrkanischen Laubwälder auf klimabedingte Dürren auf lokaler und regionaler Ebene zu bewerten.

Auf der Grundlage der aus MODIS-Daten abgeleiteten Indizes wurden die 16-tägigen physiologischen Anomalien von Weideland und Wäldern in Bezug auf Wassergehaltsdefizit und Grünverlust analysiert und ihre Variationen räumlich mit monatlichen und intersaisonalen Niederschlagsanomalien von 2000 bis 2016 bewertet. Insbesondere wurden die Dimensionen der Walddürre in Verbindung mit den Dimensionen der meteorologischen und hydrologischen Dürre bewertet. Großräumige Auswirkungen von Dürren wurden in Bezug auf Baumsterblichkeit, Insektenausbrüche und Waldbrände mit Hilfe von Feldbeobachtungen, multitemporalen Landsat- und TerraClimate Daten untersucht. Verschiedene Ansätze wurden ausgewertet, um Waldreaktionen auf Klimagefahren wie traditionelle Regressionsmodelle, räumliche Autokorrelationen, räumliche Regressionsmodelle und Paneldatenmodelle zu untersuchen.

Die wichtigsten Ergebnisse zeigten, dass die Anomalien von Weideland positive Reaktionen auf monatliche und intersaisonale Niederschlagsanomalien aufweisen. Die

Dürren in den Wäldern waren jedoch in hohem Maße mit Temperaturerhöhungen und Evapotranspiration verbunden und standen in geringem Zusammenhang mit dem Rückgang von Niederschlägen und des Oberflächenwasserspiegels. Die Gefährdungsintensität von Dürren hat den Wassergehalt von Wäldern stärker beeinflusst als die Eigenschaften ihres Blattgrüns. Die Stufen mittlerer bis extremer Baumsterblichkeit waren signifikant mit der Gefährdungsintensität des Defizits des Wassergehalts der Wälder verbunden. Das Ausmaß der starken Entlaubung hing jedoch nur mit der Gefährdungsintensität des Grünverlustes der Wälder zusammen. Die Klimagefahren haben zu deutlichen Insektenausbrüchen und Waldbränden geführt. Obwohl Maximaltemperaturen, Niederschlagsdefizite, fehlende Bodenfeuchte und Waldbrände des Vorjahres deutlich Insektenausbrüche auslösen konnten, waren die Maximaltemperaturen die einzigen signifikanten Auslöser von Waldbränden von 2010 bis 2017. Neben den Klimafaktoren können auch umweltbedingte und anthropogene Faktoren den Schweregrad eines Brandes während einer Trockenzeit beeinflussen.

Die Gesamtbewertung zeigt Hinweise auf räumliche Zusammenhänge zwischen aus Satellitendaten abgeleiteten Waldstörungen und Klimagefahren. Weitere Untersuchungen sind erforderlich, um Ansätze anzuwenden, die mit großen Datenmengen umgehen können, die Satellitendaten in einer hohen spektralen Auflösung für die großmaßstäbige Kartierung von Waldstörungen verwenden und die klimabedingte Waldstörungen von denen zu unterscheiden, die durch andere biotische und abiotische Faktoren verursacht werden.

# Acknowledgements

---

The output of this dissertation was influenced by many people who have been very helpful during my doctoral study in Dresden. I would particularly like to thank the following people and institutions:

- Prof. Manfred F. Buchroithner for giving me the opportunity to accomplish this research, for his incredible support, and all confidence, knowledge and scientific experiences towards me.
- Prof. Elmar Csaplovics and Prof. Mathias Schardt for their constructive comments during the process of reviewing my dissertation.
- Prof. Dirk Burghardt and colleagues at the Institute of Cartography, particularly to Mrs Steffi Sharma and Mrs Doris Salomon for taking care of my administrative works with full of ease.
- Mrs Zeinab Shirvani for her great collaboration and patient. I obtained fruitful experiences in working with Zeinab on our joint publications.
- Mr Thomas Gründemann for editing the German Abstract of this dissertation.
- Gesellschaft von Freunden und Förderern der TU Dresden e. V. and Graduate Academy TU Dresden for their financial support of some parts of my doctoral studies.
- The Department of Natural Resources and Watershed Management of Golestan Province, Iran for providing some base data and information during this research.
- My family for their unstinting support during all stages of my life, especially during my doctoral studies in Germany.



# Table of Contents

---

<b>Erklärung des Promovenden .....</b>	<b>III</b>
<b>Abstract .....</b>	<b>V</b>
<b>Kurzfassung .....</b>	<b>VII</b>
<b>Acknowledgments .....</b>	<b>IX</b>
<b>Table of Contents .....</b>	<b>XI</b>
<b>List of Figures .....</b>	<b>XV</b>
<b>List of Tables.....</b>	<b>XXI</b>
<b>List of Abbreviations.....</b>	<b>XXIII</b>
<b>1. Introduction.....</b>	<b>1</b>
1.1 Motivation.....	1
1.2 Time series analysis of earth observation satellites.....	2
1.2.1 Sensors .....	2
1.2.2 Variables.....	3
1.2.3 Components .....	3
1.3 Classification of droughts .....	3
1.4 Drought dimensions .....	4
1.5 Remote sensing of drought.....	4
1.6 Forest degradation and climate-triggered drought .....	5
1.7 Hyrcanian forests .....	7
1.8 Objectives .....	9
1.9 Overview of the dissertation .....	10
<b>2. Spatial-Statistical Analysis of Factors Determining Forest Fires: A Case Study from Golestan, Northeast Iran.....</b>	<b>13</b>
2.1 Abstract.....	14
2.2 Introduction .....	14
2.3 Materials and Methods.....	17
2.3.1 Study area .....	17
2.3.2 Digital fire data.....	18

2.3.3 Digital map data .....	19
2.3.4 Methods.....	19
2.3.4.1 Spatial analysis .....	19
2.3.4.2 Statistical analysis .....	20
2.4 Results and discussion .....	21
2.5 Conclusions.....	30
Acknowledgements .....	30
<b>3. Spatiotemporal Drought Evaluation of Hyrcanian Deciduous Forests and Semi-Steppe Rangelands Using Moderate Resolution Imaging Spectroradiometer Time Series in Northeast Iran .....</b>	<b>31</b>
3.1 Abstract.....	32
3.2 Introduction .....	32
3.3 Materials and Methods.....	35
3.3.1 Study area description .....	35
3.3.2 Vegetation Indices (VIs).....	37
3.3.3 Estimation of precipitation by Kriging .....	37
3.3.4 Excluding pixels subject to anthropogenic activities.....	39
3.3.5 Spatiotemporal analysis of vegetation and precipitation anomalies .....	40
3.3.6 Spatial relationships between VIs and SPI .....	41
3.4 Results.....	42
3.4.1 Spatiotemporal patterns of precipitation anomalies.....	42
3.4.2 Spatiotemporal patterns of vegetation indices .....	44
3.4.3 Spatial relationships between drought and the anomalies of MODIS VIs .....	47
3.4.3.1 Inter-seasonal relationships .....	47
3.4.3.2 Monthly relationships .....	49
3.5 Discussion .....	51
3.6 Conclusion .....	57
Acknowledgements .....	58
<b>4. Forest Drought-Induced Diversity of Hyrcanian Individual-Tree Mortality Affected by Meteorological and Hydrological Droughts by Analyzing Moderate Resolution Imaging Spectroradiometer Products and Spatial Autoregressive Models over Northeast Iran.....</b>	<b>59</b>
4.1 Abstract.....	60
4.2 Introduction .....	60
4.3 Overview of the Study Area.....	64
4.4 Data and Methodology .....	64



4.4.1 Meteorological and hydrological anomalies .....	64
4.4.2 Forest anomalies.....	66
4.4.3 Features of droughts .....	67
4.4.4 Drought hazard intensity .....	67
4.4.5 Surveying of individual-tree mortality.....	68
4.4.6 Diversity index of individual-tree mortality .....	68
4.4.7 Spatial autoregressive between drought hazards and diversity of individual-tree mortality .....	69
4.5 Results.....	70
4.5.1 Drought dimensions .....	70
4.5.1.1 Meteorological drought.....	70
4.5.1.2 Hydrological drought.....	70
4.5.1.3 Forest drought .....	70
4.5.2 Spatial variations of drought hazard intensity (DHI).....	71
4.5.3 Diversity of individual-tree mortality .....	72
4.5.4 Spatial dependence between the hazard intensity of forest droughts with meteorological and hydrological droughts .....	72
4.5.5 Spatial dependence between the diversity of individual-tree mortality and forest droughts .....	74
4.6 Discussion .....	75
4.7 Conclusion .....	80
Acknowledgements .....	81
<b>5. Climate-Triggered Insect Defoliators and Forest Fires Using Multitemporal Landsat and TerraClimate Data in NE Iran: An Application of GEOBIA TreeNet and Panel Data Analysis .....</b>	<b>83</b>
5.1 Abstract.....	84
5.2 Introduction .....	84
5.3 Materials and Methods.....	87
5.3.1 Study area .....	87
5.3.2 Data and field mensuration .....	88
5.3.3 Methodology .....	89
5.3.3.1 TreeNet-based insect-infestation mapping .....	89
5.3.3.2 Intensity of insect infestation, the severity of forest fire, and climate hazards .....	91
5.3.3.3 Relationships of insect infestation, forest fires and climate hazards .....	92
Panel data models.....	92
Testing for fixed effects and random effects .....	93

5.4 Results.....	94
5.4.1 <i>Insect defoliation mapping</i> .....	94
5.4.2. <i>Insect infestation, forest fires and climate hazards modelling</i> .....	96
5.5 Discussion .....	98
5.6 Conclusions.....	101
Acknowledgements .....	102
<b>6. Conclusions and Outlook</b> .....	103
6.1 Concluding remarks .....	103
6.2 Outlook.....	104
<b>References</b> .....	107
<b>Appendix A</b> .....	129
<b>Appendix B</b> .....	137

# List of Figures

---

Figure 1.1 The locations of Hyrcanian ecoregion in the Eurasian temperate broadleaf forests (a), Golestan Province in the Hyrcanian ecoregion (b), and the distribution of forests and rangelands in three studied basins including Atrak, Qare-sou and Gorganrood (c).....	8
Figure 1.2 A Hyrcanian forest stand (a) and an individual tree (b) attacked by insect defoliators in NE Iran in 2014.....	9
Figure 2.1 The distribution of towns and villages, paved roads, dirt roads and forest roads in Northeast Iran.....	18
Figure 2.2 The logistic model between burned area and duration of fire in Northeast Iran. .	22
Figure 2.3 Cumulative days of fire occurrence against burnt area (cumulative days calculated based on cumulative hours of forest fire occurrence in all burnt areas divided by 24 to convert it to the daily).....	22
Figure 2.4 The spatial relationship between daily mean wind speed and burnt areas in Northeast Iran.....	24
Figure 2.5 The spatial relationship between daily mean temperature and burnt areas in Northeast Iran.....	25
Figure 2.6 Burnt areas that show overlaps with forest road network coverage and outside of it.....	26
Figure 2.7 Burnt areas and fire spreading patterns in the study area. Forest density was based on NDVI.....	27
Figure 2.8 Susceptibility map based on the duration of forest fires in Northeast Iran. ....	28
Figure 2.9 Susceptibility map based on the spread of forest fire in Northeast Iran. ....	29
Figure 3.1 Location of the Hyrcanian forests and Atrak, Gorganrood and Qare-sou watersheds (a) and distribution of land cover types as well as degraded vegetation (b) in the northeast of Iran. ....	36
Figure 3.2 The proportion of the forests (a) and rangelands (b) affected by different drought schemes compared to the long-term precipitation anomalies during the growing season of	

2000-2016 (b), and four periods of severe droughts in 2001(c), 2008(d), 2011(e), and 2014 (f), respectively over the spatial extent of Northeast Iran. ....	43
Figure 3.3 Time-series distribution of proportion areas of the vegetation greenness anomalies calculated by the enhanced vegetation index (EVI; a, b) and the normalized difference vegetation index (NDVI; c, d), and the vegetation water anomalies calculated by the normalized difference water index (NDWI; e, f) from 2000 to 2016. ....	44
Figure 3.4 Distribution of vegetation greenness anomalies during the growing seasons calculated by the enhanced vegetation index (EVI) for drought periods in the forests and rangelands (a). Distribution of vegetation greenness anomalies during the growing seasons calculated by the normalized difference vegetation index (NDVI) for drought periods in the forests and rangelands (b). Distribution of the vegetation water anomalies during the growing season calculated by the normalized difference water index (NDWI) anomalies for drought periods in the forests and rangelands (c).....	46
Figure 3.5 The spatial extent of the severe dates of vegetation anomalies measured by the enhanced vegetation index (EVI), the normalized difference vegetation index (NDVI), and the normalized difference water index (NDWI). ....	48
Figure 3.6 Distribution of spatial correlation (Moran's <i>I</i> ) between the standardized precipitation index and the vegetation indices EVI, NDVI, and NDWI in the forests (a) and rangelands (b) during the growing season from 2000 to 2016, and DOYs (c and d) for drought conditions. ...	50
Figure 3.7 Spatial variations of local <i>Morans'I</i> values, BiLISA significance levels and BiLISA cluster/outlier (significance level: 0.05 and randomization permutation: 499) of some DOYs with the high spatial relation between the anomalies of rainfall and the vegetation indices during drought periods. EVI: enhanced vegetation index; NDVI: normalized difference vegetation index; NDWI: normalized difference water index. ....	52
Figure 3.8 The land surface temperature (LST) anomalies in the forest lands during 2011 (a) and 2014 (b) droughts.....	53
Figure 3.9 Aggregated maps of BiLISA for clusters (High-high and Low-low) during growing seasons (March to October) of forests and rangelands based on the qualified vegetation indices for drought periods. EVI: enhanced vegetation index; NDVI: normalized difference vegetation index; NDWI: normalized difference water index. ....	56

Figure 4.1 Spatial location of the study area in the Hyrcanian forests (a), tree species types (b), an example of scattering of tree species dieback-samples in one parcel out of 100 selected parcels (c), and distribution the total studied parcels (1162) for exploring the stress of the forest types and the selected parcels (100) for the sampling of tree mortality, and the forest biomes types in northeastern Iran (d)..... 65

Figure 4.2 Drought hazard intensity is a combination of the severity, frequency and duration of drought events for each year. The median values of the periods are used as the final hazard intensity of the meteorological droughts: the precipitation (a), day-time land surface temperature (b), night-time land surface temperature (c) and actual evapotranspiration (d); hydrological droughts: the surface water (e) and groundwater (f) levels; forest droughts: the deficit of forest water-content (g) and loss of forest greenness (h) in northeastern Iran. Although the average values of the hazard intensity of meteorological droughts are greater than the hydrological droughts, the hazard intensity values of forest droughts are considerable throughout the study area..... 71

Figure 4.3 Spatial distribution of diversity of the tree species diebacks measured using Simpson’s diversity index for the four dieback stages in the studied parcels of three zones in northeastern Iran..... 73

Figure 4.4 Fluctuation in water-table elevation relative to establishing the date of assessment network in northeastern Iran from 1973 to 2016..... 78

Figure 4.5 The sensitivity of some forest types to the intensity of forest drought hazards retrieved from the NDVI (a, c and e) and NDWI (b, d, and f) in the western (zone I), middle (zone II) and eastern (zone III) of northeastern Iran. .... 79

Figure 5.1 Study area in the Hyrcanian forest ecoregion in the southeast Caspian Sea. Spatial scatter of the insect defoliators and forest fires samples of 2012–2017 in the northeast (NE) Iran. The eastern part of the study area was affected by *Lymantria dispar*, while the western area was affected by *Erannis defoliaria* and *Operophtera brumata*. .... 88

Figure 5.2 Site C (Figure 5.1): The images of Google Earth (GE) and Landsat 5 TM (SWR, NIR, R) show that the forest was in a healthy condition before the attack of *Lymantria dispar* in 2010 (a, b); the symptoms of the infestation emerged on the Landsat 8 OLI (SWR1, NIR, R) as “olivenite

green” in 2013 (c); the insect significantly infested the region based on the GE (d) and Landsat 8 OLI (e) images in 2014, while it declined in 2015 (f) and ended in 2016 (g).....	89
Figure 5.3 The importance of top predictor variables of Landsat 8 OLI and ancillary features for discerning insect-infested from the non-insect-infested objects using TreeNet. The most important predictor variable (i.e., the mean of the second principal component, or PC2) has gained a value of 100%, and other features were rescaled based on their importance relative to the PC2. ....	95
Figure 5.4 Univariate partial dependency graphs for the top five-predictor variables for classification of insect-infested forests in NE Iran. Positive values of the outputs indicate a direct association of a class of the categorical variables or values of the continuous variables with the focus class. Eight tree species show positive relationships with the infested class (a), the mean of PC2 and the mean of red band derived from GLCM show a positive association at values of greater than 0.711 (b) and 126.30 (c), and the mean values of the NDWI and GEMI show a positive relationship with the presence of infestation until the values of 0.267 (d) and 0.697 (e). ....	95
Figure 5.5 The insect-affected and non-insect-affected forest-objects derived from the influential object features of Landsat 8 OLI and ancillary data using Geographic Object-Based Image Analysis (GEOBIA) and TreeNet in the Hyrcanian region, NE Iran. ....	96
Figure 5.6 The yearly hazard intensity of defoliation for the time period of 2010 to 2017 (a–h) within the insect-infested forest objects. The monthly anomalies of NDWI were obtained from the time series of Landsat 5, 7, and 8 from 1987 to 2017. The dimensions of forest water content deficit including severity, frequency, and duration were derived from Landsat–NDWI anomalies for the time period of defoliation (2010–2017). The values of these dimensions were standardized by the membership functions of fuzzy linear and fuzzy large between zero and one. The hazard intensity of defoliation was obtained by overlaying the standardized layers of dimensions of the NDWI anomalies using the fuzzy gamma operator within the insect-infested segment objects during a growing season in Hyrcanian forests, NE Iran.....	97
Figure 3.S1 Spatial variations of BiLISA cluster/ outlier of DOY 65 to DOY 113 during drought periods (Significance level= 0.05, Randomization permutations= 499).....	132
Figure 3.S2 Spatial variations of BiLISA cluster/ outlier of DOY 129 to DOY 177 during drought periods (Significance level= 0.05, Randomization permutations= 499).....	133

Figure 3.S3 Spatial variations of BiLISA cluster/ outlier of DOY 193 to DOY 241 during drought periods (Significance level= 0.05, Randomization permutations= 499).....	134
Figure 3.S4 Spatial variations of BiLISA cluster/ outlier of DOY 257 to DOY 305 during drought periods (Significance level= 0.05, Randomization permutations= 499).....	135
Figure 4.S1 Spatial variations of the drought severity show that the higher values of negative anomalies are observed in the ETa (d), night-time LST (c), day-time LST (b) and the precipitation (a) among meteorological variables. The water surface anomaly (e) recorded higher negative values in comparison to the groundwater anomaly (f). Forest drought based on the normalized difference water index (NDWI) (g) was severe than forest drought based on the normalized difference vegetation index (NDVI) (h) in northeastern Iran.....	138
Figure 4.S2 Spatial variations of the drought frequency of the meteorological droughts: the precipitation (P) (a), day-time LST (DLST) (b), night-time LST (NLST) (c), and the ETa (d); the hydrological droughts: the surface water (SW) (e) and groundwater (GW) (f) levels; and the forest droughts: the deficit of water-content (NDWI) (g) and loss of the greenness (NDVI) (h) during a hydrological year (from October of the previous year to September of the current year/ growing season (March–October) in northeastern Iran.....	138
Figure 4.S3 Spatial variations of the drought duration of the meteorological droughts: the precipitation (P) (a), day-time LST (DLST) (b), night-time LST (NLST) (c), and the ETa (d); the hydrological droughts: the surface water (SW) (e) and groundwater (GW) (f) levels; and the forest droughts: the deficit of water-content (NDWI) (g) and loss of the greenness (NDVI) (h) during a hydrological year (from October of the previous year to September of the current year/ growing season (March–October) in northeastern Iran.....	139





# List of Tables

---

Table 2.1 Statistics of forest fires that were occurred in Northeast Iran from 2001 to 2010. ....	15
Table 2.2 Environmental, climatic, and anthropogenic parameters used as factors affecting the occurrence and durability of forest fires.....	20
Table 2.3 Stepwise regression results depending on the factors affecting forest fire occurrence in Northeast Iran. ....	23
Table 2.4 Statistics of climatic parameters during times of forest fires compared with long-term data (1980--2010) in Northeast Iran. ....	23
Table 3.1 Obtained averages of <i>Moran's I</i> values between monthly rainfall anomalies (SPI) and 16-day VI anomalies (EVI, NDVI and NDWI) for the forest areas (a) and rangelands (b). ....	51
Table 4.1 The model coefficients and the parameters of model fit resulting from the spatial relationships between the hazard intensity of forest droughts, based on water-content (NDWI) and greenness (NDVI) properties, with the hazard intensity of the meteorological (precipitation, day-time LST, night-time LST and actual evapotranspiration) and hydrological (surface water and groundwater levels) droughts in northeastern Iran.....	74
Table 4.2 The model coefficients and the parameters of model fit resulting from the spatial relationships between the diversity of tree species mortality and the hazard intensity of forest droughts retrieved from the NDWI and the NDVI within four stages of diebacks in northeastern Iran.....	75
Table 5.1 Object features derived from Landsat 8 OLI channels and ancillary data (topographic and forest data) for discriminating defoliated forests from healthy forests in NE Iran.....	90
Table 5.2 Classification correctness of test samples for the TreeNet analysis to discriminate the insect-infested from the non-insect-infested forests in NE Iran.....	94
Table 5.3 Results of panel data models for relationships between the intensity of insect infestation with the intensity of climate hazards of the current year and previous year as well as forest fires of the previous year in NE Iran.....	98

Table 5.4 Results of panel data models for relationships between the severity of forest fires with the intensity of climate hazards and insect infestation of the current year and the previous year in NE Iran. ....	98
Table 3.S1 Cross-validation of monthly precipitation estimation based on the different semi-variogram models from rain gauges from 1987 to 2016. ....	130
Table 4.S1 Classification schemes of meteorological and hydrological droughts, and forest stress based on the first standard deviation. ....	137
Table 4.S2 The values of test parameters for diagnosing of spatial dependence of regression models. ....	137

# List of Abbreviations

---

AIC	Akaike Info Criterion
ARVI	Atmospherically Resistant Vegetation Index
AVHRR	Advanced Very High Resolution Radiometer
BiLISA	Bivariate Local Indicators of Spatial Association
<i>D</i>	Simpson's Diversity Index
DEM	Digital Elevation Model
DHI	Drought Hazard Intensity
dNBR	differenced Normalized Burn Ratio
DNRWM	Department of Natural Resources and Watershed Management
DOY	Day of Year
EBK	Empirical Bayesian Kriging
ETa	Actual Evapotranspiration
EVI	Enhanced Vegetation Index
FMPs	Forest Management Plans
FSI	Fire Susceptibility Index
GE	Google Earth
GEMI	Global Environment Monitoring Index
GEOBIA	Geographic Object-Based Image Analysis
GIS	Geographic Information Systems
GLCM	Grey-Level Co-occurrence Matrix
GLS	Generalized Least Squares
GPS	Global Positioning System
GVI	Green Vegetation Index
IPVI	Infrared Percentage Vegetation Index

LI	Log Likelihood
LM	Lagrange Multiplier
LOK	Lognormal Ordinary Kriging
LP DAAC	Land Processes Distributed Active Archive Center
LST	Land Surface Temperature
LSWI	Land Surface Water Index
MASL	Metres Above Sea Level
<i>ME</i>	Mean Error
MetOp	Meteorological Operational Satellites
MODIS	Moderate Resolution Imaging Spectroradiometer
MSI	Moisture Stress Index
MSPE	Mean Squared Prediction Errors
NDDI	Normalized Difference Drought Index
NDIib6	Normalized Difference Infrared Index-band 6
NDIib7	Normalized Difference Infrared Index-band 7
NDVI	Normalized Difference Vegetation Index
NDWI	Normalized Difference Water Index
NIR	Near-Infrared
NMDI	Normalized Multi-band Drought Index
NOAA	National Oceanic and Atmospheric Administration
OK	Ordinary Kriging
OLI	Operational Land Imager
OLS	Ordinary Least Square
PC2	Second Principal Component
PC3	Third Principal Component
PDP	Partial Dependency Plot
PDSI	Palmer Drought Severity Index
QC	Quality Condition

RCVR	Road Network Coverage
RD	Road Density
<i>RMSE</i>	Root Mean Square Error
<i>RMSSE</i>	Root Mean Square Standardized Error
ROC	Receiver Operating Characteristic
SC	Schwarz Criterion
SDI	Streamflow Drought Index
SDVI	Standardized Vegetation Index
SE	Spatial Error
SETa	ETa Anomalies
SL	Spatial Lag
SoilM	Soil Moisture
SPEI	Standardised Precipitation-Evapotranspiration Index
SPI	Standardized Precipitation Index
SSEBop	Simplified Surface Energy Balance
StdDev	Standard Deviation
SWI	Surface Water Index
SWIR	Short Wave Infrared
TIR	Thermal Infrared
Tmax	Maximum Temperature
TPI	Topographic Position Index
TRI	Terrain Ruggedness Index
TRMM	Tropical Rainfall Measuring Mission
TWI	Topographic Wetness Index
USGS	United States Geological Survey
VIs	Vegetation Indices



---

## Introduction

### 1.1 Motivation

Despite inherent resilience of forest ecosystems to variations in climate ranging from short-term to millennia, climate shifts such as droughts, heatwaves, and water stresses can affect forest function, structure and services [1], resulted in large-scale mortality, forest fires, and insect outbreaks and pathogens [2–5]. Traditional methods dependent on the dendroclimatological surveys could retrieve tree responses to these conditions at fine time scales [6–10]; however, they are restricted to individual trees or local forest stands [11] and have the limitation for identifying the holistic status of a forest biome that affected by climate hazards.

Today, multitemporal satellite-based data and approaches have facilitated long-term and near-real-time assessing climate-induced vegetation anomalies at regional to global scales [12]. However, our understanding to date has been limited to explore satellite-based forest anomalies that mostly accomplished in tropical and boreal biomes using specific data and approaches, and sometimes with some uncertainties, which need to be elaborated in respect of other forest biomes, satellite data, and alternative approaches. The potential of new satellite products needs to be tested for retrieving forest droughts and detecting forest disturbances induced by climate hazards. Moreover, the approaches that could consider spatial and time dimensions of variables require to be explored for visualizing and quantifying forest droughts and disturbances induced by climate-triggered droughts.

## 1.2 Time series analysis of earth observation satellites

### 1.2.1 Sensors

Although numerous earth observation satellites, ranging from optical to radar, have been launched for monitoring and assessing the earth, very few sensors have been collected appropriate data for time series applications.

The time series of some optical satellite sensors are available for about four decades such as Landsat image collections obtained by MSS, TM, ETM+, and OLI sensors, and NOAA image collections obtained by different AVHRR sensors. The time series of MODIS sensors, onboard the Aqua and Terra satellites, in different time scales and spatial resolutions, are available after 2000 as well. The access to the archives of these data has been freely provided by the online databases of NASA and USGS (<https://lpdaac.usgs.gov>). The SPOT daily vegetation data at 1 km full spatial resolution are available since 1998, three months after archiving, to public users (<http://proba-v.vgt.vito.be/>). A series of data acquired by commercial high-resolution sensors since 1999, but are not freely available to public users. The capability of few sensors, with recording the bands in the thermal infrared ranges, has been demonstrated in the analysis of spatiotemporal patterns of LST, for example, from the MODIS, AVHRR, and Landsat sensors [13–15]. Also, the time series of some radar data are available; such as TRMM for monitoring precipitation since 1998 [16] and MetOp for collecting atmospheric information since 2006 [17].

The Sentinel satellites ranging from Sentinel-1 (radar images), Sentinel-2 (high-resolution multispectral images), Sentinel-3, and Sentinel-5P are being available under the Copernicus Program since 2014, 2015, 2016, and 2018, respectively. Although the duration of the collections of Sentinels is limited until the present, their broad ranges of applications particularly in vegetation and climate monitoring, high spatial and temporal resolutions, a wide range of bands for assessing vegetation disturbances from Sentinel-2, and free access through various databases such as Copernicus Open Access Hub (<https://scihub.copernicus.eu/>) and Google Earth Engine datasets (<https://developers.google.com/earth-engine/datasets/>) would provide a new era of the remote sensing time series analysis in the future decades.



### *1.2.2 Variables*

The analysis of time series of satellite data is mainly based on their derivative variables such as geophysical and index variables. The satellite-derived variables such as TOA, LST, and LAI—by a physical unit—are some examples of the geophysical variables. However, dimensionless satellite-derived indices such as NDVI, EVI, NDWI, and SWI are representative of the index variables [17]. For example, some products of MODIS such as MOD13Q1 provide 16-day vegetation indices including EVI and NDVI at 250 m or MOD11A2 provide monthly LST at 1 km since 2000.

### *1.2.3 Components*

Different components are defined for analyzing remote sensing time series such as the long term variations (trend component), seasonal variations, and short term variations. Changes in the phenology cycle of forests due to variation in the precipitation or temperature can emerge in the seasonal component. Immediate responses of forests to the pathogenes, insect outbreaks, and natural hazards is an example of residuals (short term variations), which will emerge as a long term trend (e.g., declining or increasing biomass) throughout the years [18].

## **1.3 Classification of droughts**

Drought is considered as one of the main global natural hazards with substantial effects on the natural ecosystems, societies, food, and global economies [19]. Drought is characterized by a gap in precipitation relative to long-term normal conditions, which may remain for several weeks to months in the regions either with high rainfall or with low rainfall [20]. Though there is no unanimous definition of drought, drought types are classified concerning their hazard aspects into meteorological drought, agricultural drought, and hydrological drought [21].

Meteorological drought is characterized by an amount of water lower than the long-term average that induces by low rainfall and high evapotranspiration in a specific area.

Agricultural drought is referred to as a condition that the availability of soil moisture affecting the productiveness and death of plants, resulting in reducing soil moisture reservoir and then crop yields [22].

Hydrological drought is characterized by a reduction in water availability forms including surface water or reservoirs, which estimates through its consequences such as the depletion of aquatic habitat, the failure of irrigation and hydroelectric projects, and recreational programmes [23].

Despite this, further drought classifications have developed depending on drought's consequences to the social security and economy such as socioeconomic drought or disturbances-induced natural ecosystem damage such as ecological drought [21].

However, forest drought is characterized by its physiological responses to drought incidences [24], which may appear as a reduction in forest's water content or greenness properties with massive consequences such as tree mortality, forest fires, insect infestations, and pathogens.

## 1.4 Drought dimensions

Drought is a complex phenomenon with various dimensions, which employ for assessing and monitoring of droughts. Some major dimensions are severity, frequency, duration, onset and end time, and spatial extent of drought. The severity is defined as a degree of moisture deficit and divided into mild, moderate, severe, and extreme categories. The severity is measured using drought indices. The frequency represents the recurrence interval of moisture deficit. The duration is the time interval between the onset and end of a drought episode. The onset and end times represent the start and end times of a drought episode, respectively; they are determined with respect to the specific threshold values of drought indices. The spatial distribution of drought across the landscape is defined as the spatial extent of drought; it is determined using multitemporal remote sensing data and drought indices [25].

## 1.5 Remote sensing of drought

Drought indices are mainly applied for quantifying droughts depending on the ground-based or remote sensing data. Conventional meteorological and hydrological drought indicators such as SPI and SWI are obtained from analyzing the historical ground-based databases.

Advanced remote sensing systems have provided data and products that could appropriately quantify, monitor, and assess droughts from both spatially and temporally aspects at local, regional, and global scales [25,26]. Time series of AVHRR, MODIS, and Landsat are long series of databases that could quantify not only droughts' dimensions but also could assess vegetation responses to climate hazards from local to global scales [27].

Various indicators have been developed concerning the visible, NIR, SWIR, and TIR spectra of satellites for quantifying and assessing droughts' dimensions and their effects on the forest functionality, composition, and services. Some indices have targeted the greenness variations of vegetation during drought episodes such as NDVI and EVI [28], while several indices have developed for assessing the water content variations of vegetation in such a condition like NDWI [29].

Although some studies verified the capabilities of satellite-derived indices for detecting responses of forests to drought conditions [30], other studies have challenged their capabilities in this concept [31]. Moreover, forest biomes may show different responses to drought episodes. For example, forests in the arid and humid biomes have shown responses to droughts at shorter time-scales than the forests in the semiarid and sub-humid biomes [32–34]. There is little information about the responses of temperate forests, such as Hyrcanian forests, to drought conditions regarding time scales, the potential of vegetation indices for retrieving physiological responses of these forests, and the priority of greenness and water content indicators for these purposes.

## 1.6 Forest degradation and climate-triggered drought

Various abiotic and biotic agents are controlling forest degradation. The abiotic agents such as high temperatures, droughts, fluctuations of soil moisture, and forest fires may significantly trigger biotic agents such as invasive species, insect defoliators and pathogens [4,35–37]. Some studies demonstrated that long-lasting droughts increase forest vulnerability that could affect the carbon storage and hydraulic systems of trees [38–42] by the symptoms like reducing growth and greenness, or increasing tree mortality, insect outbreaks, and pathogens [43–48].

Although several studies have documented the effects of high temperatures on insect outbreaks [49–51], there are still some uncertainties about the effects of droughts on triggering forest insects [52]. Moreover, some studies reported the positive impact of forest fires on insect outbreaks [53,54], while insect infestation may have positive [5,55,56], negative [57], or neutral [58,59] effects on the severity of forest fires.

Different wavelengths of satellite remote sensing provide the possibility for detecting different forest disturbances induced by biotic or abiotic agents. The infestations caused by insects and pathogens could be discriminated from healthy forests with the contribution of bands in the visible, red edge, NIR and SWIR-1 ranges [60–64]. Forest affected by water stresses could be identified through the bands in the regions of visible, red edge and NIR plateau [61,62]. The anomalies of forest greenness and water content may be retrieved using indices derived from the bands in the regions of visible, red edge, SWIR-1 and -2 [34,65–67]. Trends in the tree mortality could be depicted through the series of vegetation bands or measuring the shifts in SWIR reflectances in a died-off forest relative to its healthy condition [68].

Although advanced satellite-based approaches have provided discriminating insect-affected forests from undisturbed forests, measuring the intensity of individual tree mortality from available time series is directly problematic. Therefore, the approaches are mostly limited to analyse the relationships between the satellite-derived physiological anomalies of forest and field-based tree mortality mensuration using LASSO regression [69], random forest [70], or timescales and time-lag effects [71,72] approaches. Despite their satisfactory results in terms of performance, accuracy, and predictions, they summarize the model residuals of data from different locations without taking account of their spatial variations. Spatial regression approaches could consider the effect of the spatial location of data by calculating weights in relations with neighbours such as SL and SE [73] or within a kernel such as GWR [74]. Little known about the efficiency of spatial autoregressive models for quantifying the effects of climate-triggered drivers on the satellite-derived forest droughts and disturbances.

Furthermore, random forest and TreeNet algorithms, depending on machine learning, could satisfactorily detect some forest insect disturbances using satellite-derived features [49,75,76]. Machine learning approaches such as random forest and TreeNet can handle big data without the need for any preprocessing; they work with both parametric and non-

parametric variables, and avoid over-fitting in learning data [77,78]. Besides, image segmentation concerning spectral information of images significantly increases the accuracy of extracting features from satellite images. In addition to numerous image-based object features, there is a possibility to derive features from GIS databases and apply them for image classification— known as GEOBIA [79]. The integration of GEOBIA and machine learning algorithms may improve discriminating forest disturbances from the forest background and each other.

## 1.7 Hyrcanian forests

The Hyrcanian temperate broadleaf deciduous and mixed forests are the only relic forests of the Paleozoic Era and known as the alive fossils of Euro-Siberian phytogeographical forests that were destroyed during the glacial periods [80]. Indeed, the milder climate conditions of the Caspian Sea led them to survive during the glaciation era.

The Hyrcanian ecoregion stretches as a narrow belt—880 km length and 20 to 75 km width—along with the southern shores of the Caspian Sea and the northern mountain ranges of Alborz (Figure 1.1a and b). These forests are one of the richest ecosystems in the world by more than 280 endemic and subendemic vascular plant species, about 180 birds and 58 mammals species. These forests comprise a mixture of broadleaf tree species such as chestnut-leaved oak (*Quercus castaneifolia*), oriental beech (*Fagus orientalis*), hornbeam (*Carpinus betulus*), velvet maple (*Acer velutinum*), Persian ironwood (*Parrotia persica*), and elm (*Ulmus glabra*) [81,82].

This study was accomplished in the eastern part of Hyrcanian forests, northeastern Iran. Three basins were selected in the Golestan Province including Atrak (7,931 sq.km), Gorganrood (10,826 sq.km) and Qare-sou (3,153 sq.km). The Gorganrood and Qare-sou basins mostly cover by natural forests, while the Atrak basin consists of semi-steppe winter rangelands (Figure 1.1c).

These forests largely have been degrading not only by intensive anthropogenic processes [83] but also by severe natural hazards— such as large forest fires, insect outbreaks (Figure 1.2) and pathogens [84–87]— that may be induced by extreme climate conditions.

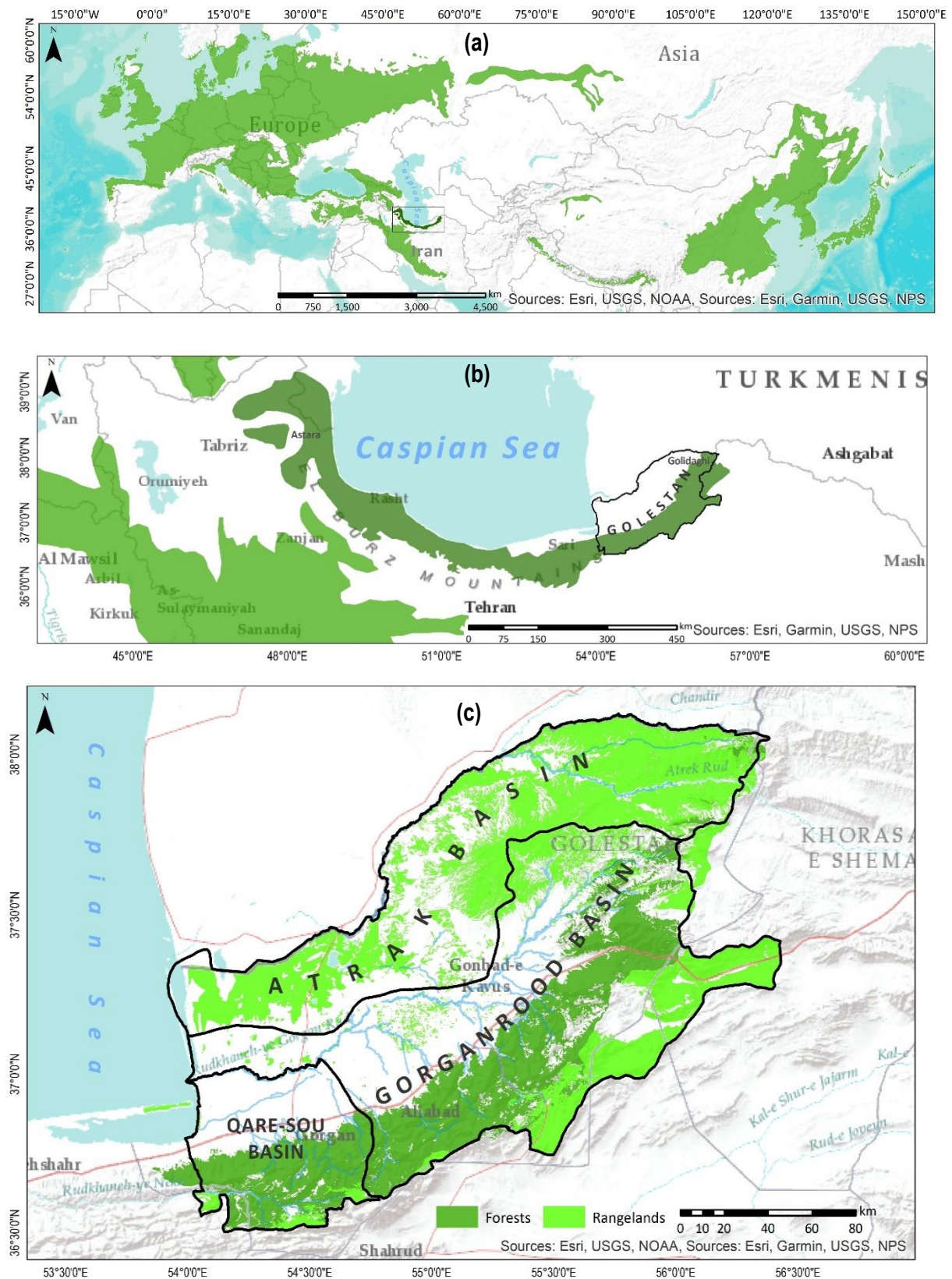


**Figure 1.1** The locations of Hyrcanian ecoregion in the Eurasian temperate broadleaf and mixed forests (a), Golestan Province in the Hyrcanian ecoregion (b), and the distribution of forests and rangelands in three studied basins including Atrak, Qare-sou and Gorganrood (c).





**Figure 1.2** A Hyrcanian forest stand (a) and an individual tree (b) attacked by insect defoliators in NE Iran in 2014.

This research starts by investigating the causes of large forest fires in 2010 along with the drought condition and then continues to retrieve long-term drought conditions and satellite-derived physiological responses of both rangelands and forests to these extreme conditions in the Hyrcanian ecoregion. Progressively, it explores further extreme climate variables and their effects on the different types of forest degradation such as the intensity of tree mortality, insect infestations, and forest fires.

## 1.8 Objectives

This dissertation seeks to investigate remote sensing-based forest droughts induced by meteorological and hydrological droughts and their effects on forest fire severity, tree mortality diversity, and insect infestation intensity in the Hyrcanian forests. Moreover, it examines novel approaches for visualizing and quantifying associations amongst these variables by applying spatial autocorrelation and regression models, machine learning algorithms, and panel data analysis.

The specific objectives of this dissertation are to:

- assess determining factors of forest fires under a drought condition

- evaluate spatial and temporal responses of forests and rangelands to precipitation deficits based on the long-term variations of MODIS-derived vegetation greenness and water-content properties in the Hyrcanian ecoregion
- investigate spatial associations between the dimensions of forest droughts and the dimensions of meteorological and hydrological droughts using multitemporal MODIS products and Fuzzy techniques in the Hyrcanian deciduous forests
- explore the intensity of tree-mortality induced by MODIS-derived hazard intensity of forest droughts
- develop a new approach for discriminating between insect-defoliated and non-insect-defoliated forests from Landsat 8 OLI and ancillary data by applying GEOBIA and TreeNet algorithm
- identify mutual relationships between the intensity of insect infestation and severity of forest fire in the presence of TerraClimate-derived climate hazards throughout the time period of the forest infestation using panel data models in the Hyrcanian forests

## 1.9 Overview of the dissertation

This cumulative dissertation is divided into six chapters. After this introductory chapter, the main parts of the dissertation are structured in the four chapters that were written as stand-alone articles and published in international peer-reviewed journals. These articles were written mainly by the first author (the author of this dissertation) and revised by co-authors.

As each of the articles has published by a specific publisher, they were reformatted base on a single standard structure in this dissertation. The contents of the four articles have remained unchanged throughout the dissertation and are embedded in Chapter 2 to Chapter 5 as follows:

Abdi, O.; Kamkar, B.; Shirvani, Z., Teixeira da Silva, J.A.; Buchroithner, M.F. Spatial-statistical analysis of factors determining forest fires: A case study from Golestan, Northeast Iran. *Geomatics, Natural Hazards and Risk* **2018**, 9, 276–280, doi: 10.1080/19475705.2016.1206629

Abdi, O.; Shirvani, Z., Buchroithner, M.F. Spatiotemporal drought evaluation of Hyrcanian deciduous forests and semi-steppe rangelands using moderate resolution imaging



spectroradiometer time series in Northeast Iran. *Land Degrad. Develop.* **2018**, 29, 2541–2525, doi: 10.1002/ldr.3025

Abdi, O.; Shirvani, Z., Buchroithner, M.F. Forest drought-induced diversity of Hyrcanian individual-tree mortality affected by meteorological and hydrological droughts by analyzing moderate resolution imaging spectroradiometer products and spatial autoregressive models over northeast Iran. *Agricultural and Forest Meteorology* **2019**, 275, 265–276, doi: 10.1016/j.agrformet.2019.05.029

Abdi, O. Climate-Triggered Insect Defoliators and Forest Fires Using Multitemporal Landsat and TerraClimate Data in NE Iran: An Application of GEOBIA TreeNet and Panel Data Analysis. *Sensors* **2019**, 19, 3965, doi: 10.3390/s19183965

Therefore, the presented dissertation is based on the included articles and framed by an introductory and a conclusion chapter as follows:

Chapter 1 addresses the importance and problems, research questions, objectives, background about remote sensing of forest droughts, tree mortality, and forest infestation, and structure of the dissertation.

Chapter 2 attempts to discuss determining factors of forest fires focusing on climatic, environmental, and anthropogenic agents during a drought condition.

Chapter 3 explains monthly and seasonal responses of deciduous forests and semi-steppe rangelands to drought conditions. It discusses how vegetation anomalies were derived from MODIS time series and also presents the spatial models for estimating long-term precipitation anomalies. Ultimately, it demonstrates the spatial indicators for testing local relations between vegetation (forest and rangelands) stresses and precipitation deficits.

Chapter 4 assesses the long-term responses of forest types to meteorological and hydrological droughts and investigates spatial associations of the diversity of tree-mortality and the hazard intensity of forest droughts. Drought hazard intensity was calculated from different drought dimensions for forest, meteorological and hydrological variables. The dimensions of forest drought were derived from MOD13Q1 time series. The dimensions of meteorological and hydrological droughts were derived from a combination of ground-based measurements and the MODIS products including MOD11A2 and MOD16A2. The intensity

of tree-mortality was computed based on the field observations of various tree species which were affected by different levels of dieback.

Chapter 5 presents a novel method for discerning insect-affected and non-insect-affected forests using GEOBIA and TreeNet machine learning algorithms with Landsat 8 OLI and ancillary data. Moreover, it investigates the relations between the intensity of insect infestation, climate hazards and the severity of forest fires. It explains how the hazard intensity of forest defoliation and climate variables were derived from the time series of Landsat and TerraClimate data, respectively. Meanwhile, it expresses how the severity of forest fires was calculated and explains the used methods for applying connections among these variables using panel data analysis.

Finally, Chapter 6 summarises achievements, expresses concluding remarks, presents the scientific relevance and also discusses an outlook on potential future studies to further improve the discussed approaches and forest disturbances using remote sensing data. Besides, this dissertation includes two Appendices supplementing Chapter 3 and 4.

---

## **Spatial-Statistical Analysis of Factors Determining Forest Fires: A Case Study from Golestan, Northeast Iran**

Omid Abdi, Behnam Kamkar, Zeinab Shirvani, Jaime A. Teixeira da Silva, Manfred F. Buchroithner

### Contributions:

Omid Abdi designed the work and contributed to data collection, spatial analysis, forest fire modelling, and writing the article.

Behnam Kamkar contributed to designing the work and statistical analysis.

Zeinab Shirvani made contributions in creating the database of forest fires and data analysis.

Jaime A. Teixeira da Silva revised the manuscript and assisted in writing the article.

Manfred F. Buchroithner reviewed the article and supervised at all stages of the study.

### Citation:

Abdi, O.; Kamkar, B.; Shirvani, Z.; Teixeira da Silva, J.A.; Buchroithner, M.F. Spatial-statistical analysis of factors determining forest fires: a case study from Golestan, Northeast Iran. *Geomatics, Natural Hazards and Risk* **2018**, *9*, 267–280, doi:10.1080/19475705.2016.1206629.

## 2.1 Abstract

Intermittent fires in Northeast Iran in the autumn of 2010 resulted in the burning of some valuable forest habitats. The objective of this study was to apply geographic information systems (GIS) to determine to what degree three key factors (environmental, climatic, and anthropogenic) influence the severity rating of fires in these forests. The forest fire sites were surveyed and imported into GIS. The severity of burnt areas was considered in relation to the three factors. Statistical functions were used to calculate the effect of the factors at each fire site. Logistic and stepwise regressions were used to determine the fire severity rating related to each factor. The results indicate that as the number of cumulative days after the onset of fire increased, the burnt areas also increased at a rate of 303.5 ha/day ( $R^2 = 0.95$ ). Consequently, forest density, daily mean wind speed, daily mean temperature and distance to roads were highly correlated with the daily severity rating of forest fires, and only daily temperature and forest density affected the size of the burnt areas. Prediction maps show that about 24% of the forests have high fire durability, amounting to 7% of the fire-sensitive area. The findings from this case indicate that GIS can be effectively employed in fire management to assess the damage, and possibly to prevent future fires, thus assisting in the preservation of valuable forest resources.

## 2.2 Introduction

The prediction of forest fires constitutes a significant component of forest fire management. It plays a major role in resource allocation, mitigation and recovery efforts. Forest and grassland fires cause air pollution, extinction of rare floral and faunal species, devastating loss and irreparable damage to the environment and atmosphere, global warming, and threaten the lives of people who live near forests[88]. Forest fires in Northeast Iran have become more common in recent years (Table 2.1). This phenomenon is of concern since the likelihood of similar fires in the future is high. For example, in 2010, intermittent forest fires burnt more than 16,000 ha in these areas in just less than one month [89]. In the majority of forest fire reports, the causes of these fires are 'unknown', so there is a need for basic studies that assess

the probability of forest fires and examine the main factors that affect its durability and severity.

**Table 2.1** Statistics of forest fires that were occurred in Northeast Iran from 2001 to 2010.

Year	Number of fires	Burnt area (ha)
2001	45	254.20
2002	59	395.50
2003	74	1920.10
2004	68	266
2005	132	633.60
2006	130	548.30
2007	124	766.7
2008	140	325.64
2009	67	201.25
2010	200	16180

*Source:* Abdi et al. [89] and Eskandari [90].

Forest fires, based on their origin, can be divided into natural fires, or fires induced by humans. Finding the relationship between fire and weather factors, vegetation and human criteria is necessary, and different aspects can be probed [91]. Substantial attempts have been performed for characterizing, anticipating, modelling, planning, and managing wildfires in various Mediterranean countries [92,93]. To determine the effects of anthropogenic, climate and environmental factors separately, different statistical methods, models and algorithms have been tested. Statistical methods have also been applied to visualize spatial and temporal variations in fire susceptibility as a function of predictors like vegetation, climate, relief, and anthropogenic activity by historical fire data [94–99]. Beverly et al. [100] developed a model for fire susceptibility in west-central Alberta, Canada, in which multivariate statistical analysis was used to identify the key factors, and their results were carried out to establish a Fire Susceptibility Index (FSI) that was significantly influenced by fuel composition, fuel organization and topographic of the earth's surface. Moreover, Beverly et al. [100] and Oliveira et al. [101] compared the application of multiple linear regression and random forest methods to identify the main structural factors that could describe the probability of occurrence of a fire at a European scale: the random forest model had a higher predictive capability than multiple linear regression. Furthermore, Oliveira et al. [101] applied some variables which were

common to both models, and rainfall and soil wetness appeared to affect the occurrence of fire to a vast range, although unemployment rate, overgrazing and local road density were also constituted to be significantly affected by the multiple linear regression and random forest methods. For instance, a logistic model was used by Chou et al. [102] to identify areas with a high likelihood of fire occurrence based on environmental, anthropogenic and spatial variables in the San Bernardino National Forest, California, and also by Garcia et al. [103] to forecast the sum of fire-days in the White Court Forest of Alberta, USA. In the region of Golestan forests of Northeast Iran, Abdi et al. [89] used a multiple regression model to identify the correlations between forest management factors and the frequency of forest fire occurrence, with a strong positive correlation (up to 70%) between fire duration and the low density of forest roads, fencing and channel excavation in forest management plans. In addition, the majority of burnt areas were affected by three factors: lack of skilled personnel reduced forest management practices and fencing or channel excavation operations (about 90%). Furthermore, Mohammadi et al. [104] integrated logistic regression and geographic information systems (GIS) to study the risk of forest fires and to identify the factors that most influenced the occurrence of forest fires in the forests of western Iran. In this study, the correlation between forest fires and climatic variables, human factors and physiography were analysed. Results indicated that the likelihood of fire occurrence was negatively correlated to slope percentage, altitude and distance from croplands, but was positively correlated to the amount of annual rainfall.

To rate the occurrence of wildfires, most industrialized countries use prediction systems that involve a large number of monitoring tools, including weather forecast algorithms. However, most of the developing countries cannot afford the use of these technologies because of the weakness of their technical resources. New approaches are, thus, needed to predict the occurrence of forest fires while considering a reduced number of monitoring features. These can be classified into wildfire occurrence prediction systems and indices, and artificial intelligence [105]. Therefore, in countries such as Iran, identification of effective factors to control forest fires and the use of prediction probability maps can serve as a preventive or protective approach to improve fire management.

GIS and remote sensing, as two components of system-approach procedures, have been applied to evaluate fire susceptibility at distinctive spots based on spatial data for biophysical factors, the fire variations, and other attributes, or in composition with fire-behaviour models [91,106–109]. These two techniques have also been used to determine risk zones and probability maps of fire occurrence [91,110–112]. For example, a method based on spatial GIS analysis and logistic regression was used by Zhang et al. [113] to predict the probabilities of anthropogenically caused grassland fires in Inner Mongolia.

Since there is a lack of novel methods to monitor the early detection of forest fires in Iran, identifying induced factors and mapping fire susceptibility is very important. Therefore, the goal of this study was to use the spatial and statistical capabilities of GIS to determine the effect of environmental, climatic and anthropogenic factors on the temporal extension and area of forest fires. Besides, mapping forest fire susceptibility depended on the significant effect of factors on fire severity in the forests of Northeast Iran.

## 2.3 Materials and Methods

### 2.3.1 *Study area*

This study was performed in the northeast forests of Iran located in the Southeast of the Caspian Sea. The geographic coordinates of the study area are within 54° 43' 55" to 56° 01' 09" E and 36° 44' 02" to 37° 29' 14" N. It is approximately 116 km long, 30 km wide, and an area spanning of 2465 km<sup>2</sup>. The elevation ranges from 190 to 2500 m above sea level. The relief increases gradually with increasing elevation from South to North. According to reports by the Department of Natural Resources and Watershed Management (DNRWM) of Golestan Province, more than 14550 ha of these areas burnt during less than one month in October and November of 2010. In this period, the mean temperature amounted approximately to 22 °C (6 °C higher than the long-term average), and the average precipitation was 40 mm lower than long-term data. The average lowest relative humidity was 35% (20% less than long-term data). In those two months, there were only three rainy days versus 10 days for long-term data. The vegetation in the Golestan forest region has a diversity of plant communities, including beech

(*Fagus orientalis* Lipsky), alder (*Alnus subcordata* C.A.Mey.), Caucasian oak (*Quercus castaneifolia* C.A.Mey.), Eastern hornbeam (*Carpinus betulus* L.), yew tree (*Taxus baccata* L.), common juniper (*Juniperus communis* L.), cypress tree (*Cupressus sempervirens* L.), and ironwood (*Parrotia persica* (DC.) C.A.Mey.) [114]. The study area consists of nine counties, including approximately 356 towns and villages. Paved roads, dirt roads and forest roads are common in this region (Figure 2.1). Most of the forest roads were built to facilitate wood production and forest accessibility, and have a low density (4.53 m/ha), distributed unevenly throughout the area.

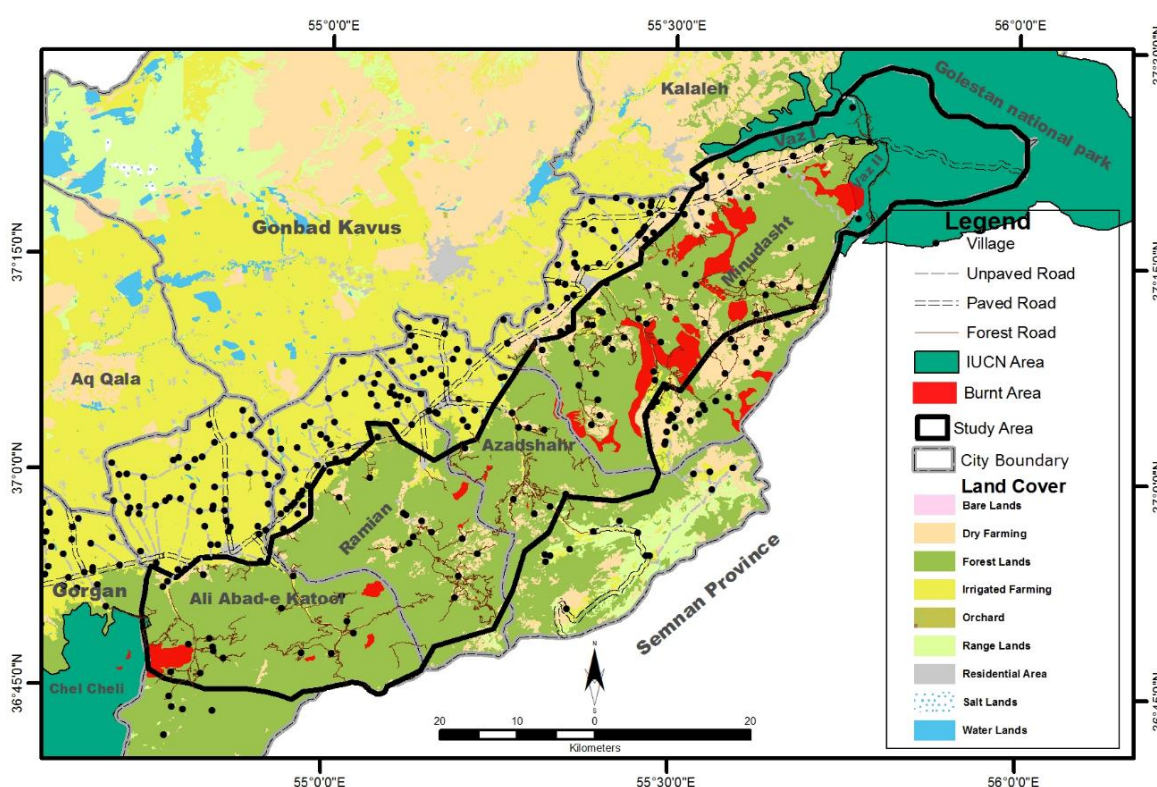


**Figure 2.1** The distribution of towns and villages, paved roads, dirt roads and forest roads in Northeast Iran.

### 2.3.2 Digital fire data

The fire data were provided by the DNRWM of Golestan and established after our field survey. The fire database is based on a data archive, including all reported forest fires from 16 November 2010 to 13 December 2010 (29 consecutive days), where a total of 135 fires occurred. The size of the burned polygons was between 0.1 and 2927 ha. In most cases, the causes of fires were unknown. Each fire report contained different variables, including the fire's location, duration (minutes), day of ignition, final area burnt, weather and estimated cause. The boundaries of the forest fire polygons were surveyed using an Oregon 550 Garmin GPS device.



### 2.3.3 Digital map data

All digital data related to the factors affecting the forest study area were obtained from two- and three-dimensional digital topographic maps (scale of 1:25,000) of the National Cartographic Center of Iran (NCC), SPOT5 satellite imagery, and daily meteorological data from available synoptic-climatological stations in Golestan Province. All digital data and spatial analyses were performed using ArcGIS software. Geodatabase data were created for boundary lines, roads, residential areas and forests. All geo-data were available at a 1:25,000 scale, as a Universal Transverse Mercator projection and as WGS84 Datum.

### 2.3.4 Methods

#### 2.3.4.1 Spatial analysis

Environmental factors including slope, aspect and plan curvature layers were derived using surface analysis functions from the Digital Elevation Model (DEM) with 10 m cell size. Forest density was obtained using the Normalized Difference Vegetation Index (NDVI) from SPOT5 images for September and November 2009 with 10 m spatial resolution, four spectral bands with orthorectification, corrected for terrain displacement, and also for atmospheric effects. The values of this index range from -1 to 1 [115]. The common range for green vegetation is 0.2–0.8.

Climatic factors were mapped using different GIS functions. The historical meteorological data were obtained from available non-automatic weather stations. These data were extrapolated to calculate meteorological layers with a cell size of 10 m<sup>2</sup>. For this purpose, a multiple regression method was applied. Each variable, including mean temperature, average relative humidity, wind speed and precipitation, was related to corresponding coordinates and elevation data. To obtain the least-squared difference between observed data minus simulated data, different combinations were tested. Then, a 10 m<sup>2</sup> DTM array was generated to extract X and Y coordinates as well as Z values in the centre of each cell. Finally, all meteorological variables were calculated by an algebraic function and interpolated by functions of the Spatial Analyst of ArcGIS10.1.

Then, different anthropogenic-induced factors were assessed, including the distance from paved, dirt and forest roads; residential area maps were created by connectivity and spread functions, while the population density layer was created by the Kernel density function. From this set of data, different variables were selected as input data for the fire prediction model (Table 2.2).

**Table 2.2** Environmental, climatic, and anthropogenic parameters used as factors affecting the occurrence and durability of forest fires.

<b>Factors</b>	<b>Predictor description</b>
<i>Environmental parameters</i>	
Digital elevation model	Elevation (m)
Slope	Slope (degree)
Plan curvature	The direction of maximum slope
Aspect	Aspect (degree)
Forest density	Normalized Different Vegetation Index
<i>Climatic parameters</i>	
Temperature	Daily mean temperature (°C)
Relative humidity	Daily relative humidity (%)
Wind speed	Daily mean wind speed (m/s)
Precipitation	Daily precipitation (mm)
<i>Anthropogenic parameters</i>	
Population density	Population density (people/km <sup>2</sup> )
Residential distance	Distance to the residential (m)
Paved road distance	Distance to the paved road (m)
Dirty road distance	Distance to the dirty road (m)
Forest road distance	Distance to the forest road (m)

The most commonly used metrics to describe the effectiveness of a forest road network included road density ( $R_D$ ), which is simply the length of roads divided by the forest area, and road network coverage ( $R_{CVR}$ ), which is obtained by dividing the average distance of road spacing by the forest area [116].

#### 2.3.4.2 Statistical analysis

Forest fire severity was considered as the period from the start until the end of the fire against the total burnt area. Cumulative burnt areas were plotted against time (days). From this curve, the time to burn 50% of the total area was determined by fitting a logistic model to the cumulative burnt areas ( $G$ ) versus time ( $t$ , hours), as indicated in Equation 2.1:

$$G = \frac{F_x}{1 + \exp[a(t - b)]} \quad (2.1)$$

where  $F_x$  is the maximum burnt area,  $b$  is the time to reach 50% of all cumulative burnt areas and  $a$  is a value determined by an iterative optimization method to minimize the observed minus the predicted value. The times for 5%, 10%, 90% and 95% were also determined by interpolation and are designated as D5, D10, D90 and D95, respectively.

To calculate the mean values of three factors (environmental, climatic and anthropogenic) for each fire region, the zonal statistics function was used. Consequently, the stepwise multiple regression method [117] was carried out to find the relationship between dependent and predictors in SPSS software program; the variables of three factors (environmental, climatic and anthropogenic) were entered based on their correlation with the dependent variables (forest fire severity) in the model. Variables with a higher correlation were entered earlier, and variables with a lower correlation were eliminated. Eventually, numerical models of forest fire susceptibility were developed, and the maps of forest fire susceptibility, in a raster format, were generated based on these models and also the significant factors affecting fire severity in the study area. These maps were then classified into five categories with the equal interval method in ArcGIS.

## 2.4 Results and discussion

Forest fires present a real threat to precious forest resources in the northeast of Iran, almost 14,550 ha of this area burned during November and December of 2010. The size of fire patches was calculated as being between 1.13 and 2927 ha (Figure 2.1). The duration of the fires was variable, from 2 h to 12.7 days with approximately 29 days in total. In other words, about 4% of the forests burned in less than one month. Results of the logistic model indicate that with increasing cumulative days after the onset of a fire event, the burnt areas also extended at a rate of 303.5 ha/day (Figure 2.2;  $R^2 = 0.95$ ). The results also indicate that approximately 50% of the total area burned over 19 days and that the remaining 50% only within the 10 remaining days (Figure 2.3).

The rate at which the fire spread increased at the end of this period, revealing that operations to suppress and prevent fire were not successful.

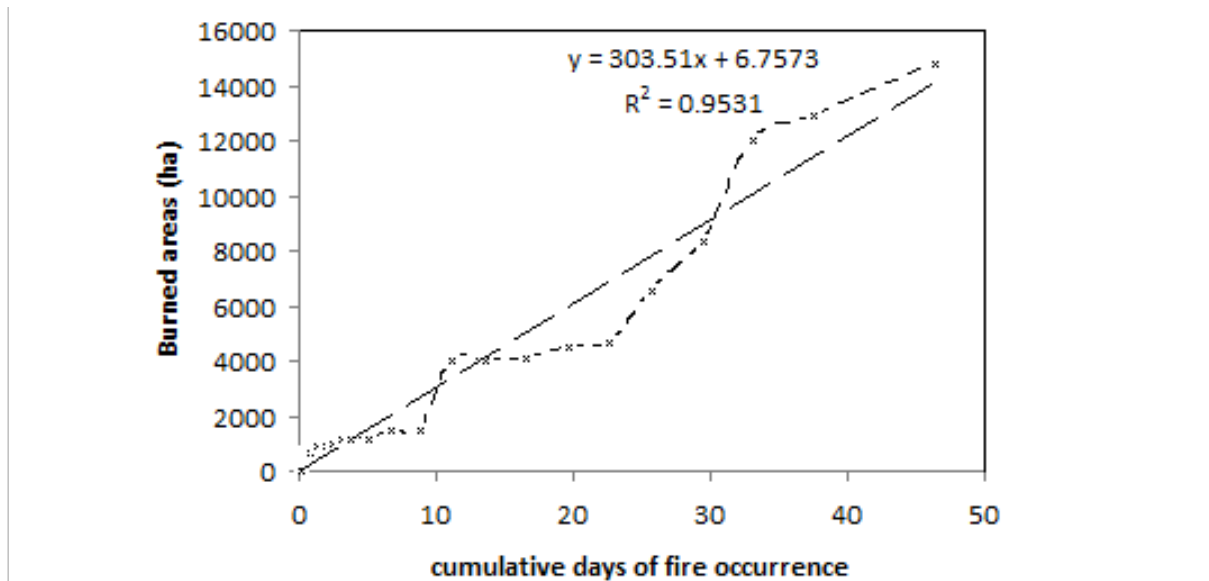


**Figure 2.2** The logistic model between burned area and duration of fire in Northeast Iran.

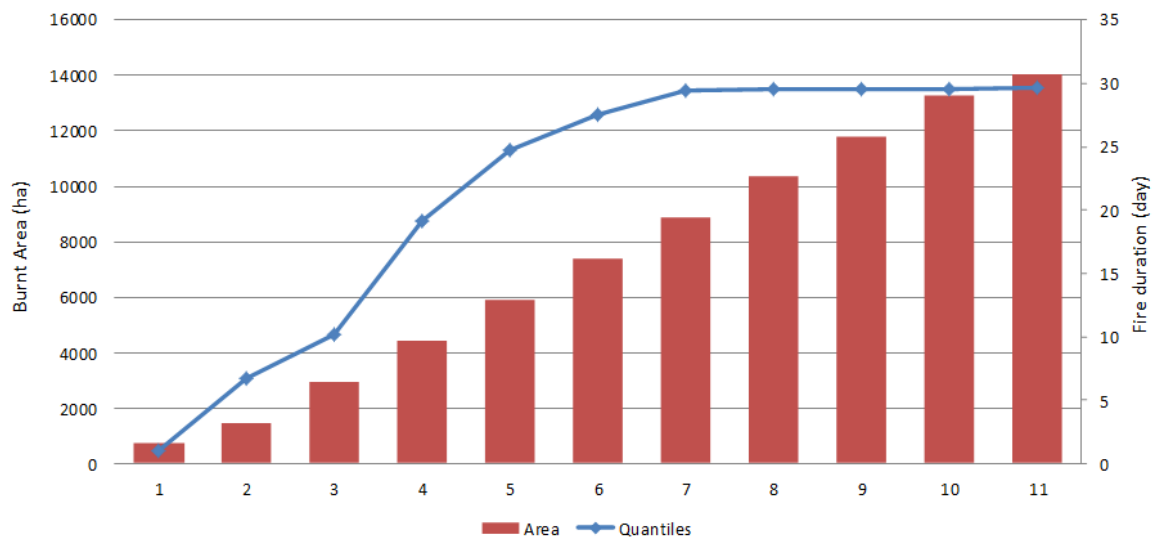


**Figure 2.3** Cumulative days of fire occurrence against burnt area (cumulative days calculated based on cumulative hours of forest fire occurrence in all burnt areas divided by 24 to convert it to the daily).

Stepwise regression results of the three key factors (environmental, climatic and anthropogenic) affecting the occurrence of fire are shown in Table 2.3. The start and extend of a fire event are mainly affected by the water content of the surface fuels, by the moisture content of the trees, and by wind speed. Various limitations provide the litter moisture content to be evaluated: air temperature, moisture, and precipitation [118]. Extreme climate

parameters were ripe for the occurrence of fire in the northeast of Iran during these forest fires, as the mean temperature was approximately 6 °C higher than the long-term average (1980–2010), average precipitation was 40 mm lower than the long-term mean, and average relative humidity was 20% less than long-term data. The wind speed was between 11.50 and 65.50 km/h with an average of 36.80 km/h in the fire patches (Table 2.4). Statistical analysis of climate factors indicates that daily mean temperature and wind speed significantly affected the duration of forest fires in the study area ( $R^2 = 0.47$ ;  $F = 10.4$ ;  $P \leq 0.05$ ), but there was no significant correlation between the size of fires and these parameters.

**Table 2.3** Stepwise regression results depending on the factors affecting forest fire occurrence in Northeast Iran.

Factors	Sig.	F	Determination coefficient
<i>Fire durability</i>			
Forest density	0.0028	11.34	32.48
Daily mean of wind speed	0.0567	4.05	47.27
Daily mean temperature	0.0001	21.93	55.46
Distance to roads	0.0002	8.96	63.06
<i>Burnt area</i>			
Daily mean temperature	0.006	9.1	27.48
Forest density	0.000	130.01	88.84

Figure 2.4 shows that the larger fire patches occurred in the regions with average wind speed. Furthermore, our analysis indicated that daily mean temperature was affected both by fire duration and fire spread ( $P \leq 0.01$ ), more so by fire duration than fire spread in all fire patches (Table 2.3).

**Table 2.4** Statistics of climatic parameters during times of forest fires compared with long-term data (1980–2010) in Northeast Iran.

Climatic parameters	Average statistics for Oct. & Nov.	
	Long-term	2010
Daily mean temperature (°C)	15	21
Daily relative humidity (%)	55	35
Daily mean of wind speed (m/s)	5.5	10.2
Daily precipitation (mm)	58	18
Frequently of precipitation (day)	10	3

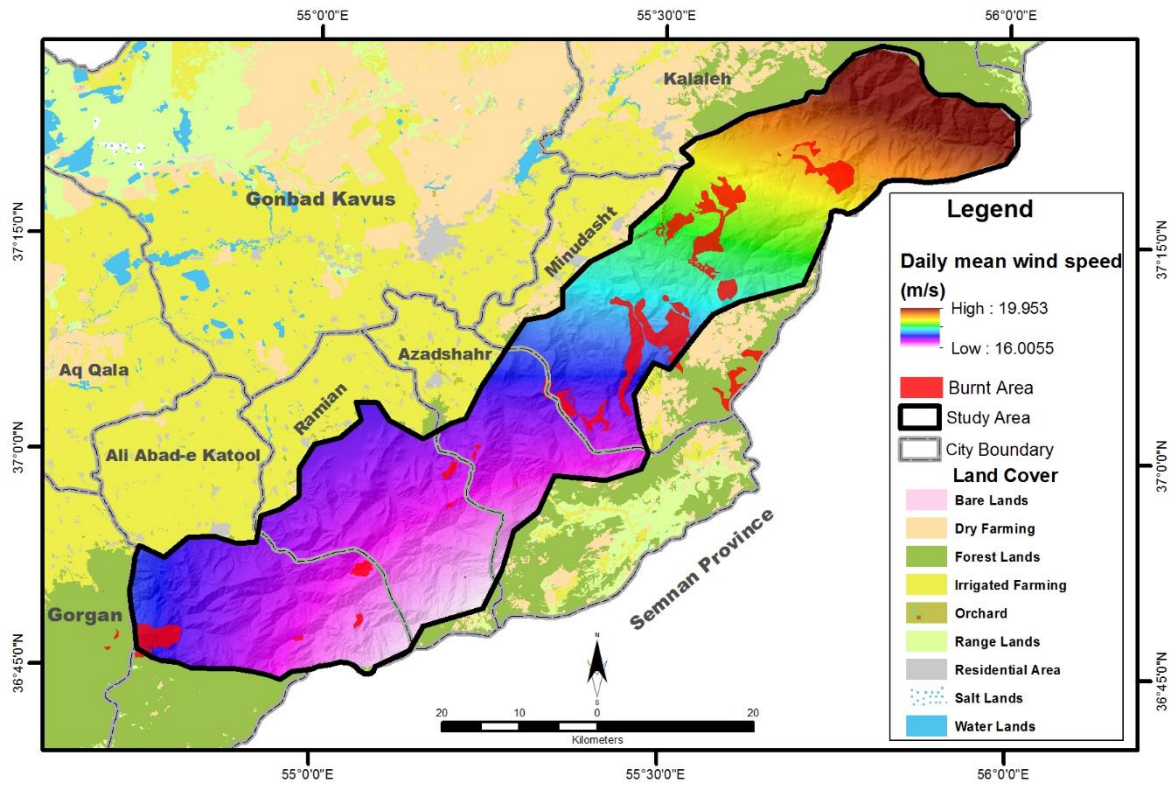


**Figure 2.4** The spatial relationship between daily mean wind speed and burnt areas in Northeast Iran.

Figure 2.5 indicates that fires that occurred at high temperatures displayed more extreme severity than those that occurred at low temperatures. Some previous scholars have demonstrated that under extreme climate-change pressure, weather applies a significant control on fire severity and fire behaviour [93,119–122]. In this study, other climatic parameters (daily relative humidity and precipitation) showed fewer changes during wildfires and no significant effect on fire severity. In contrast, the results of earlier research indicate that the probability of fire occurrence is positively related to the amount of annual precipitation [101,104].

Moreover, among all anthropogenically induced factors, only distance to roads had a high positive correlation with fire durability. When this factor was added to the regression model, the coefficient of determination ( $R^2$ ) for the model increased to 63.06% ( $F = 10.4$ ;  $P \leq 0.01$ ). Furthermore, Figure 2.6 indicates that the forest road network did not comply with the standards of forest roads in the study area. The road density (RD) was 4.53 m/ha, and road network coverage (RCVR) was observed in 53.97% of the study area. Thus, optimum road density can decrease the occurrence



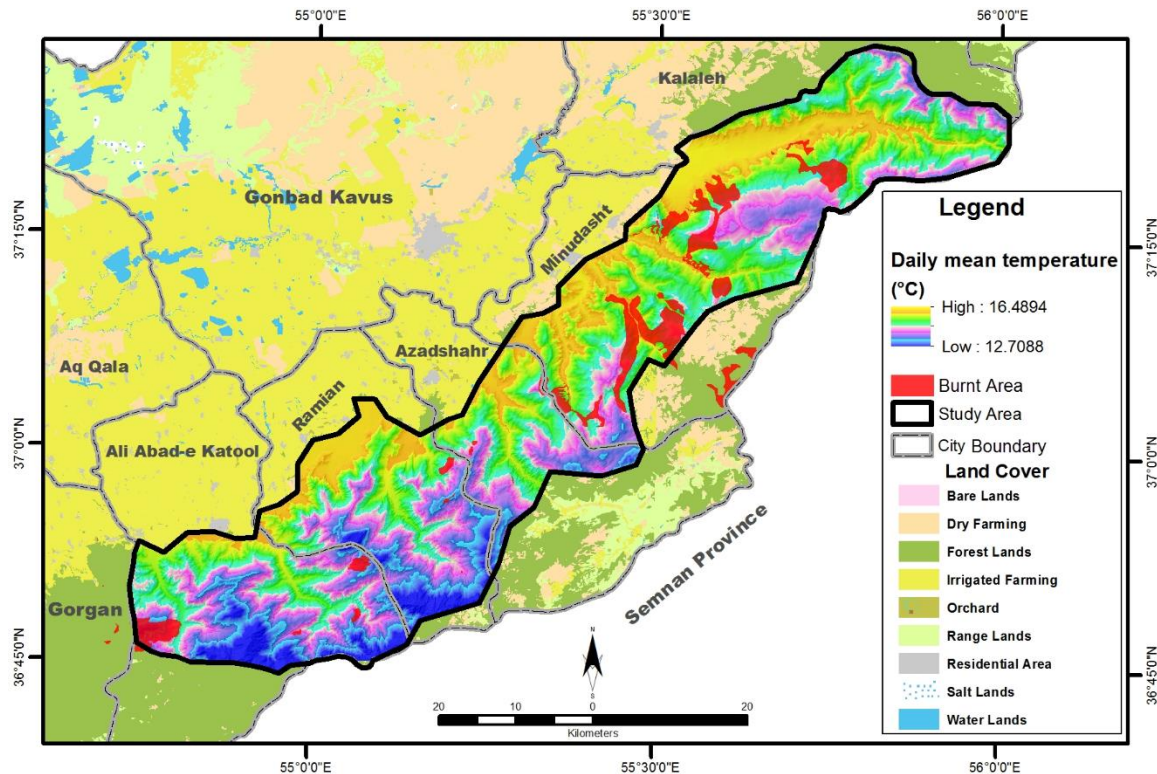


**Figure 2.5** The spatial relationship between daily mean temperature and burnt areas in Northeast Iran.

and duration of fire because access to fire-prone zones is easier. This is consistent with other research findings in Iran [89]. The vicinity to the road is a known key factor in forest fire studies [101]. A survey of the burned forests showed that the majority of fire spots were located in regions with low road density. Therefore, it is important to consider optimal road density (around 20 m/ha) and a reasonable road network coverage (as much as 65%) within forest districts [116]. Access roads allow the movement of fire engines and reduce the travel time for fire crews to reach forest fires. In these forests, with low road density, tracks can be supplemented as primary forest roads. Tracks are very important for forest fire protection as they connect to the road network and also serve as a firebreak. They allow for wider and safer movements to fight a fire inside a forest or at its periphery [118]. Other anthropogenically induced factors had no significant effect on the duration of wildfires ( $P \geq 0.05$ ). Spatial analysis (Figure 2.1) shows that most wildfires occurred in areas with low population density and distant from public roads. The average distance of fire patches was 6 km from residential areas and 2.85 km from public roads. Other human activities might spark fires, including recreational activity, forest harvesting, mining and farming activities. This, in turn, suggests the need for carefully focused research into the patterns, seasonality, and

locations of different types of anthropogenic activities in fire-sensitive areas, demographics of the populations involved in these activities, and risk perceptions.

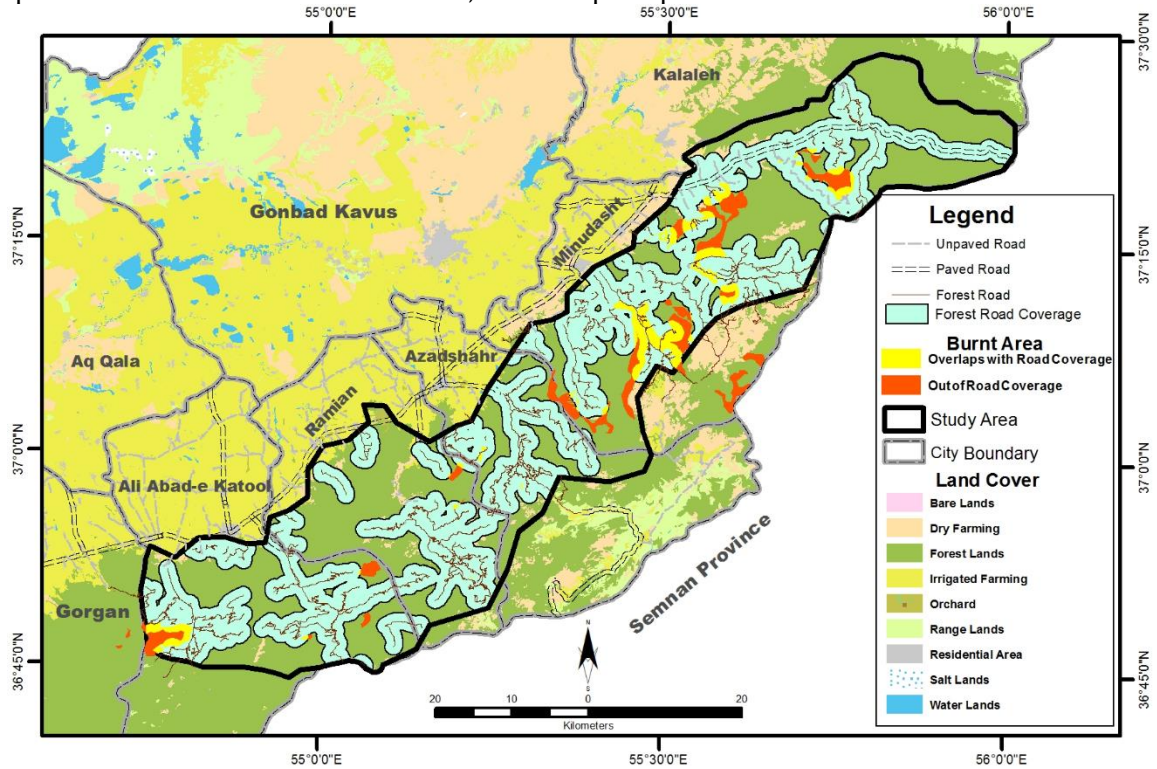


**Figure 2.6** Burnt areas that show overlaps with forest road network coverage and outside of it.

Regarding environmental variables, the regression model shows that forest density significantly affected fire severity (Table 2.3). Forest density not only affected the spread of fires more ( $R^2 = 0.89$ ;  $F = 130.01$ ;  $P \leq 0.01$ ) but also significantly affected the duration of fire patches ( $P \leq 0.01$ ). Figure 2.7 shows that the maximum NDVI value was about 0.71 in the study area. As the value of NDVI increased, forest density increased. Specifically, forest with high density is characterized by a continuous structure of tree crowns, where the fire is likely to spread as an active crown fire, thus leading to a greater accumulation of fuels and thus increase the severity of extreme fire [123,124]. This notion is supported by Figure 2.7, which shows that the percentage of the forest was significantly higher in fire patches than in other areas. Furthermore, in forest structures with high canopy closure, the risk of crown fires is higher because there is an increase in vertical and horizontal continuity [97,124]. Our study showed that there is no significant correlation between topographic parameters (slope, aspect and plan curvature) and fire severity in the study area ( $P \geq 0.05$ ). Nevertheless, the majority of fires occurred in the southwestern and southeastern aspects. Nearly 52% of areas to which fires spread and 45% of fire duration were



in the southwestern part, and these numbers were 33% and 31%, respectively, for the southeastern aspects, which tended to burn with greater intensity and thus with a resulting severity that was higher than in other parts because southern parts received more solar radiation and had less moisture [125]. Moreover, the average slope was about 40% in the fire patches, i.e. not a steep forest slope. Therefore, the slope had no significant effect on fire severity. Some research has shown that as slope increases, the distance and angle between flames and fuels decrease and result in more extreme fire severity [124,126–128].

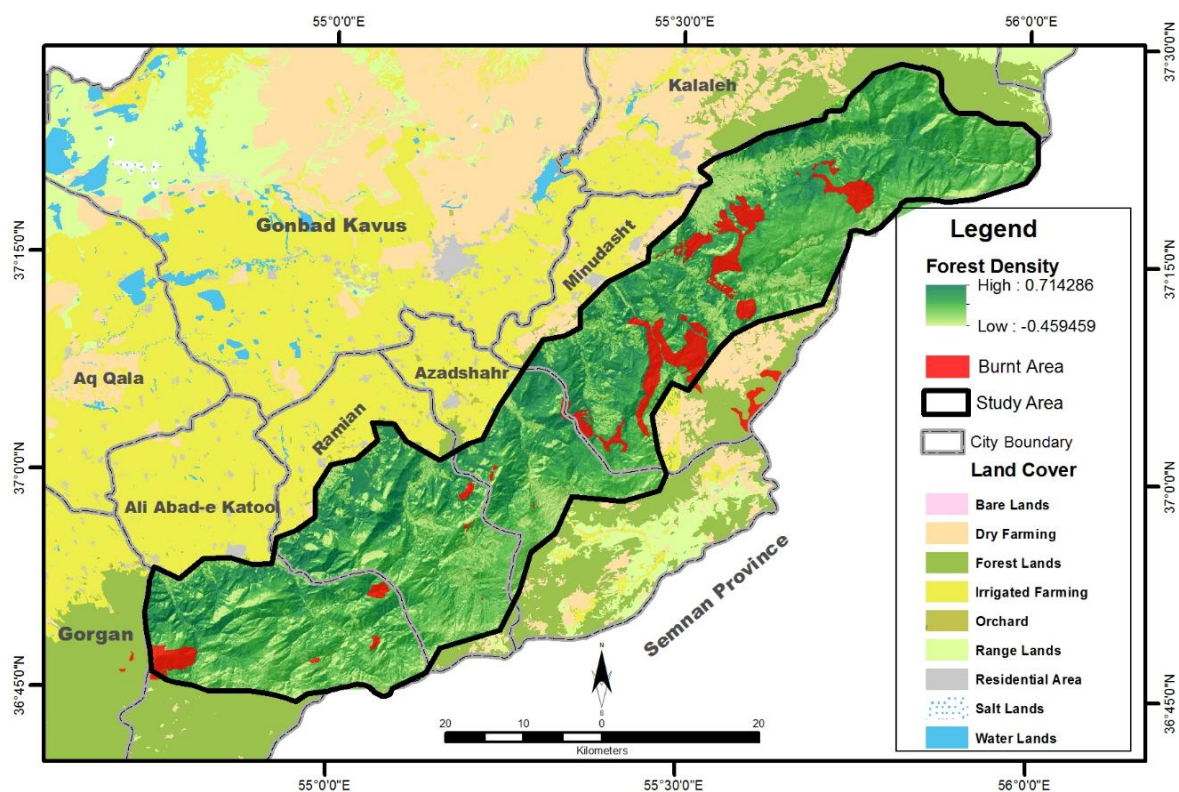


**Figure 2.7** Burnt areas and fire spreading patterns in the study area. Forest density was based on NDVI.

To apply these results to future forest fire management, susceptibility maps of forest fire severity were generated based on the significant factors in the regression results. This model incorporates environmental, climate and human factors, including vegetation, temperature, wind speed, and roads. Figure 2.8, which describes the likelihood of a forest fire based on the important parameters in fire durability, and classifies the five hazard categories by the equal interval method with intervals of 0.2 increments, shows that 24% of forests are in the hazard

class > 0.6 (high and very high), 38% in the medium class (0.4–0.6), 31% with low severity (0.2–0.4), and 8% below 0.2 (very low severity).

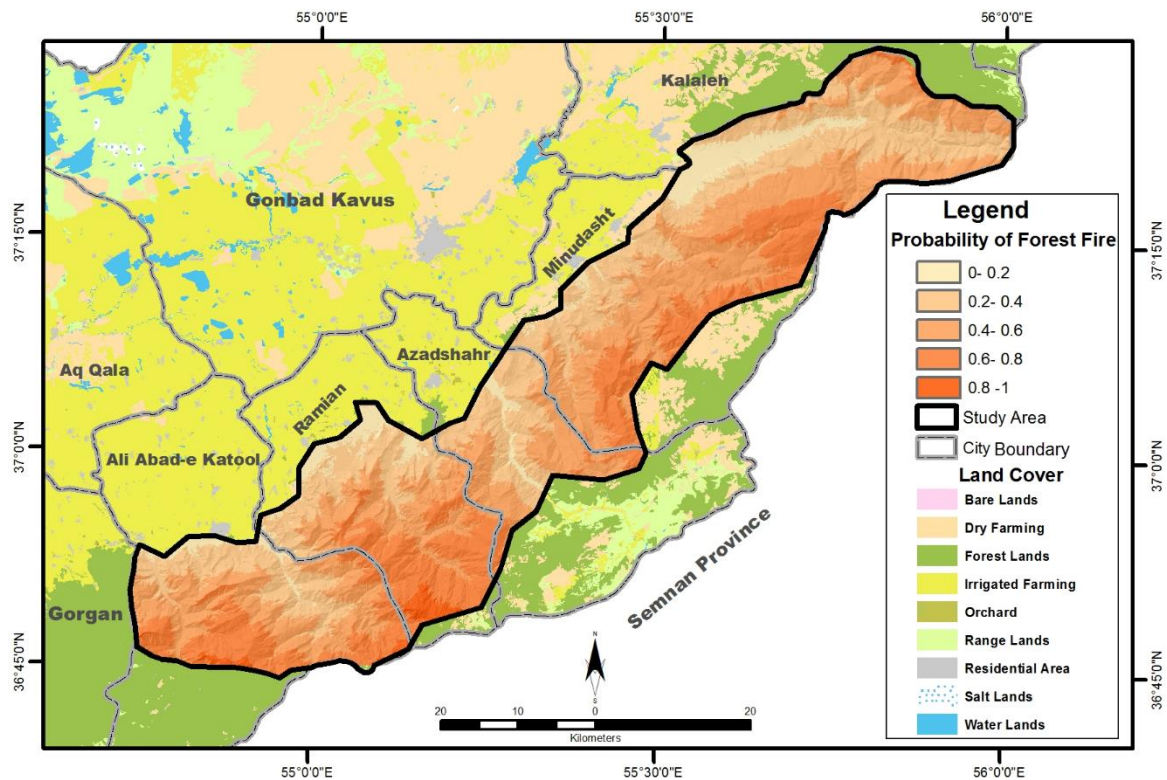


**Figure 2.8** Susceptibility map based on the duration of forest fires in Northeast Iran.

Table 2.3 shows that the distance to the forest road was the strongest variable to affect the duration of the forest fire with a determination coefficient of 63.06%. Our findings show that total road density in all the forests was about 4.53 m/ha, while it was much lower in the fire patches with about 1.03 m/ha (Figure 2.6). Road density is far from the required standards (20 m/ha) in the study area. Related to the duration of fires, about two-thirds of the study area are in the hazard class of medium and above, so the development of a forest road network with reasonable density and strong coverage is deniable. Moreover, results of the probability map of fire spread showed that the vast majority (83%) of forests are located in the medium severity (76%), high severity (6%) and very high severity class (~1%) (Figure 2.9). Larger fire patches with longer burn times tended to happen in distant areas with poor road density that were primarily located at higher altitudes, and fewer road lines expand fuel continuity and result in a less fragmented landscape. As a result, there were larger and longer fires, particularly in the areas of lower road density and weak road network coverage. Furthermore, larger fires

tended to be in more distant forests with low accessibility for firefighter crews in the ground-based operations), less fragmented by roads, and where there is high continuous fuel connectivity [129,130]. Higher road densities provide easier access for fire crews, equipment and behave like firebreaks in fire suppression [131,132]. In contrast, in some studies, the distance to the forest road was a significant contributing factor in human-induced fires, and higher road densities reflect a higher level of human activity [96,130,132,133].

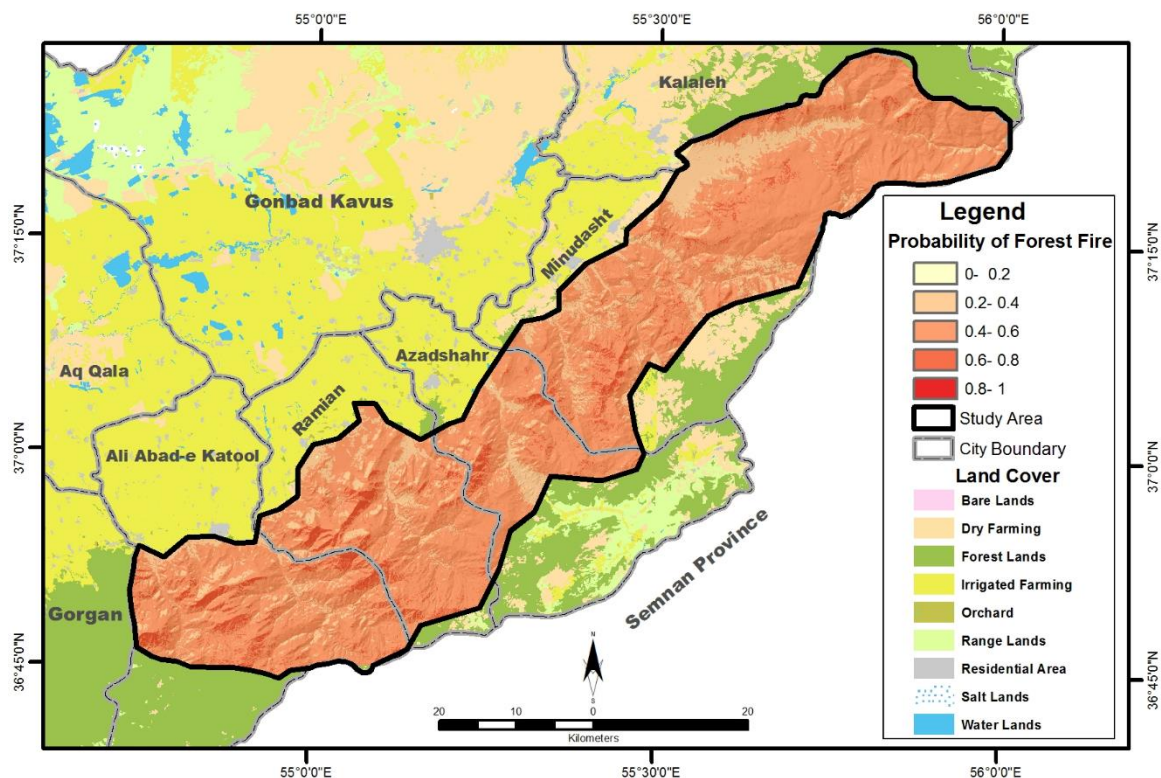


**Figure 2.9** Susceptibility map based on the spread of forest fire in Northeast Iran.

Our study provides novel information about the correlation between environmental, climatic and anthropogenic variables and fire durability and fire spread in Northeast Iran over a short time frame. Although fire severity is influenced by climate and forest density, forest roads are the single largest influencing parameter for extending the period of a fire, especially in forests with higher elevation, relatively lower road density and a weak road network coverage.

## 2.5 Conclusions

Forest fires present a real threat to the forest resources of Northeast Iran. Our results indicate that with increasing cumulative days after the onset of a fire, the burned areas also extended at a rate of 303.5 ha/day during November and December of 2010, resulting in burning about 4% of total forested area in less than one month. We compared the factors that influenced the duration and spread of those wildfires. Forest density had a significant influence on the duration and spread of wildfires among the environmental parameters, whereas topographic parameters (slope, aspect and plan curvature) did not. Spatial analysis showed that large fires occurred in those regions with high forest density, such as southwestern and southeastern parts of our study site. We also found an intriguing relationship between fire severity (durability and spread of fire) and daily mean temperature, while wind speed had a significant influence only on the duration of the fire. There were no significant correlations between fire severity and other climate factors (daily precipitation and humidity) during the forest fire. In Iran, most forests have a weak forest road network, and thus access to the entire forest is impossible. There was a high proportion of forest fires in areas with low forest density and also a weak road network coverage. Spatial analysis showed that most wildfires occurred in areas with a low-density population and at a long distance from public roads, although it is likely that other anthropogenic activities may have affected the expansion of fires. We suggest that studies on the influence of anthropogenic activities such as recreation, timber harvesting, mining and farming on fire severity would be useful. Susceptibility fire maps showed that the vast majority of forests are located in the medium-class severity of the fire, or higher, where there is a serious risk of fire due to the weak road coverage of the study area. The need for forest roads is obvious not only in commercial forests but also in protected forests, as they provide access and line breaks for suppressing fires.

## Acknowledgements

The authors would like to thank the reviewers for helpful suggestions that allowed us to improve this paper.



---

## **Spatiotemporal Drought Evaluation of Hyrcanian Deciduous Forests and Semi-Steppe Rangelands Using Moderate Resolution Imaging Spectroradiometer Time Series in Northeast Iran**

Omid Abdi, Zeinab Shirvani, Manfred F. Buchroithner

### Author contributions:

Omid Abdi designed the work and implemented geostatistical modelling, time-series image analysis, autocorrelation-statistical analysis, and writing the article.

Zeinab Shirvani contributed to extract human-caused degraded vegetation and analyse climate database.

Manfred F. Buchroithner reviewed the article and supervised at all stages of the study.

### Citation:

Abdi, O.; Shirvani, Z.; Buchroithner, M.F. Spatiotemporal drought evaluation of Hyrcanian deciduous forests and semi-steppe rangelands using moderate resolution imaging spectroradiometer time series in Northeast Iran. *Land Degrad. Develop.* **2018**, *29*, 2525–2541, doi:10.1002/ldr.3025.

### 3.1 Abstract

Advanced MODIS data have provided diverse products for assessing and monitoring natural vegetation affected by droughts. Between 2000 and 2016, we estimated monthly precipitation anomalies in the deciduous forests and semi-steppe rangelands of northeastern Iran using Kriging models, and analysed 16-day vegetation anomalies using vegetation greenness and water content indices—including the Enhanced Vegetation Index (EVI), the Normalized Difference Vegetation Index (NDVI), and the Normalized Difference Water Index (NDWI). Vegetation anomalies showed high positive responses to inter-seasonal precipitation anomalies over the 17 years and low positive responses to monthly precipitation deficits during critical droughts. Forest and rangeland anomalies recorded higher Moran's coefficients based on the NDVI ( $I = 0.253 \pm 0.102$ ) and NDWI ( $I = 0.284 \pm 0.087$ ) with inter-seasonal precipitation anomalies, respectively. Throughout critical droughts, the NDWI anomalies showed higher coefficients with monthly precipitation deficits for both forests ( $I = 0.0716 \pm 0.059$ ) and rangelands ( $I = 0.125 \pm 0.0615$ ). Nevertheless, there were only significant differences between the Moran's coefficients of the three vegetation indices for rangelands ( $F = 2.873$ ;  $P < 0.05$ ). BiLISA maps indicated that sparse forests show higher spatial associations with drought conditions (High-high cluster), whereas dense forests experienced lower stresses by severe droughts (High-low outlier) during drought periods. Meanwhile, some severe vegetation stresses occurred at locations with low droughts (Low-high outlier), which indicate the impact of other significant climate-induced disturbances on vegetation anomalies.

### 3.2 Introduction

Droughts are a worldwide and recurring natural hazard with an extensive range of adverse impacts on natural ecosystems, social communities and the global economy [19], which rank first among all the natural disasters in the world (<http://www.emdat.be/>). Generally, droughts are defined as long-term dry conditions in affected areas by periods of several weeks to months with rainfall that is significantly below normal levels [20]. However, droughts are classified,

based on their effects, into climatological, agricultural, hydrological and socioeconomic, but forest drought is also significant since its impacts on the ecosystem services [134].

Iran has experienced severe droughts in different periods during the last three decades [135]. Although droughts have been extensively studied from meteorological and hydrological perspectives in different climatic zones of Iran [136–139], their consequences on the vegetation have been explored in only a few research studies dealing with crops [140,141], irrespective of natural vegetation such as forests and grasslands. Numerous forest disturbances such as deforestation [83] and forest fires during drought periods were reported in different studies [84,142] in the northern part of Iran. By utilizing the Palmer Drought Severity Index (PDSI), Zoljoodi & Didevarasl [143] demonstrated that Iran experienced severe droughts during 1999–2002. This research was particularly the case in the northwestern and the northeastern parts of Iran. Likewise, Kazemzadeh & Malekian [139] have reported on severe meteorological and hydrological droughts in the northwestern part of Iran in 2007–2008 and 2010–2011, respectively. They showed that the majority of this region was suffering from severe hydrological drought in comparison to meteorological drought.

Today, satellite imagery offers widespread capabilities for monitoring the effects of drought on climatic variables, canopy physiology and disturbance feedback such as wildfires, tree mortality and yearly growth reductions [144–146]. The time-series of Advanced Very High Resolution Radiometer (AVHRR) data have been extensively used for environmental monitoring and documenting historical variations in climate and vegetation conditions using its derived NDVI and thermal infrared spectrum in the forested regions and grasslands for about three decades [147–149]. For example, Jong et al. [27] reported a strong spatial relationship between the variability of climatic parameters with the anomalies of forests and closed shrublands using the NDVI time series throughout the world from 1982 to 2008, in locations which browning anomalies predominated the greening anomalies.

To date, the Moderate Resolution Imaging Spectroradiometer (MODIS) onboard NASA's Terra satellite has provided monitoring of the terrestrial vegetation in fine spatial, radiometric and temporal resolutions [150], which has led to the emergence of new perspectives on drought assessment and monitoring in the world [151] as compared to the AVHRR data.

Moreover, scholars have integrated meteorological variables and derived vegetation indices from the MODIS sensor to assess spatiotemporal patterns of droughts in forest canopies [152–155] and rangelands [156]. For this purpose, vegetation indices (VIs), including vegetation greenness indices and vegetation water indices are designed to retrieve vegetation compositions, and their biophysical and structural features as well as their spatiotemporal changes by utilizing rationing between visible, near-infrared and shortwave-infrared channels of satellite data [157]. For example, MOD13Q1 includes vegetation greenness such as the EVI, NDVI and spectral channels (visible, NIR and SWIR) for deriving further indices, as well as pixel reliability information for checking the quality of NDVI and EVI [158].

Some researchers have challenged the capabilities of MODIS data to detect droughts in densely forested areas. For example, Atkinson et al. [31] analysed 11 years of derived vegetation indices (EVI and NDVI) from MODIS at a spatial resolution of 5.6 km for detecting the response of Amazonian vegetation to drought, and they reported that there was no significant variability between the VI standardized anomalies of drought years and non-drought years. Likewise, Samanta et al. [159] found no relationship between drought severity and EVI greenness values for Amazonian vegetation in the 2005 drought. The majority of these studies applied satellite images with low spatial resolution and short time series which gives credence to the argument that available remote sensing data and approaches are unable to detect anomalies in vegetation greenness during drought conditions. In contrast, some studies concluded that new leafage –at the top of the canopy– cause an increase in the near-infrared reflectance and increased greenness values of satellite-based indices during the dry season in the humid forests [160,161]. For example, Xu et al. [30] showed a significant and lasting decline in the EVI and NDVI values of Amazonian vegetation during the 2010 drought. Furthermore, Zhao et al. [162] compared the responses of natural vegetation to different stages of the 2009-2010 drought in China using MODIS NDVI and PDSI. Their results showed that the growth of grasslands and woody savannas were disturbed in all stages of drought, while forests only responded to the extreme droughts. Some researchers represented a higher sensitivity of densely-forested areas to MODIS water indices than to MODIS greenness indices. Anderson et al. [152] showed a positive spatial association between the EVI and tree mortality, but a negative association between the NDWI and tree mortality in Amazonian forest canopies during the 2005 drought. Gu et al. [156]



reported a strong spatial association between the NDVI and NDWI anomalies with the 2001-2006 drought conditions in the central grasslands of the United States. Moreover, their analysis showed that NDWI was more sensitive than NDVI to drought conditions. Caccamo et al. [163] reported that although vegetation greenness indices and vegetation water indices were sensitive to time-steps and time-lags of the Standardized Precipitation Index (SPI) droughts, the SWIR-based indices such as the Normalized Difference Infrared Index-band 6 (NDIb6) and the Normalized Difference Infrared Index-band 7 (NDIb7) demonstrated stronger performance than the visible-NIR indices such as NDVI and EVI in the high biomass ecosystems.

This study is designed to determine the periods of drought events which occurred in northeastern Iran during the last three decades (1987-2016) using the SPI. Also, we will explore the probabilistic anomalous values in the vegetation greenness values through EVI and NDVI, as well as in the vegetation water values through NDWI indices of MODIS VI products' time series (2000-2016). Finally, we will evaluate the possible spatial associations between the anomalous-MODIS-vegetation values and the SPI drought severity over the specified drought periods. Specifically, our goal is to find out an appropriate response to the following questions:

- In which periods did the northeastern part of Iran experience severe droughts?
- Did deciduous broadleaved forests and grasslands anomalies demonstrate positive responses to the inter-seasonal and monthly precipitation anomalies over the last 17 years?
- Which MODIS-derived vegetation indices (EVI, NDVI, and NDWI) has the strongest spatial correlation with the severity levels of the inter-seasonal and monthly SPI droughts?

## 3.3 Materials and Methods

### *3.3.1 Study area description*

We focused our research on the province of Golestan with an area of 21,910 sq.km, including Atrak (7,931 sq.km), Gorganrood (10,826 sq.km) and Qare-sou (3,153 sq.km) basins in the northeast of Iran (Figure 3.1). These basins are heterogeneous based on the land-cover types,

topographic complexity, and climatic regimes. The Qare-sou and Gorganrood basins are covered by dense natural deciduous forests, reserved forests, summer rangelands with high-quality forage, protected areas, fertile farmlands, and crowded residential areas, while, Atrak basin consists of semi-steppe winter rangelands, dry-farmlands, and sparse residential areas. The forests are the end part of Hyrcanian forests with rich deciduous broad-leaved tree species such as chestnut-leaved oak (*Quercus castaneafolia*), hornbeam (*Carpinus betulus*), velvet maple (*Acer velutinum*), Persian parrotia (*Parrotia persica*), elm (*Ulmus glabra*), etc. [164]. The elevation ranges between -30 meters in the northern parts and 3,360 meters in the south parts. According to the De-Martom climate classification system, the climate regime includes humid and semi-humid in Gorganrood and Qare-sou, and semi-arid in Atrak. The temperature varies between -5.5 and 33°C [165]. The minimum and maximum precipitation recorded 230 and 866 mm in Atrak and Gorgan-rood, respectively. This region has experienced severe droughts over recent decades [143], which led to irreparable damage to natural vegetation and crop productions.

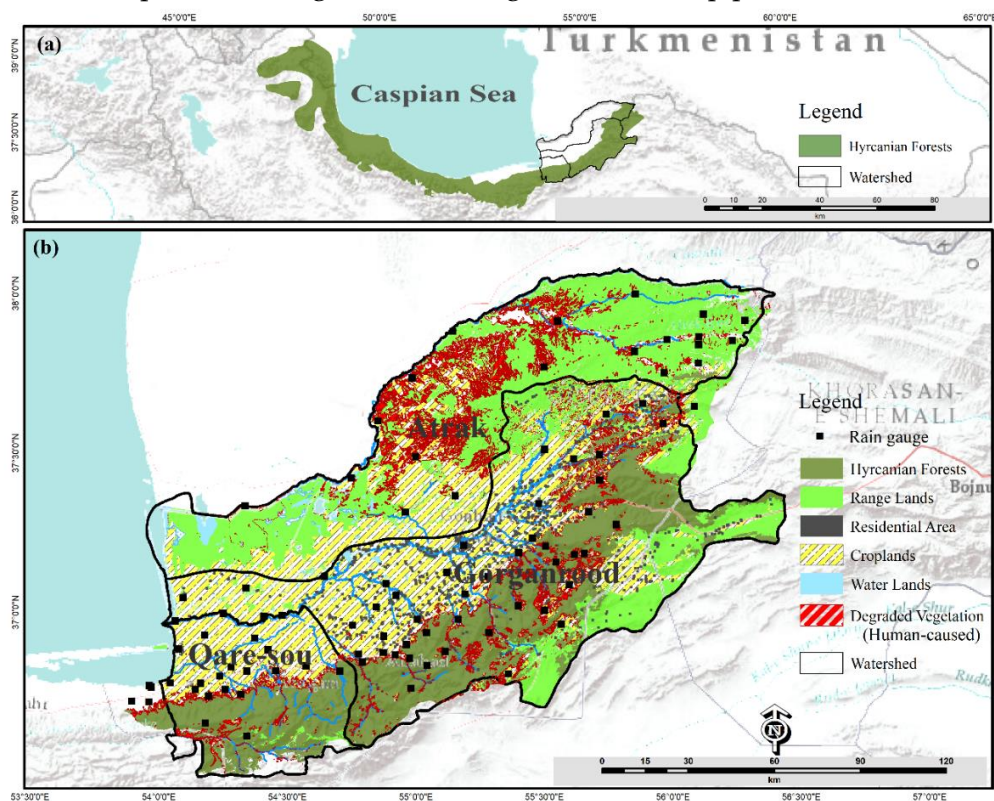


**Figure 3.1** Location of the Hyrcanian forests and Atrak, Gorganrood and Qare-sou watersheds (a) and distribution of land cover types as well as degraded vegetation (b) in the northeast of Iran.

### 3.3.2 Vegetation Indices (VIs)

We obtained 16-day MODIS VI products (MOD13Q1) at 250-meter spatial resolution from the online database of NASA Land Processes Distributed Active Archive Center (LP DAAC) from February 2000 to December 2016. The standard MOD13Q1 product consists of the reflectance spectra (red: 0.6-0.7  $\mu\text{m}$ , band 1; NIR: 0.7-1.1  $\mu\text{m}$ , band 2; blue: 0.459-0.479  $\mu\text{m}$ , band 3; SWIR: 2.105-2.155  $\mu\text{m}$ , band 7), and some useful ancillary data such as vegetation index quality and pixel reliability to remove cloud-contaminated pixels. Moreover, MOD13Q1 offers two applied vegetation greenness indices, i.e., NDVI and EVI for assessing vegetation anomalies, which are obtained from the visible and NIR bands as follows:

$$NDVI = \frac{(\rho_{NIR} - \rho_{red})}{(\rho_{NIR} + \rho_{red})} \quad (3.1)$$

$$EVI = G \times \frac{(\rho_{NIR} - \rho_{red})}{\rho_{NIR} + (C_1 \times \rho_{red} - C_2 \times \rho_{blue}) + L}, \quad (3.2)$$

where  $\rho$  is the atmospheric corrected spectral bands,  $G$  is the gain factor ( $G=2.5$ ),  $L$  is the canopy background adjustment ( $L=1$ ),  $C_1$  and  $C_2$  are the coefficients computed for decreasing the effects of scattering and absorption onto the vegetation ( $C_1=6$  and  $C_2=7.5$ ) [166]. These coefficients and corrections increase the EVI sensitivity to retrieve differences and abrupt changes in the high biomass forests [158]. Besides, we derived the NDWI from the NIR and SWIR spectral bands over the 17 years as Equation 3.3 [29]. The NDWI is used to estimate the vegetation water content due to the less sensitivity of the SWIR to saturation in comparison with the used bands in the EVI and NDVI [152].

$$NDWI = \frac{(\rho_{NIR} - \rho_{SWIR})}{(\rho_{NIR} + \rho_{SWIR})} \quad (3.3)$$

### 3.3.3 Estimation of precipitation by Kriging

Monthly precipitation data over the spatial extent of the study area were obtained from various rain gauges, with a minimum of 24 stations in 1987 and a maximum of 94 stations in 2016. Kriging methods were used to estimate monthly precipitation from recorded historical data. Kriging is a geostatistical approach to providing an optimal, unbiased, and generalized

the least-square interpolator that minimizes expected error variance by fitting a semivariogram model [167]. Semivariogram is a pre-implementation step of geostatistical modelling to explore spatial autocorrelation among measured data, which is defined as half of the average squared difference between the values at  $z(x_i + h)$  and  $z(x_i)$  as indicated in Equation 3.4 [168]:

$$\gamma(h) = \frac{1}{2n(h)} \sum_{i=1}^{n(h)} [z(x_i + h) - z(x_i)]^2, \quad (3.4)$$

where  $n(h)$  is the number of paired rain gauges within a specific distance and direction. The smaller values of  $\gamma(h)$  represent a stronger spatial autocorrelation between paired values of  $z(x_i)$  and  $z(x_i + h)$ , and vice versa. To find the best-fitted model, we tested different variogram types (e.g. Spherical, Gaussian, Pentaspherical, Tetraspherical, Rational quadratic and Stable) using weighted least squares, and key properties of the semivariogram, i.e. sill, nugget, and range. Then, three kriging models include Ordinary Kriging (OK), Lognormal Ordinary Kriging (LOK), and Empirical Bayesian Kriging (EBK) were applied. OK was used to estimate precipitation from data with the normal distribution and a specific semivariogram as follows [167]:

$$Z_{ok}^*(\chi) = \sum_{i=1}^n \omega_i(\chi) z(x_i) + [1 - \sum_{i=1}^n \omega_i(\chi)] m(\chi), \quad (3.5)$$

where  $Z_{ok}$  is the linear regression estimator,  $Z(\chi)$  is the measured precipitation at the location  $\chi$ , all  $x_i$  values are equal to  $n$  rain gauge stations,  $\omega_i(\chi)$  is the weight, and  $m(\chi)$  is the mean of monthly precipitation.

LOK was used to take account of the strong positive skewed distribution of the few precipitation data with a very large or small value as well. We applied the logarithmic transforms onto the skewed precipitation data, and after estimation by ordinary kriging, we reverted the transformed data to the original precipitation values as indicated in Equation 3.6 [169].

$$Z_{lok}^*(x_i) = \exp \left[ \hat{\gamma}(x_i) + \frac{\sigma^2(x_i)}{2} \right], \quad (3.6)$$

where  $\hat{\gamma}(x_i)$  is the transformed estimation by lognormal kriging,  $\sigma^2(x_i)$  is the estimation variance of lognormal kriging, and  $Z(x_i)$  is the back-transformed of estimation of the original precipitation data.

EBK was used to interpolate precipitation data with uncertainty in semivariogram parameters or small datasets. EBK automatically minimizes the error estimations by many semivariogram models (power, linear and thin-plate spline) rather than a single semivariogram model [170].

Finally, we compared the goodness of fit of all the used kriging methods by the cross-validation method. This method continuously excludes a measured sample, then interpolates the values from the excluded observation and compares the estimated value with the measured value [171] using the mean error (ME), root mean squared error (RMSE) and root mean square standardized error (RMSSE) as given below:

$$ME = \frac{\sum_{i=1}^n z_{(x_i)} - z^*_{(x_i)}}{n} \quad (3.7)$$

$$RMSE = \sqrt{\frac{1}{n} \sum_{i=1}^n [z_{(x_i)} - z^*_{(x_i)}]^2} \quad (3.8)$$

$$RMSSE = \sqrt{\frac{1}{n} \sum_{i=1}^n [(z_{(x_i)} - z^*_{(x_i)}) / \sigma^*_{(x_i)}]^2}, \quad (3.9)$$

where  $z_{(x_i)}$  and  $z^*_{(x_i)}$  are measured and estimated precipitation values at location  $x_i$ , respectively,  $\sigma^*_{(x_i)}$  is the standard deviation, and  $n$  is the number of rain gauges. The ideal monthly model was chosen based on the smallest RMSE, ME near to zero, and RMSSE near to one (Supporting information is found in Table 3.S1). When RMSSE is greater or less than one indicating an unstable model, particularly during the adjustment of parameters of Kriging models, and when it is close to one indicating the reliability of estimated standard errors [172].

### 3.3.4 Excluding pixels subject to anthropogenic activities

To differentiate vegetation anomalies induced by drought events from anthropogenic activities, we excluded anthropogenic-degraded-vegetation pixels from the non-anthropogenic-affected pixels between 2000 and 2016. Thus, Landsat images (Landsat 7 (ETM+) in 2000, and Landsat 8 (OLI) in 2016) were interpreted to identify degraded vegetation and expanded anthropogenic-based land-cover types. After radiometric and atmospheric corrections, spatial and spectral

enhancements were applied to the Landsat images to improve their resolutions in feature extraction. Then, supervised classifiers were carried out to classify land-cover types from selected multi-spectral images with high separability of spectral signatures at the beginning and the end of the period. Ultimately, we used the best distinctive change-detection method, i.e. post-classification [173] to exclude degraded vegetation (rangelands and forests) pixels induced by sprawling anthropogenic activities (dry-farming, irrigated farming, orchards, construction areas, and water bodies) from the non-anthropogenic-affected pixels throughout the study area over the last 17 years (Figure 3.1b).

### 3.3.5 Spatiotemporal analysis of vegetation and precipitation anomalies

We analysed 16-day spatiotemporal anomalies of vegetation indices (NDVI, EVI, and NDWI) over a 17-year (2000–2016) and monthly spatiotemporal anomalies of precipitation over a 30-year (1987–2016) to characterize the inter-seasonal and monthly pattern changes of vegetation during drought periods.

The standardized anomalies of inter-seasonal and monthly precipitation (SPI) were calculated based on the precipitation value of pixel  $i$  in the month  $m$  of year  $j$  ( $\chi_i$ ), the long-term mean ( $\mu_{im}$ ), and the standard deviation of precipitation ( $\sigma_{im}$ ) for the same month at this pixel (Equation 3.10). The SPI values show a period varying from normal to extremely dry (0 to -3) or extremely wet (0 to +3) conditions. Negative SPI values indicate drought conditions; we classified them into extremely dry ( $SPI \leq -2.00$ ), severely dry ( $-2.00 < SPI \leq -1.50$ ), moderately dry ( $-1.50 < SPI \leq -1.00$ ), mildly dry ( $-1.00 < SPI < 0.00$ ), and normal categories ( $0.00 \leq SPI$ ) [174].

$$SPI_{imj} = \frac{\chi_{imj} - \mu_{im}}{\sigma_{im}} \quad (3.10)$$

In addition, the standardized anomaly for a 16-day vegetation index (SDVI) was derived from the values of each vegetation index (NDVI, EVI, and NDWI) at pixel  $i$  in the 16-day  $p$  of the year  $j$ , the average spatial value of the vegetation index ( $VI_{ip}$ ) calculated over the 17-year study period for the time period  $p$ , and the standard deviation of the 17-year  $VI_{ip}$  values (Equation 3.11) [149].

$$SDVI_{ipj} = \frac{VI_{ipj} - \overline{VI_{ip}}}{\sigma_{ip}} \quad (3.11)$$

The SDVI values range from 0 to  $\pm 4$ , with negative values indicating below-normal vegetation conditions. Therefore, SDVI represents the 16-day vegetation conditions for vegetation indices at pixel  $i$ , during the growing season  $p$  of the year  $j$ , which compared to the long-term mean conditions for the same period along with the historical time-series data. Moreover, we classified SDVI values into the five vegetation-condition-classes based on the standard deviation of the three vegetation indices, including extreme stress ( $\text{SDVI} \leq -2.00$ ), severe stress ( $-2.00 < \text{SDVI} \leq -1.00$ ), moderate stress ( $-1.00 < \text{SDVI} \leq -0.50$ ), mild stress ( $-0.50 < \text{SDVI} < 0.00$ ), and normal conditions ( $0.00 \leq \text{SDVI}$ ) [175].

### 3.3.6 Spatial relationships between VIs and SPI

Moran's  $I$  evaluates a degree of spatial association between the attributes of a set of features located in neighbouring areas, which includes global autocorrelation, local autocorrelation, significance maps and cluster maps [176]. To identify the spatial correlation between inter-seasonal precipitation anomalies (inter-seasonal SPI) with vegetation anomalies throughout the 17 years—as well as the spatial relationship between monthly precipitation deficit (monthly SPI) and 16-day vegetation anomaly (SDVI) calculated from the standardized NDVI, EVI, and NDWI—bivariate local indicators of spatial association (BiLISA) was applied at the pixel  $i$  as follows [176,177]:

$$I = \frac{\frac{1}{W} \left( \sum_{i=1}^n \sum_{j=1}^n w_{ij} (Y_i - \bar{Y})(Y_j - \bar{Y}) \right)}{\frac{1}{n} \sum_{j=1}^n (Y_j - \bar{Y})^2}, \quad (3.12)$$

where  $n$  is the number of pixels, and  $Y_i$  and  $Y_j$  are identified values at the pixel  $i$  and  $j$ . The values of  $w_{ij}$  indicate the spatial weights matrix for measurement of the spatial association between the centroids of pixels, which were calculated based on the queen contiguity approach with the first order of neighbour in a  $3 \times 3$  matrix [178,179].  $W$  is the sum of weights of the matrices.

If SDVI and SPI exhibit strong spatial association in the positive direction, then Moran's  $I$  would be close to +1; no spatial association results in a Moran's  $I$  near zero; and strong association in the negative direction results in a Moran's  $I$  near -1 [176]. We tested the presence of global spatial autocorrelation based on 499 permutations with a pseudo-significance level

of 0.05. Using GeoDa™ [179], clusters were identified using the Moran scatterplot. Then, BiLISA cluster maps were coded as ‘High-high’ (the large values of SDVI surrounded by the large values of SPI), ‘Low-low’ (small values of SDVI surrounded by small values of SPI), ‘High-low’ (large values of SDVI surrounded by small values of SPI), ‘Low-high’ (small values of SDVI surrounded by high values of SPI), and ‘not significant’ [176].

## 3.4 Results

### *3.4.1 Spatiotemporal patterns of precipitation anomalies*

The results of estimated monthly precipitation from rain gauges indicate that the qualified models with higher accuracy varied in different months. Nevertheless, the OK models were performed more frequently than EBK from 1987 to 2016 (Supporting information is found in Table 3.S1.). Precipitation anomalies show different spatial and temporal variations throughout northeastern Iran between 1987 and 2016. These anomalies are shown with the overlapping periods of vegetation anomalies (2000-2016) in Figure 3.2a and b. This region experienced critical drought conditions in 2001, 2008, 2011 and 2014. The most severe of the droughts occurred in 2008, as about 15.4 and 6.4%, 66.8 and 20.8%, and 16.5 and 71.0% of forests and rangelands were affected by moderate, severe and extreme drought conditions, respectively (Figure 3.2c). Moreover, approximately 88.0% of forests experienced drought conditions in 2014 ranging from moderate (21.0%) to severe (51.7%) and extreme (15.2%) (Figure 3.2f). About 81.0% of the rangelands affected by moderate (3.0%), severe (73.3%) and extreme (4.0%) droughts in 2014 (Figure 3.2f). The drought event was remarkable in rangelands in 2001 as well, with 17.4% in the moderate category, 60.5% in the severe category and 16.0% in the extreme category. About 51.0% of forests affected by moderate (18.6%) and severe (32.2%) droughts in 2014 (Figure 3.2f).



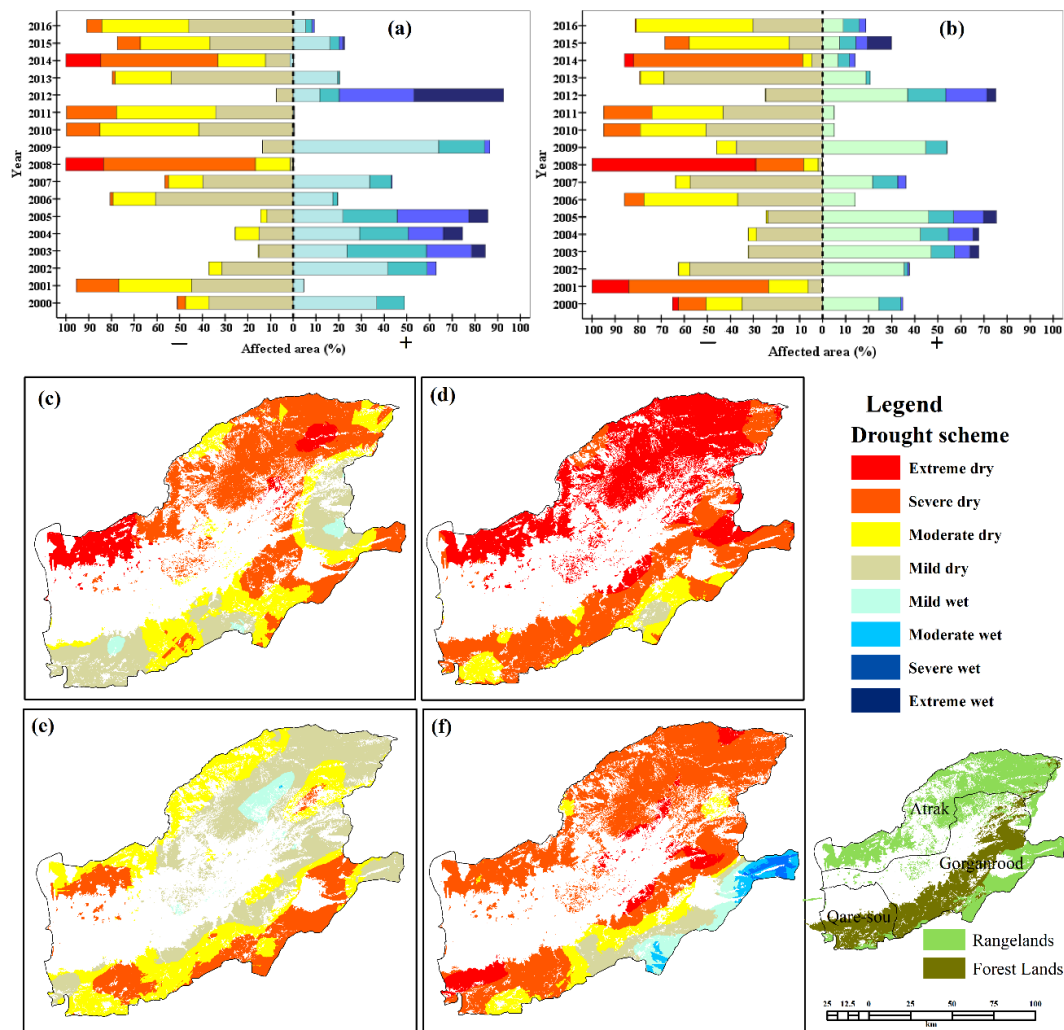


**Figure 3.2** The proportion of the forests (a) and rangelands (b) affected by different drought schemes compared to the long-term precipitation anomalies during the growing season of 2000-2016 (b), and four periods of severe droughts in 2001(c), 2008(d), 2011(e), and 2014 (f), respectively over the spatial extent of Northeast Iran.

Although all of the forest lands and about 95.0% of the rangelands experienced drought conditions in 2011, about 43.7 and 22.0% of the forests and 31.0 and 21.0% of the rangelands were in the moderate and severe categories, respectively (Figure 3.2e). In contrast, the severe wet conditions were observed in 2003-2005 and 2012 in both forests and rangelands. The most severe wet condition occurred in 2012 in the forests and the rangelands with 23.8 and 16.7% in the moderate category, 31.6 and 17.9% in the severe category and 8.4 and 3.9% in the extreme category, respectively (Figure 3.2a and b).

### 3.4.2 Spatiotemporal patterns of vegetation indices

The interpretation of Landsat images disclosed that anthropogenic drives degraded approximately 17,000 ha of forest lands and 51,500 ha of rangelands in 2000-2016 (Figure 3.1b). We excluded these areas from the vegetation anomalies affected by droughts throughout the study area.

The MODIS vegetation indices varied spatially and temporally across the northeastern part of Iran during 2000-2016. Forests and rangelands experienced severe anomalies in 2001, 2008, 2011 and 2014 as shown by the EVI, NDVI, and NDWI (Figure 3.3).

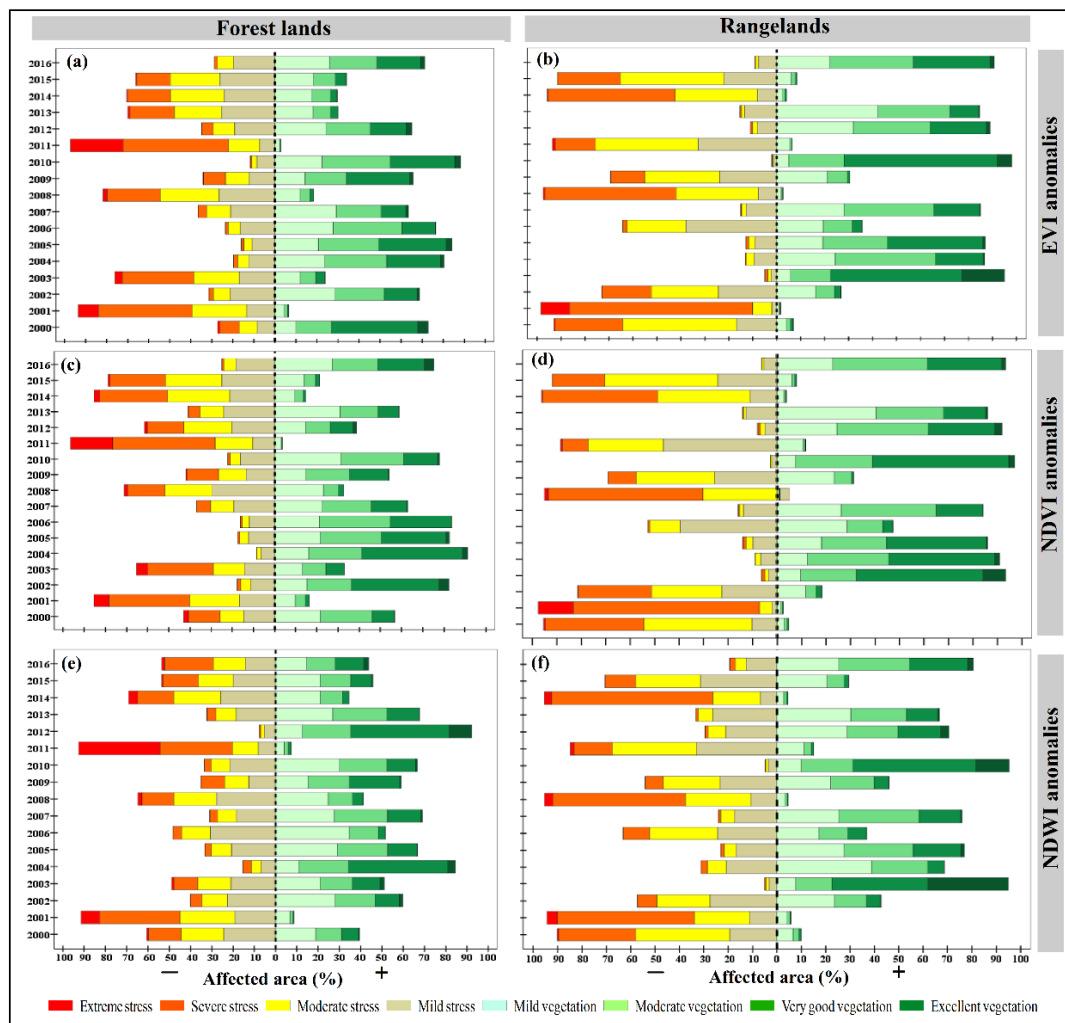


**Figure 3.3** Time-series distribution of proportion areas of the vegetation greenness anomalies calculated by the enhanced vegetation index (EVI; **a, b**) and the normalized difference vegetation index (NDVI; **c, d**), and the vegetation water anomalies calculated by the normalized difference water index (NDWI; **e, f**) from 2000 to 2016.

The highest inter-seasonal forest-greenness anomalies, moderate to extreme stress conditions, was detected in about 90.0 and 86.0% of forests based on the EVI and NDVI in 2011 (Figure 3.3a and c). We observed the highest inter-seasonal forest water-content deficits (NDWI) at about 84.0% of forests in both 2001 and 2011 (Figure 3.3e). Moreover, the vast majority of rangelands, affected by the moderate to the extreme of inter-seasonal greenness stresses, was obtained in 2001 (EVI: 96.5; NDVI: 95.5%), 2008 (EVI: 90.0; NDVI: 95.0%) and 2014 (EVI: 88.0; NDVI: 85.3%) (Figure 3.3b and d). The most critical inter-seasonal water-content deficits of rangelands occurred in 2014 (NDWI: 88.6%), and 2001 and 2008 (NDWI: 84.0%) (Figure 3.3f).

Additionally, 16-day VIs anomalies showed different variations during DOYs of the four drought periods. Figure 3.4a describes that 16-day EVI variability in forests was increasing during the May-June timeframe, while the rangeland anomaly was increasing from March to August in 2001. For example, about 87.0% of the forests and 94.5% of the rangelands experienced moderate to extreme stress conditions on DOY 145; these anomalies were higher in the dense forests (Qare-sou and central parts of Gorgan-rood) and summer rangelands with higher-quality forage (the southern of Gorganrood and central parts of Atrak) (Figure 3.5). Moreover, for the majority of the forests affected by moderate to extreme stress conditions during the growing season of 2011, Figure 3.4a shows that about 85.0% of them were in either the moderate category (17.1%), the severe category (46.6%) or the extreme category (21.5%) on DOY 129. Rangelands showed different schemes of stress during the other three periods, which were mostly dominated by the severe conditions of 2008 and the moderate conditions of 2014 (Figure 3.4a). Although the 16-day NDVI anomalies showed trends near the inter-seasonal EVI anomalies in rangelands during drought periods, their variations were slightly different in forest areas (Figure 3.4b). About 86.0 and 64.0% of the forests experienced upper-moderate stress conditions in 2011 and 2014, respectively. The most severe inter-seasonal forest anomalies occurred during July and August of 2011 as about 77.6% of the forests were affected by the moderate (18.2%), severe (44.2%) and extreme (15.2%) stress conditions on DOY 225, whereas the severe inter-seasonal NDVI anomalies of 2014 obtained during July through October timeframes in the spatial extent of the study area (Figure 3.4b).

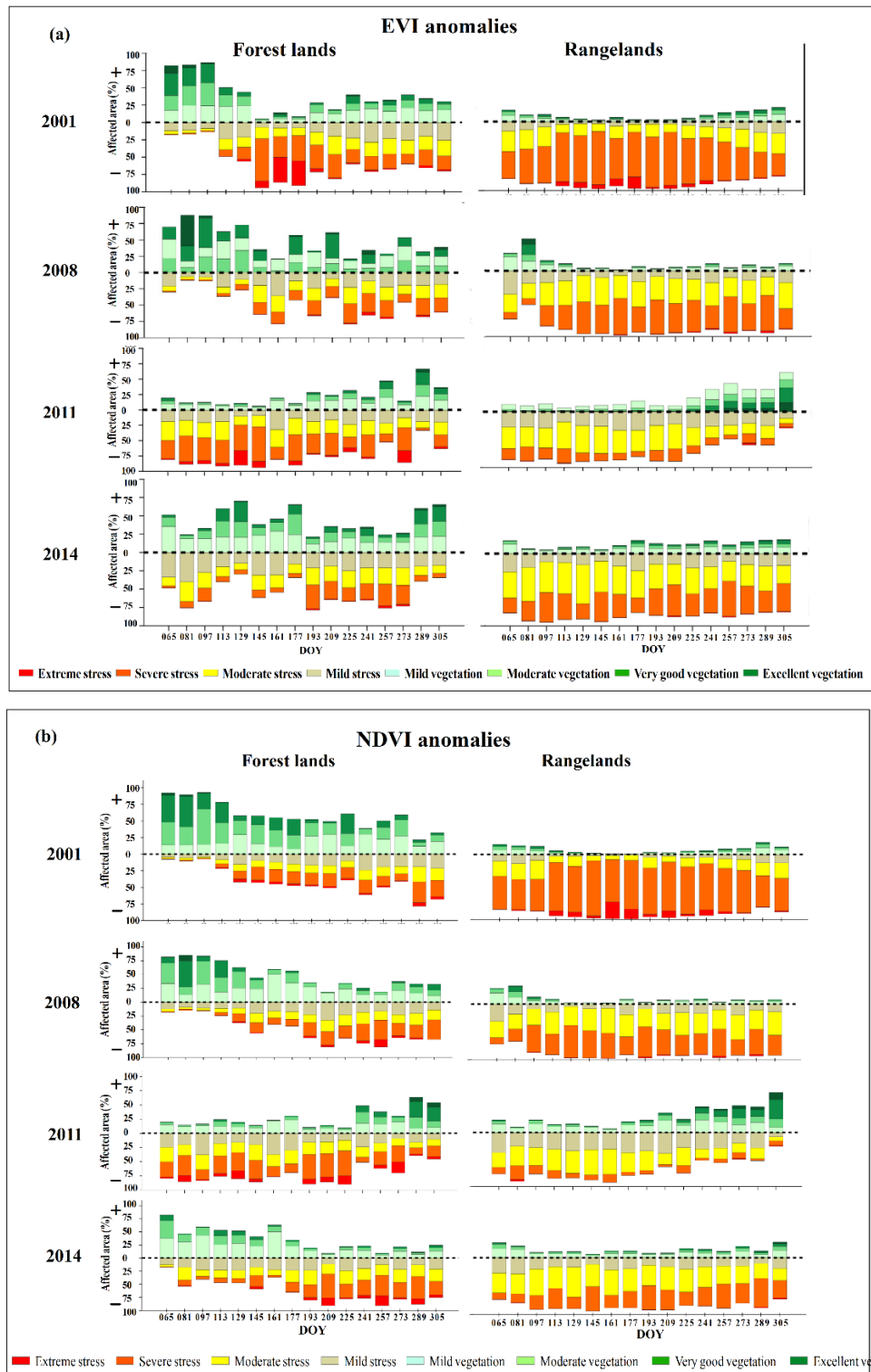


**Figure 3.4** Distribution of vegetation greenness anomalies during the growing seasons calculated by the enhanced vegetation index (EVI) for drought periods in the forests and rangelands (a). Distribution of vegetation greenness anomalies during the growing seasons calculated by the normalized difference vegetation index (NDVI) for drought periods in the forests and rangelands (b). Distribution of the vegetation water anomalies during the growing season calculated by the normalized difference water index (NDWI) anomalies for drought periods in the forests and rangelands (c).

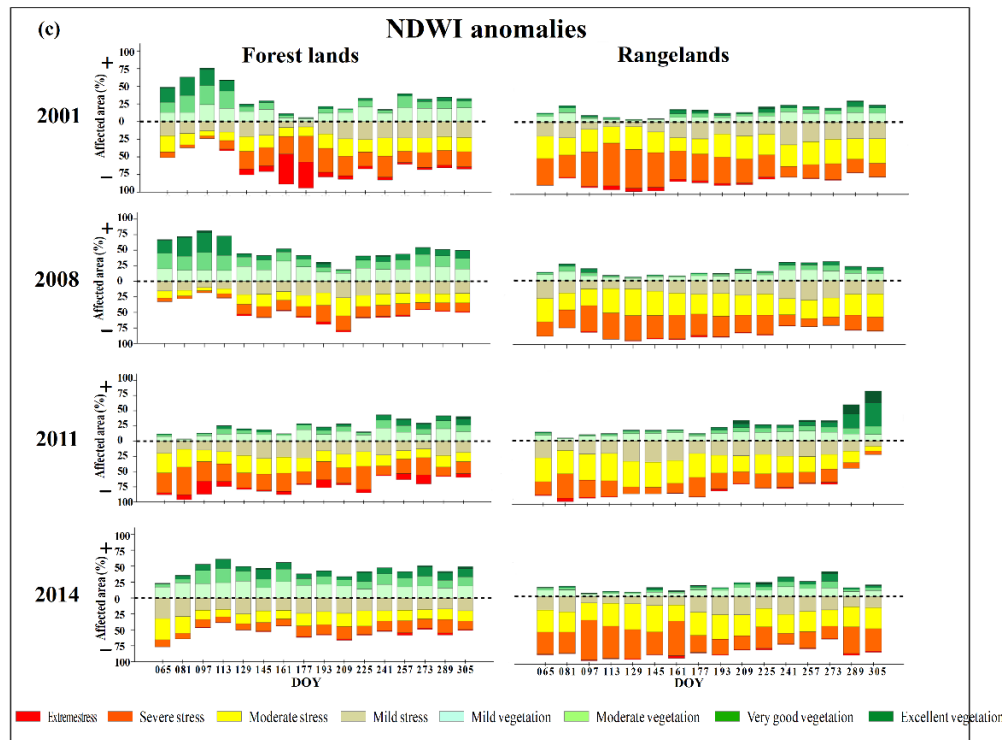


**Figure 3.4** Continued

The 16-day NDWI anomalies show that the most severe stress affected the entirety of the forests and rangelands in 2001 (Figure 3.5). Figure 3.4c indicates that severe conditions started in May and reached the highest peak in June in the forests, with more than 86.0% of them falling into the moderate (13.0%), severe (36.8%) and extreme (36.9%) stress categories on DOY 177. Likewise, the rangelands experienced severe and extreme anomalies in April through May, with the highest number recorded on DOY 129. Moreover, more than 60.0% of the forests experienced stress conditions ranging from moderate to extreme in six DOY (81, 97, 161, 193, 225 and 273) during the growing seasons of 2011. Rangelands, however, were predominantly affected by the severe stress conditions of 2014.

### 3.4.3 Spatial relationships between drought and the anomalies of MODIS VIs

#### 3.4.3.1 Inter-seasonal relationships

The inter-seasonal forest anomalies showed an overall positive spatial relationship with the SPI anomalies from 2000 to 2016 ( $P < 0.05$ ), however, some periods showed negative

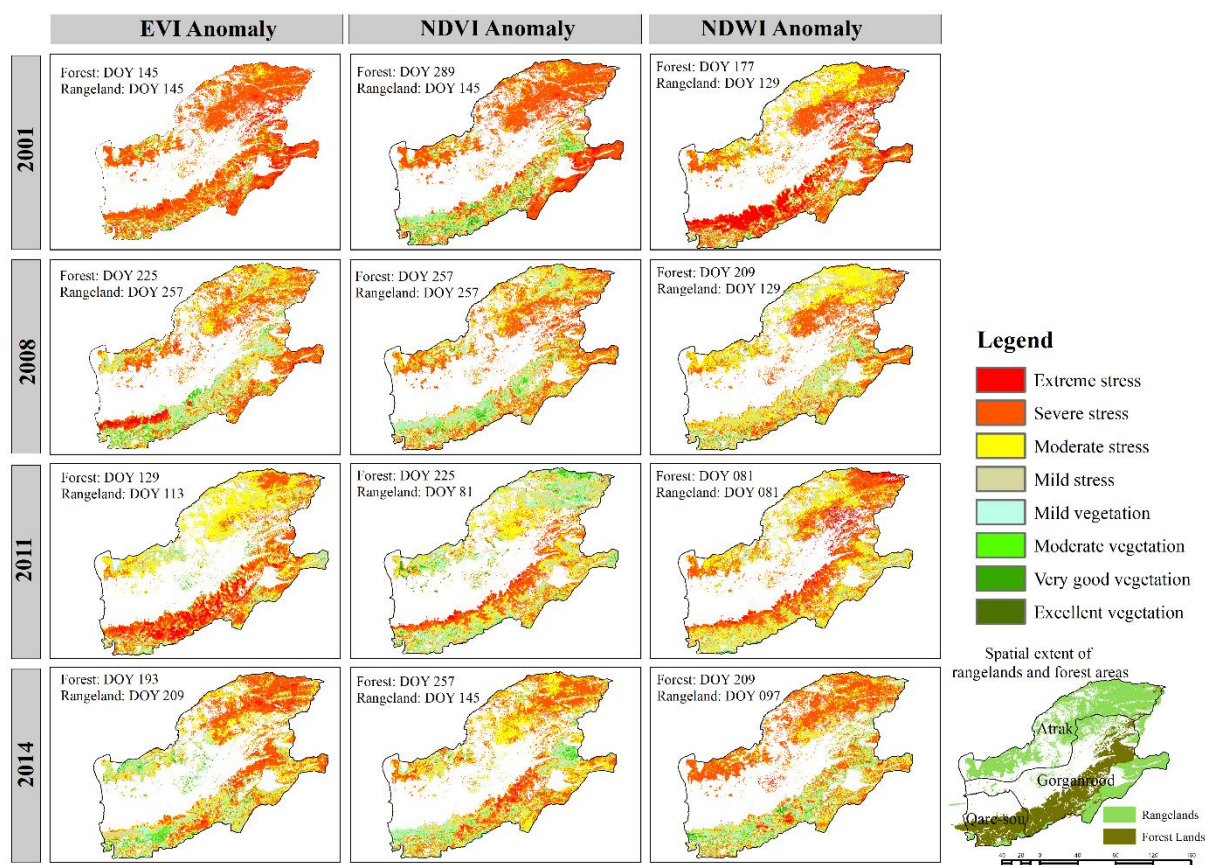


**Figure 3.5** The spatial extent of the severe dates of vegetation anomalies measured by the enhanced vegetation index (EVI), the normalized difference vegetation index (NDVI), and the normalized difference water index (NDWI).

coefficients with the VIs anomalies (Figure 3.6a). Statistically, distribution of *Moran's I* values indicates that forest anomalies based on the NDVI ( $I = 0.253 \pm 0.102$ ) recorded higher average coefficients than the NDWI ( $I = 0.205 \pm 0.099$ ) and EVI ( $I = 0.178 \pm 0.113$ ) anomalies in the study area. Nevertheless, there were no significant differences between the means of *Moran's I* of the three VIs based on the *F* test ( $F = 0.426$ ;  $P > 0.05$ ). Inter-seasonal forest anomalies recorded positive significant *Moran's I* coefficients with the critical drought periods (Figure 3.6a). For example, higher correlation coefficients were obtained for the EVI in 2001 ( $I = 0.382$ ), NDVI in 2008 ( $I = 0.2608$ ), NDWI in 2011 ( $I = 0.366$ ) and 2014 ( $I = 0.640$ ). Moreover, the inter-seasonal rangeland anomalies showed a positive spatial relationship with the SPI values based on all three VIs over the 17 years ( $P < 0.05$ ). The *Moran's I* coefficients show that the water content properties of rangelands based on the NDWI ( $I = 0.284 \pm 0.087$ ), were more sensitive than the greenness properties based on the NDVI ( $I = 0.178 \pm 0.071$ ) and EVI ( $I = 0.148 \pm 0.093$ ) to the SPI



values during the 17 years (Figure 3.6b). Nevertheless, the results of  $F$  test indicate that there exists no statistically significant differences between the average values of *Moran's I* of three VIs ( $F = 0.708$ ;  $P > 0.05$ ) for the rangelands as well. The correlation coefficients for the NDWI anomalies were higher than the NDVI and EVI anomalies in the critical conditions of 2001, 2008, 2011 and 2014; the NDVI shows stronger relationships with the precipitation deficit than the EVI in 2008, 2011 and 2014 (Figure 3.6b) as well.

#### 3.4.3.2 Monthly relationships

We explored the spatial relationships between monthly precipitation anomalies and 16-day VIs-anomalies of forests and rangelands during the growing months of the four drought periods (Figure 3.6c and d). Overall, distribution of spatial coefficients shows that the 16-day NDWI anomalies demonstrated higher values than the NDVI and EVI with  $0.0716 \pm 0.059$  for forests, and  $0.125 \pm 0.0615$  for rangelands. While the differences between the average *Moran's I* coefficients of the 16-day EVI, NDVI, and NDWI anomalies were not statistically significant for forests ( $F = 1.510$ ;  $P > 0.05$ ), but they were significant for rangelands ( $F = 2.873$ ;  $P < 0.05$ ). A summary of the spatial associations between monthly precipitation anomalies and 16-day MODIS VIs anomalies is presented for forests in Table 3.1a and rangelands in Table 3.1b. The *Moran's I* values indicate that the rainfall anomalies showed the highest positive spatial associations with the MODIS NDWI during the DOYs of 2001 and 2011, and the MODIS NDVI of 2008 and 2014 in the forest areas ( $P < 0.01$ ). Moreover, the majority of positive associations between precipitation anomalies and the anomalies of rangelands were observed in the MODIS NDWI during the DOYs of 2001, 2008, 2010 and 2011, and the EVI and NDVI anomalies of 2014 ( $P < 0.01$ ).

The local spatial associations between monthly rainfall anomalies and VIs anomalies mapped as local *Moran's I*, BiLISA significance maps and BiLISA cluster maps (Permutations of 499 and  $P < 0.05$ ) for each DOY of associated drought periods with vegetation anomalies are shown in the supplementary data (Figure 3.S1-S4). Specifically, the BiLISA maps for DOYs with the highest *Moran's I* (Figure 3.7) demonstrate that about 17.8% (DOY 177, NDWI), 17.9% (DOY 177, EVI), 17.2% (DOY 289, NDWI) and 26.9% (DOY 225, NDVI) of the forests were in the High-high clusters in 2001, 2008, 2011 and 2014, respectively. Likewise, about 32.4% (DOY 129, NDWI), 13.6% (DOY 97, NDWI), 17.9% (DOY 97, EVI) and 27.3% (DOY 177, EVI) of the rangelands were in the High-

high clusters of the VIs, chronologically. Furthermore, the spatial associations between locations with lower drought and lower vegetation-stress conditions were significant in given DOYs in Figure 3.7. About 18.9%, 15.7%, 31.7 and 17.2% of the forests, and about 7.2, 15.7, 14.0, and 11.8% of the rangelands located in the Low-low clusters during drought periods, respectively. On the other hand, locations with outliers (Low-high/High-low) have occupied less proportion of the area in comparison to the clusters (High-high/Low-low) in the studied DOYs. For example, about 10.34 and 6.12% of forests, and about 10.34 and 6.13% of rangelands located in the Low-high outliers based on the VIs in 2001 and 2008, respectively. While about 17.3 and 6.1% of the forests, and about 3.9 and 4.2% of the rangelands were in the High-low outliers in these times.

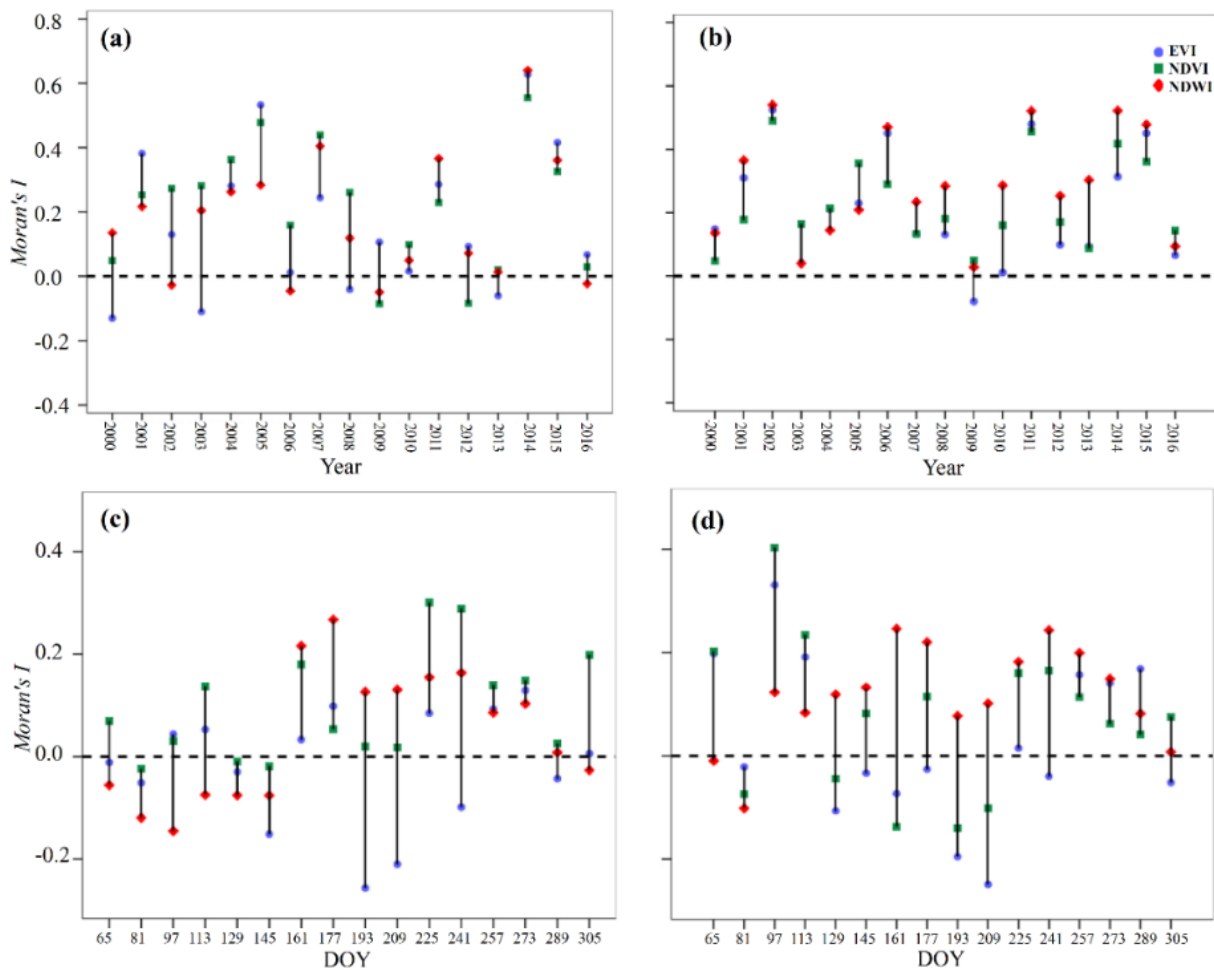


**Figure 3.6** Distribution of spatial correlation (Moran's  $I$ ) between the standardized precipitation index and the vegetation indices EVI, NDVI, and NDWI in the forests (a) and rangelands (b) during the growing season from 2000 to 2016, and DOYs (c and d) for drought conditions.



**Table 3.1** Obtained averages of *Moran's I* values between monthly rainfall anomalies (SPI) and 16-day VI anomalies (EVI, NDVI and NDWI) for the forest areas (a) and rangelands (b).

(a)

DOY	EVI anomaly				NDVI anomaly				NDWI anomaly			
	2001	2008	2011	2014	2001	2008	2011	2014	2001	2008	2011	2014
65	-0.1236	0.0211	0.1153	-0.0436	-0.0762	0.0098	0.1290	0.1957	-0.1738	-0.1509	0.0636	0.0393
81	-0.0714	-0.0343	-0.0262	-0.068	-0.1924	0.0037	0.0153 <sup>ns</sup>	-0.0481	-0.2890	-0.3816	0.0499	0.1006
97	0.1784	-0.4279	0.1415	-0.0541	0.1765	-0.2563	0.1225	-0.0621	0.0832	-0.4362	-0.1509	-0.1400
113	0.052	-0.1912	0.2004	0.0541	0.1397	-0.2678	0.1338	0.3169	0.1074	-0.4356	-0.1494	-0.0065 <sup>ns</sup>
129	-0.0712	0.0118	0.1586	-0.2616	-0.0462	0.0027 <sup>ns</sup>	-0.0096	-0.0055	0.1220	-0.2214	0.0702	-0.3128
145	-0.1485	-0.1542	0.0541	-0.2982	0.0099	0.0177	-0.0474	-0.1436	0.0731	-0.1774	0.0252	-0.3291
161	-0.1248	0.2761	0.0265	0.0400	-0.3202	0.3193	0.2063	0.1531	0.1190	0.3513	0.3135	-0.0501
177	0.0181	0.5229	-0.2615	0.1787	-0.4213	0.3121	-0.0119	0.1189	0.2094	0.3463	0.3256	-0.0589
193	-0.3440	-0.2267	0.2279	-0.2868	-0.3657	-0.0221	0.0609	0.1679	0.2576	-0.1569	0.1048	0.1480
209	-0.3150	-0.2060	0.1946	-0.2146	-0.3225	-0.0266	0.0623	0.2191	0.2658	-0.1845	0.1137	0.1476
225	0.1592	-0.3739	0.0542	-0.291	0.3628	-0.2359	0.2392	0.078	0.3050	-0.2824	0.0178	0.292
241	0.1663	-0.1448	-0.0553	-0.166	0.3533	-0.2230	0.2961	0.282	0.3091	-0.2928	0.0185	0.313
257	0.1844	0.1282	0.0335	0.0572	0.2327	0.2407	0.0373	0.0467	0.0864	0.0856	0.1177	0.0789
273	0.3541	0.2259	-0.0129	0.0329	0.3904	0.2192	0.0786	0.0599	0.1266	0.0929	0.1142	0.0690
289	-0.0123	0.5157	-0.0738	-0.1650	0.0516	0.5157	0.0052 <sup>ns</sup>	-0.1888	-0.4424	0.3418	0.3795	-0.3257
305	-0.0519	0.4352	0.0634	-0.1421	0.0394	0.3999	0.0035	-0.1565	-0.4548	0.3641	0.2223	-0.2753

(b)

DOY	EVI anomaly				NDVI anomaly				NDWI anomaly			
	2001	2008	2011	2014	2001	2008	2011	2014	2001	2008	2011	2014
65	0.2495	0.1743	-0.3299	0.2213	0.2041	0.2006	-0.2684	0.2402	-0.2261	0.1113	0.0450	-0.0642
81	0.2560	-0.2343	-0.4622	0.1916	0.0450	-0.1930	-0.4334	0.1880	-0.2770	-0.1697	0.0641	-0.0333
97	0.2809	0.3802	0.5592	0.0124	0.3035	0.5023	0.5476	0.0167	0.4957	-0.0467	0.1011	0.1452
113	-0.0786	0.2082	0.4017	0.1741	-0.0822	0.3328	0.1355	0.4257	0.4957	-0.0462	-0.1368	0.2134
129	-0.1674	-0.0567	-0.1566	-0.2354	-0.1604	-0.0259	-0.0620	-0.2108	0.4173	-0.1730	0.2281	-0.5181
145	-0.2698	-0.0346	0.0411	-0.0826	-0.2372	0.1402	0.0237	-0.0376	0.2609	-0.1201	0.3471	-0.5462
161	-0.1332	-0.2332	-0.0129	0.3758	-0.1526	-0.3137	-0.1213	0.2693	0.3649	0.4380	0.1270	0.1229
177	-0.1694	-0.1494	0.0972	0.4613	0.0421	0.0681	0.1609	0.4081	0.1860	0.3754	0.2543	0.1856
193	-0.1951	-0.1032	0.0069 <sup>ns</sup>	-0.3096	-0.2758	-0.1255	0.1305	-0.1535	0.2918	0.1029	0.0517	-0.1775
209	-0.2132	-0.2847	0.0202	-0.3055	-0.1206	-0.4261	0.1003	-0.0815	0.3537	0.1174	0.0855	-0.201
225	-0.0481	0.0062	0.0606	0.0235	0.3778	0.0461	0.2744	-0.2632	0.5529	0.1800	0.1838	-0.3597
241	0.0879	-0.1293	0.0022 <sup>ns</sup>	-0.0397	0.4069	0.0564	0.2728	-0.2857	0.4946	0.1506	0.1615	0.3251
257	0.1572	-0.0043 <sup>ns</sup>	0.2177	-0.2190	0.2386	-0.0429	0.1468	0.0807	0.3114	0.4965	0.087	-0.2944
273	0.1408	-0.0077 <sup>ns</sup>	0.4223	-0.2596	0.1467	-0.0226	0.2955	-0.2144	0.2430	0.5490	0.0552	-0.3611
289	-0.0026 <sup>ns</sup>	-0.0043	0.3411	-0.0046 <sup>ns</sup>	0.0009	0.0414	0.4061	-0.0025 <sup>ns</sup>	-0.3398	0.3640	0.2273	-0.0639
305	-0.1444	-0.0275	-0.0756	-0.0029	0.0031	0.1476	0.1609	-0.0041	-0.4057	0.3532	0.1559	-0.1406

*Note.* Positive values indicating significant direct spatial associations and negative values indicating vice versa spatial associations between monthly rainfall anomalies and 16-day VIs anomalies (p-value < 0.05, ns: p-value > 0.05). EVI: enhanced vegetation index; NDVI: normalized difference vegetation index; NDWI: normalized difference water index; SPI: standardized precipitation index.

## 3.5 Discussion

Rainfall anomalies show that the northeastern part of Iran has experienced severe meteorological droughts with shorter time lags during recent years, as the six lags between 2001 and 2008 decreased to two intervals between 2011 and 2014 (Figure 3.2). Nevertheless, our study confirms

the severe droughts reported by Zoljoodi & Didevarasl [143] in 1999 to 2002 and Kazemzadeh & Malekian [139] in 2007 to 2008 and again in 2010 to 2011 in northeastern Iran. This study adds that this area experienced severe drought in 2014 as well.

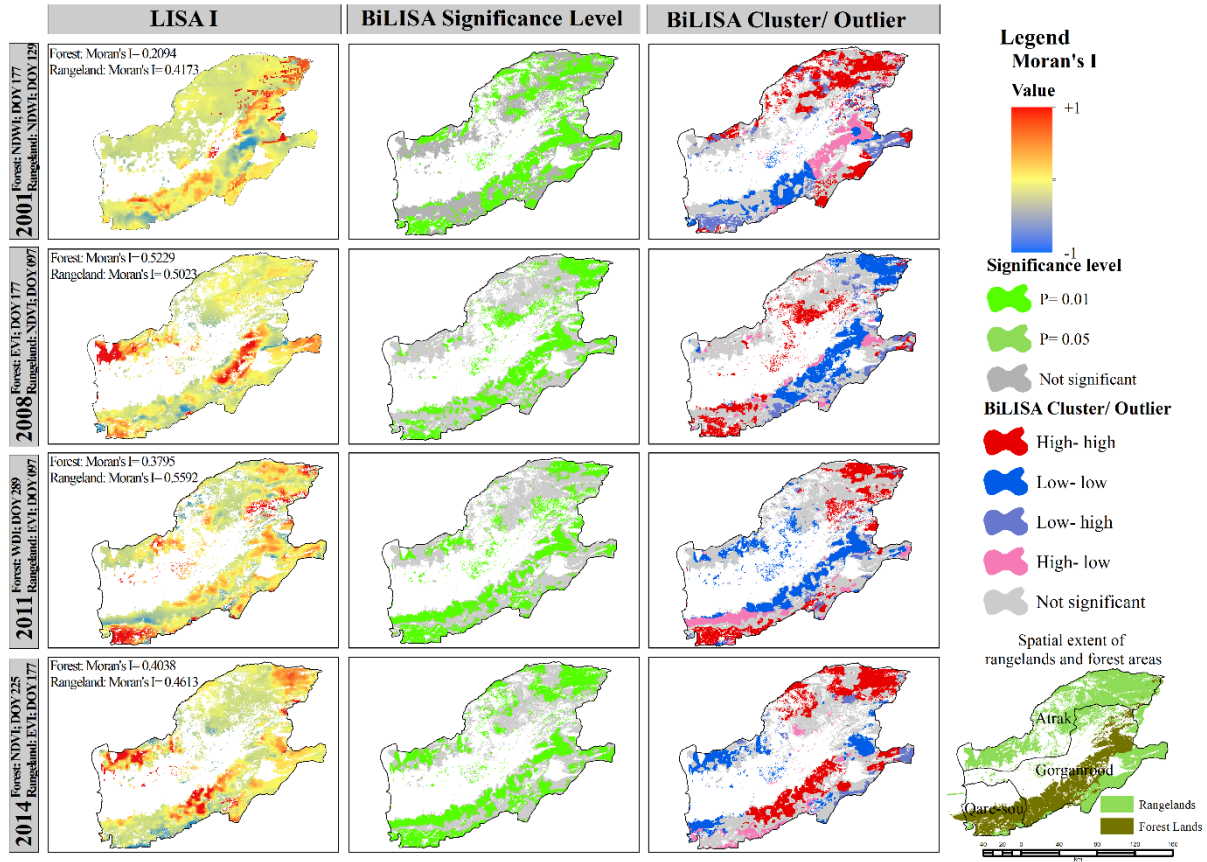


**Figure 3.7** Spatial variations of local *Morans'I* values, BiLISA significance levels and BiLISA cluster/outlier (significance level: 0.05 and randomization permutation: 499) of some DOYs with the high spatial relation between the anomalies of rainfall and the vegetation indices during drought periods. EVI: enhanced vegetation index; NDVI: normalized difference vegetation index; NDWI: normalized difference water index.

Moreover, Kriging methods enabled us to estimate the monthly rainfall with an acceptable validity over the spatial extent of the study area; hence, instead of calculating rainfall anomalies just in the location of rain gauges, we did so for all cells against prior studies [136–139]. This method decreased the errors related to the sporadic rain gauges, missing data and possible incorrect measurements of time-series rainfalls, and it provided an effective combination to assess the spatial relationships between vegetation anomalies derived from MODIS VI products and rainfall anomalies.

Although the inter-seasonal forest anomalies showed significant spatial correlation with the precipitation deficit during four drought periods, the *Moran's I* coefficients in 2008, with severe

to extreme drought, and 2011, with severe to extreme stress, were less than the coefficients of 2001 and 2014 (Figure 3.6a). Despite receiving above-normal precipitation in 2002, 2009 and 2012, forests showed low positive or negative responses to these wet conditions during the growing season (Figure 3.6a). It shows that the precipitation deficit is not the final climate variable for determining the forest anomalies of northeastern Iran. To investigate the possible impacts of other climatic parameters on the significant forest stresses in 2011 and 2014, we explored the land surface temperature (LST) anomalies (Figure 3.8) derived from Terra MODIS Land Surface Temperature and Emissivity L3 1 km product (MOD11A2) data for the studied period. We observed strong positive relationships between the forest-greenness anomalies with the LST anomalies in 2011 (NDVI:  $I = 0.159$ ; NDWI:  $I = 0.046$ ), and both greenness and water content anomalies in 2014 (NDVI:  $I = 0.207$ ; NDWI:  $I = 0.365$ ). Therefore, it is crucial to consider the impacts of other climatic and hydrological anomalies on the forest droughts as well.

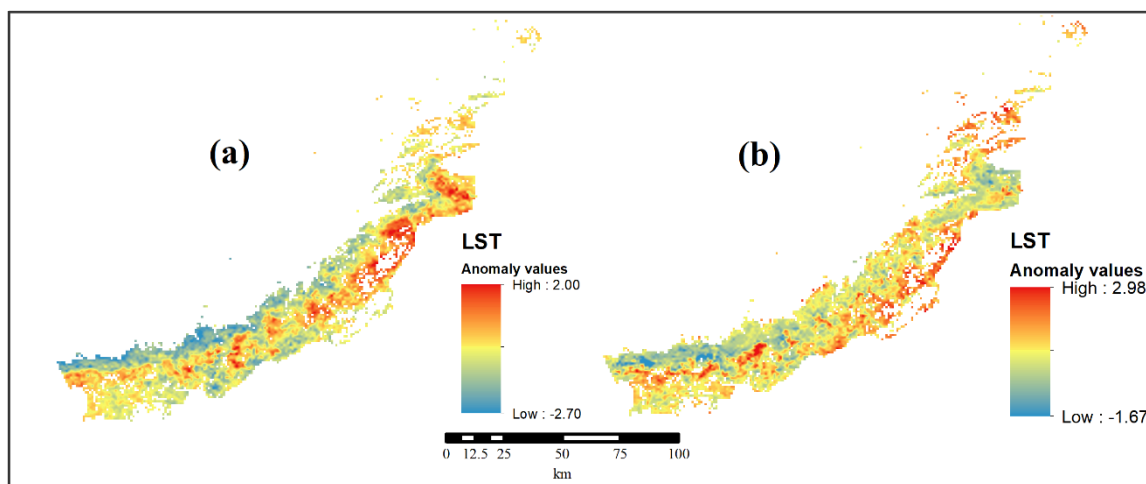


**Figure 3.8** The land surface temperature (LST) anomalies in the forest lands during 2011 (a) and 2014 (b) droughts.

The actual physiological state of forests does not entirely rely on the precipitation-based patterns, therefore; the MODIS vegetation indices determine the physiological forest variables and indicate their vulnerabilities to drought [154]. Some negative anomalies in 2002, 2009, 2012 and 2015, following drought periods, confirm that when a forest is affected by a critical drought, its status may remain disturbed for a longer time span [155]. The intensity of drought effects pertains to the drought duration and intervals in forests, which the 2008 drought has occurred six years after the 2001 drought while 2011 drought was following the 2010 drought as well as

2014 drought had two time lags with it (Figure 3.2a). The high correlation coefficients of the NDWI anomalies show the influence of long duration and short lag of droughts on disturbing the water content of forests in 2011 and 2014. Therefore, it is essential to be considered the impacts of precipitation deficit on the forest droughts from both climatic and biological aspects [154]. In contrast, inter-seasonal rangeland anomalies were more sensitive to the precipitation anomalies in comparison to the inter-seasonal forest anomalies. However, the responses of rangelands to drought condition was higher in deficiency of water content than the decline of greenness throughout the four drought periods (Figure 3.6b).

The analyses of the critical DOYs revealed that forests were affected by diminishing of water content during June to September timeframes of droughts, as the 16-day NDWI anomalies showed positive responses to the monthly precipitation anomalies from DOY 161 to DOY 273. The positive relationship between medium-term drought and forest condition was observed in the Mediterranean [154] and the eastern Baltic Sea [155] regions as well. The normal conditions of the winter season led to maintain the soil moisture and increased the water content of forests during the spring season of droughts, as the 16-day NDWI anomalies showed negative spatial relationships with the precipitation deficit till DOY 145 (Figure 3.6c). The 16-day rangeland-water-content anomalies showed positive responses to the monthly precipitation deficit from the beginning of April till the end of October during drought periods (Figure 3.7b), however, their greenness properties show positive coefficients in the beginning (DOY 65 to DOY113) and the last six DOYs (Figure 3.6d). The significant impact of drought conditions on the arable land vegetation in the beginning and the end of the growing season was reported in the eastern Baltic Sea region [155] as well.

The NDWI anomalies showed significant positive associations with drought intensity in the forest areas during 75% (DOY 97–DOY 237) and more than 85% of DOYs in 2001 and 2011, respectively (Table 3.1a). In the meantime, these associations were recorded in 75% (DOY 113–DOY 241) and greater than 90% of DOYs of rangelands in 2001 and 2011, as well. The *Moran's I* coefficients confirm that the NDWI anomalies were strongly associated with monthly rainfall anomalies in rangelands during 70% of the DOYs in 2008 (Table 3.1b). These findings indicate that variations in the vegetation water content against the vegetation greenness were highly correlated to the variations in precipitation patterns in the Hyrcanian deciduous broadleaf forests and semi-steppe rangelands of northeastern Iran. Previously, the higher sensitivity of the NDWI

to drought conditions in comparison with the NDVI was highlighted in the grasslands of the United States by Gu et al. [156] and in the dense biomass ecosystems by Caccamo et al. [163].

Although the NDVI anomalies showed significant positive correlations in at least 50% of the DOYs during growing seasons of drought periods, they only performed higher than the NDWI in the 2008 drought in forests and again in the 2014 drought in both forests and rangelands. Furthermore, the EVI anomalies demonstrated significant direct associations with the rainfall anomalies in the 2011 drought in the forests (60% of the DOYs) and rangelands (70% of the DOYs). These results confirm that severe drought conditions disturbed the greenness properties of the Hyrcanian forests and semi-steppe rangelands of northeastern Iran. Likewise, vegetation anomalies induced by rainfall deficits were presented by utilizing the EVI and the NDVI in the Amazonian vegetation during the 2010 drought [30], and by the EVI in Amazonian forest canopies during the 2005 drought [152] as well. Besides, Jong et al. [27] have demonstrated the greenness responses of natural forests and grasslands to climatic parameters via the NDVI time series in different stages of droughts.

The aggregated maps of BiLISA illustrate that the considerable portions of forests have experienced high stress surrounded by severe droughts, especially in 2001, 2008 and 2011. Figure 3.9 shows that about 92,600 ha (19.1%) and 111,000 ha (22.9%) of the forests based on the NDWI, and also about 100,000 ha (20.7%) and 22,000 ha (4.5%) based on the NDVI are located in the High-high cluster in more than 50% of the length of growing seasons of 2001, 2011, 2008 and 2014. The vast majority of these forests are located in the montane parts of the Qare-sou and Gorganrood watersheds, which are covered by tree species with low-growing stock volumes in all of the drought periods. Meanwhile, dense forests with higher stock volume values have experienced less drought and therefore less stress (Low-low cluster) in the medium-range altitudes (800-1,000 MASL) of the Qare-sou and Gorganrood (Figure 3.9). Moreover, BiLISA maps depict that rangelands have experienced high-stress conditions during severe droughts, especially in the northern parts of Atrak which have low-quality forage (winter rangelands). Figure 3.9 shows that about 136,000 ha (17.6%), 122,300 ha (15.8%) and 173,400 ha (22.5%) of the rangelands were in the High-high clusters based on the NDWI over 50% of the growing seasons in 2001, 2008 and 2011, respectively. On the other hands, the locations with significant outliers

scattered throughout the study area in the growing seasons of droughts. It can be concluded that some vegetation types were less affected by severe droughts (High-low). These locations consist of summer rangelands with high-quality forage in the south parts of Atrak, and also high dense forests with well survive species, which are under the forest management plans in the lowlands and mid-altitudes of the Qare-sou and Gorganrood (Figure 3.S1–S4). Furthermore, some locations with severe vegetation stress are surrounded by low drought events (Low-high), which represents to do further studies on the possible effects of other natural variables such as extreme temperature, vegetation evapotranspiration, soil moisture deficit and hydrological droughts on both rangelands and slightly lower forests. Likewise, severe forest disturbances induced by human activities [83] and forest fires [84] have reported in the northeast of Iran.

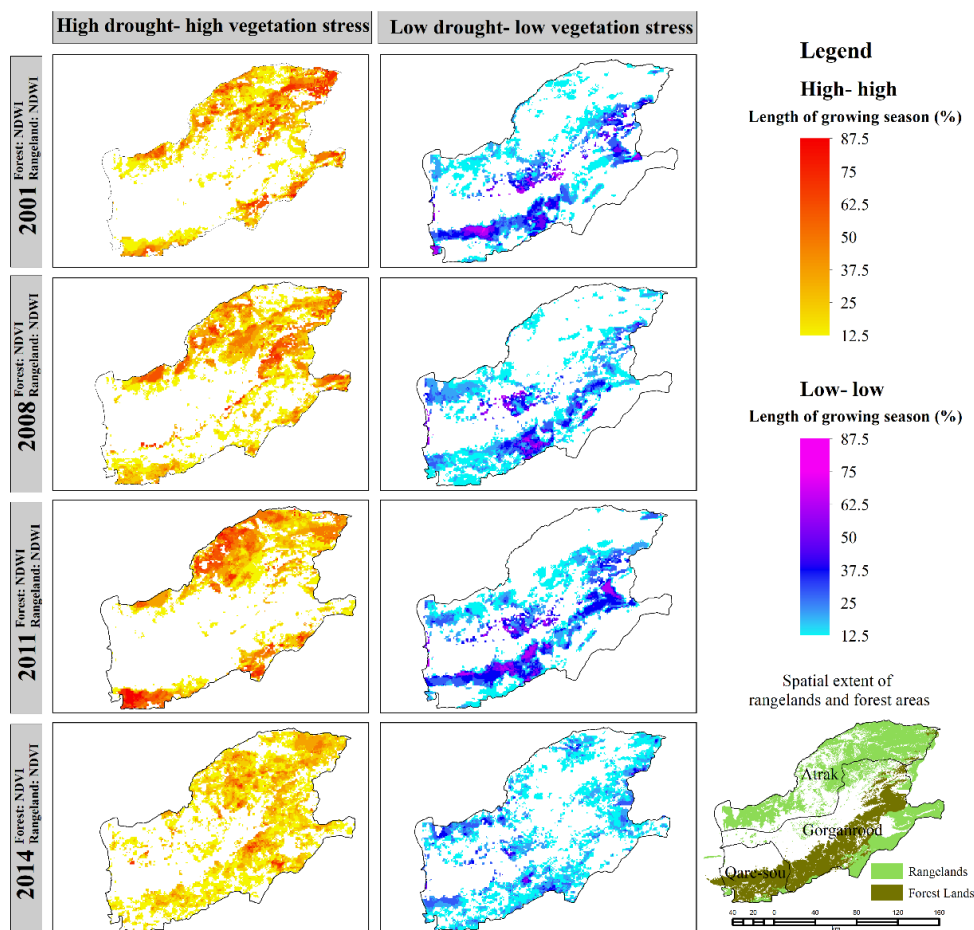


**Figure 3.9** Aggregated maps of BiLISA for clusters (High-high and Low-low) during growing seasons (March to October) of forests and rangelands based on the qualified vegetation indices for drought periods. EVI: enhanced vegetation index; NDVI: normalized difference vegetation index; NDWI: normalized difference water index.



The current study suggests that long time-series of 16-day MOD13Q1 data retrieved the spatial variability of deciduous broadleaf forests and semi-steppe rangelands to droughts relevant to their water-content and greenness properties in Northeast Iran. Conversely, using some satellite products with coarse spatial resolution and short time-series resulted in their restrictions for retrieving of vegetation anomalies to drought conditions such as Amazonian forests in some previous studies [31,159].

### 3.6 Conclusion

We explored the inter-seasonal and monthly anomalies of precipitation and vegetation using 16-day MODIS data at 250-m in the Hyrcanian deciduous forests and semi-steppe rangelands of northeastern Iran over the 17 years. Also, two vegetation greenness (EVI and NDVI) and one vegetation water content (NDWI) indices were used to finding real responses of the forests and rangelands to the drought conditions. We applied the bivariate indicator spatial association to examine possible relationships among precipitation and 16-day vegetation anomalies at both regional (*Moran's I*) and local (BiLISA) scales. The inter-seasonal SPI values showed that northeastern Iran experienced moderate to extreme drought conditions in 2001, 2008, 2011 and 2014, and normal conditions in 2002-2005, 2009 and 2012 during the growing season. Overall, all of the three VIs showed positive responses to the inter-seasonal precipitation anomalies for both forests and rangelands throughout the 17 years. Although vegetation anomalies recorded higher correlation coefficients with inter-seasonal precipitation anomalies, based on the NDVI (forests) and NDWI (rangelands), there were no significant differences between the mean correlation coefficients of the three vegetation indices. Monthly droughts disturbed the greenness and water content properties of forests during the middle of the growing season of drought conditions, while they had significant impacts on the water content of rangelands in comparison to their greenness throughout DOYs. The vegetation stress showed higher relationships with inter-seasonal precipitation deficit than monthly precipitation deficit conditions. BiLISA cluster maps reveal that about one-fifth of vegetation with the high-stress condition was experienced high-drought condition during a half or higher length of the growing season. BiLISA outliers indicate

that there are some locations with stress-affected vegetation surrounded by low droughts (Low-high) and vice versa (High-low), which suggest further research regarding other natural disturbances and the sensitivity of tree species. The variation of forest responses to drought conditions expresses that precipitation deficit is not a certain climatic variable determining the real physiological condition of the Hyrcanian deciduous forests. Therefore, it is essential to explore forest droughts from biological and climatic aspects as well as consider the long-term impacts of other climatic variables and hydrological droughts on their disturbances.

## Acknowledgements

This paper is a part of the first author's doctoral studies under the supervision of the third author. Massive thanks to the anonymous reviewers and the editorial comments, which helped us to improve this manuscript.



---

## **Forest Drought-Induced Diversity of Hyrcanian Individual-Tree Mortality Affected by Meteorological and Hydrological Droughts by Analyzing Moderate Resolution Imaging Spectroradiometer Products and Spatial Autoregressive Models over Northeast Iran**

Omid Abdi, Zeinab Shirvani, Manfred F. Buchroithner

### Author contributions:

Omid Abdi designed the work and implemented drought hazards modelling, time-series image analysis, tree mortality measurements, autoregressive-statistical analysis, and writing the article.

Zeinab Shirvani contributed to creating the database of tree mortality and data analysis.

Manfred F. Buchroithner reviewed the article and supervised at all stages of the study.

### Citation:

Abdi, O.; Shirvani, Z.; Buchroithner, M.F. Forest drought-induced diversity of Hyrcanian individual-tree mortality affected by meteorological and hydrological droughts by analyzing moderate resolution imaging spectroradiometer products and spatial autoregressive models over northeast Iran. *Agricultural and Forest Meteorology* **2019**, *275*, 265–276, doi:10.1016/j.agrformet.2019.05.029.

## 4.1 Abstract

This study sought to assess the spatial variations of physiological responses of Hyrcanian forests to the hazard intensity of meteorological and hydrological droughts for properly assessing drought-induced tree mortality in northeastern Iran. A variety of time series moderate resolution imaging spectroradiometer (MODIS) products and ground-based measurements were applied to derive the multiple dimensions of droughts and forest stresses. Drought hazard intensity was computed with the combination of the severity, frequency and duration of drought dimensions for each variable. The intensity of tree mortality was calculated by Simpson's diversity index with surveying 30,000 individuals of commercial species suspected to dieback within 100 intact parcels. Spatial autoregressive models were carried out to determine significant meteorological and hydrological drivers that controlling biological responses of forests to drought events and associations of the diversity of tree mortality with these forest responses. Results showed that the hazard intensity of forest water-content-deficit and greenness loss showed higher relationships with the high land surface temperatures and actual evapotranspiration than the precipitation and surface water deficits, however, they did not show significant relationships with the groundwater deficit. Moreover, diversity of tree mortality was associated with forest water-content-deficit from moderate to death stages and with forest greenness loss in the only very high defoliation stage. The critical values of forest droughts and diversity of mortality were recorded for the climax tree species. Understanding satellite-derived physiological responses of forests to droughts might help to assess the intensity of tree mortality widely to adopt appropriate strategies for mitigating the impacts of droughts on the tree species.

## 4.2 Introduction

Forest dieback is a vital condition in which tree individuals or stands increasingly die from the crown to the root system, resulting in declining tree growth, loss of tree vitality, browning of leaves, and defoliating and dying of forest patches in large areas with negative consequences on the ecosystem [180]. Although diverse biotic and abiotic agents have been introduced as the causes of forest dieback [180,181], forest vulnerability to climatic shifts, such as severe droughts, high

temperatures and water stress, widely accepted as the primary causes of widespread dieback across the world [182–190]. However, climate-based droughts entirely cannot explain the responses of forest biomes to drought events, the actual drought-related physiological changes of forests are necessary to be quantified as well [24]. Thus, there is a need to determine reliable indicators indicating forest responses to meteorological and hydrological droughts, and drought-induced tree mortality particularly relying on the proper time-series remotely sensed observations.

A variety of vegetation indices have been derived from the reflectance spectra of MODIS images, including greenness-related vegetation indices such as the normalized difference vegetation index (NDVI) [28] and the enhanced vegetation index (EVI) [191], and also water content-related vegetation indices such as the normalized difference water index (NDWI) [29] and the land surface water index (LSWI) [192]. The NDWI is derived based on the absorption spectrum of water and the reflectance spectrum of spongy mesophyll (Near-infrared (NIR) and Short Wave Infrared (SWIR)), which are connected to the moisture of the vegetation canopy, therefore, are appropriate for monitoring water content-related forest drought. Whereas the NDVI is derived from the chlorophyll absorption and spongy mesophyll spectra (red and NIR), which are sensitive to the greenness and carbon sequestration of vegetation [44,66,193–195]. Moreover, satellite-derived products based on the thermal infrared spectra (TIR), such as the land surface temperature (LST) and the actual evapotranspiration (ETa) [196], have been used to diagnose evapotranspiration and soil moisture for retrieving drought stress [197–201] through relationships between the anomalies of satellite-derived vegetation indices and temperatures and evapotranspiration indices [24,202,203].

Although significant responses of forests to precipitation deficits have been addressed in different forest biomes [33,47,204–206], incorporating satellite-derived temperatures and evapotranspiration indices for the quantification of drought have been decreased the uncertainty of forest responses to meteorological droughts [24,34,39,202,203,207]. Increases temperatures and heat waves affect forest functioning by intensifying evaporation in the root system and canopy of trees and amplify dehydration and biotic activities which resulting in forest die-off and mortality [208,209] regardless of precipitation deficits [209]. The impacts of changing temperatures and evapotranspiration on dehydration and forest vulnerability to die-off are required to be evaluated

in characterizing forest droughts. Furthermore, increases forest water-use and changes in the species composition and forest structure since prolonged and severe droughts affect hydrological processes from the stand to regional levels [210]. Hydrological responses to forest drought either in streamflow level or groundwater level can be considered as an indication of drought-induced changing in the water balance of forests as well [210–212].

In addition, forest biomes have shown different responses to drought conditions. The resistance and resilience of tropical and boreal forests to drought conditions are well-documented in several studies [38,204,213,214]. Unlike the arid and humid biomes, species responses to water deficit may occur at long time-scales in the semiarid and sub-humid biomes [32–34]. However, tree die-off might be resulting from drought-induced carbon starvation in a specific species or hydraulic deterioration in another species within a forest biome [215], that is, a combination of tree mortality mechanisms need to be considered for analyzing species-dieback in a specific forest biome [40].

Multiple features of forest drought, namely frequency, duration, severity, onset and end time, and areal extent are resulting from these dimensions of water-, precipitation- and temperature-driven drought conditions [216,217], which lead to extreme tree mortality and alter the composition, structure, and biogeography of forests considerably[44,218–221] with higher impact on the dominant and large tree species [222]. A considerable amount of previous studies have addressed the frequency and severity of drought among all features for quantification and monitoring of drought. However, a total drought process contains detailed information of all its dimensions, such as the risk map of drought hazard intensity.

Satellite images have provided an efficient system for quantification, assessment and monitoring of drought dimensions and their impacts on trees' vigour and recovery, layers, functions, and ecosystem services from regional to global scales [12]. A long duration of drought increases forest vulnerability and causes carbon starvation and hydraulic deterioration of tree species [38–42], which appear as slow growth, declining greenness and biomass, forest die-off and tree mortality [43–48] as well as forest diseases and insect infestations [52]. Quantification and monitoring of drought-induced hydraulic deterioration and carbon starvation of tree species have been characterized through relationships between satellite-derived vegetation indices and in situ measurements of tree growth or aboveground

biomass [34,65–67]. Even though MODIS-derived vegetation indices have received the most attention for characterizing of forest responses to drought dimensions since their fine temporal resolution and usable values, to date, it is challenging to quantify drought-induced tree mortality through these satellite data due to their coarse spatial resolution. Conventional regression analyses [34,66] between MODIS-derived forest-drought indices and field-based indicators of forest growth and vitality are the most common approaches in quantifying drought-related tree mortality. Further statistical methods such as LASSO regression [69], Random Forest [70], timescales and time-lag effects [71,72] have been suggested for this purpose as well. However, these models focus only on statistical relationships and do not consider spatial relationships between variables, therefore, we need to explore alternative approaches which can model spatial-statistical associations between satellite-derived drought indices and severity of tree mortality such as the spatial error and spatial lag models [73].

The aforementioned works have focused mostly on quantification and monitoring droughts and tree mortality in the tropical and boreal forests. We little know about the vulnerability of temperate forests to drought events and drought-induced tree mortality, particularly in the Hyrcanian forests where a wide diversity of tree species exists and experienced several severe droughts during recent decades [206]. In this study, we seek to quantify the severity, duration, frequency and spatial extent of forest droughts (i.e., water-content deficit and greenness loss), meteorological droughts (decreases of precipitation and evapotranspiration, and increases of temperatures), and hydrological droughts (decreases of streamflow and groundwater levels) as the drought hazard intensity (DHI) indicator for each drought type in northeast Iran during 2000–2016. Then we examine spatial associations among the hazard intensity of forest droughts and the hazard intensity of meteorological and hydrological droughts. Finally, we explore the intensity of individual-tree mortality at different levels and examine its spatial relationship with the hazard intensity of forest droughts in northeast Iran. Specifically, this study was established to find appropriate responses to the following questions:

- Are the NDWI and NDVI strong enough to retrieve the biological responses of Hyrcanian forests to the meteorological and hydrological droughts?

- Which of the meteorological and hydrological variables have significantly affected the water-content and greenness properties of the Hyrcanian forests?
- Is there a significant spatial relationship between the diversity of tree mortality and the vulnerability of Hyrcanian forests to droughts?
- In which forest-drought conditions and dieback level the intensity of tree mortality is significant?

Our drought analyses are based on the time-series of three novel products of MODIS including MOD13Q1, MOD11A2, and MOD16A2 as well as ground-based measurements of precipitation and water levels. Tree mortality analysis is based on the field observations from diverse species of pristine forests falling into dieback levels. We use spatial autoregressive approaches to explore relationships between droughts and tree mortality events.

## 4.3 Overview of the Study Area

We concentrated our studies on the end parts of the Hyrcanian forests in northeastern Iran, southeast of the Caspian Sea in the Golestan Province (Figure 4.1a). Elevation ranges between 30 to 3360m from north to south of the region with an average of 1080 m. This area consists of humid (89.60%) and subhumid (10.40%) biomes (Figure 4.1d). Forested areas are mostly managed in the form of forest management plans (FMPs) for logging or scarcely as forest conservation plans in the protected areas such as Golestan National Park in the eastern parts of the study area. We selected a total of 1162 parcels for exploring the vulnerability of tree species to the drought conditions, which 100 parcels were randomly selected for the sampling of tree mortality events (Figure 4.1d and c). Dominant tree species are *Fagus orientalis*-*Carpinus betulus* and *Juniperus polycarpus* in the western zone, *Quercus castaneifolia*-*Carpinus betulus* and *Carpinus betulus* in the middle zone, and *Quercus castaneifolia*-*Carpinus betulus* and *Carpinus betulus*-*Pterocarya fraxinifolia* in the eastern zone of the study area (Figure 4.1b).

## 4.4 Data and Methodology

### 4.4.1 Meteorological and hydrological anomalies

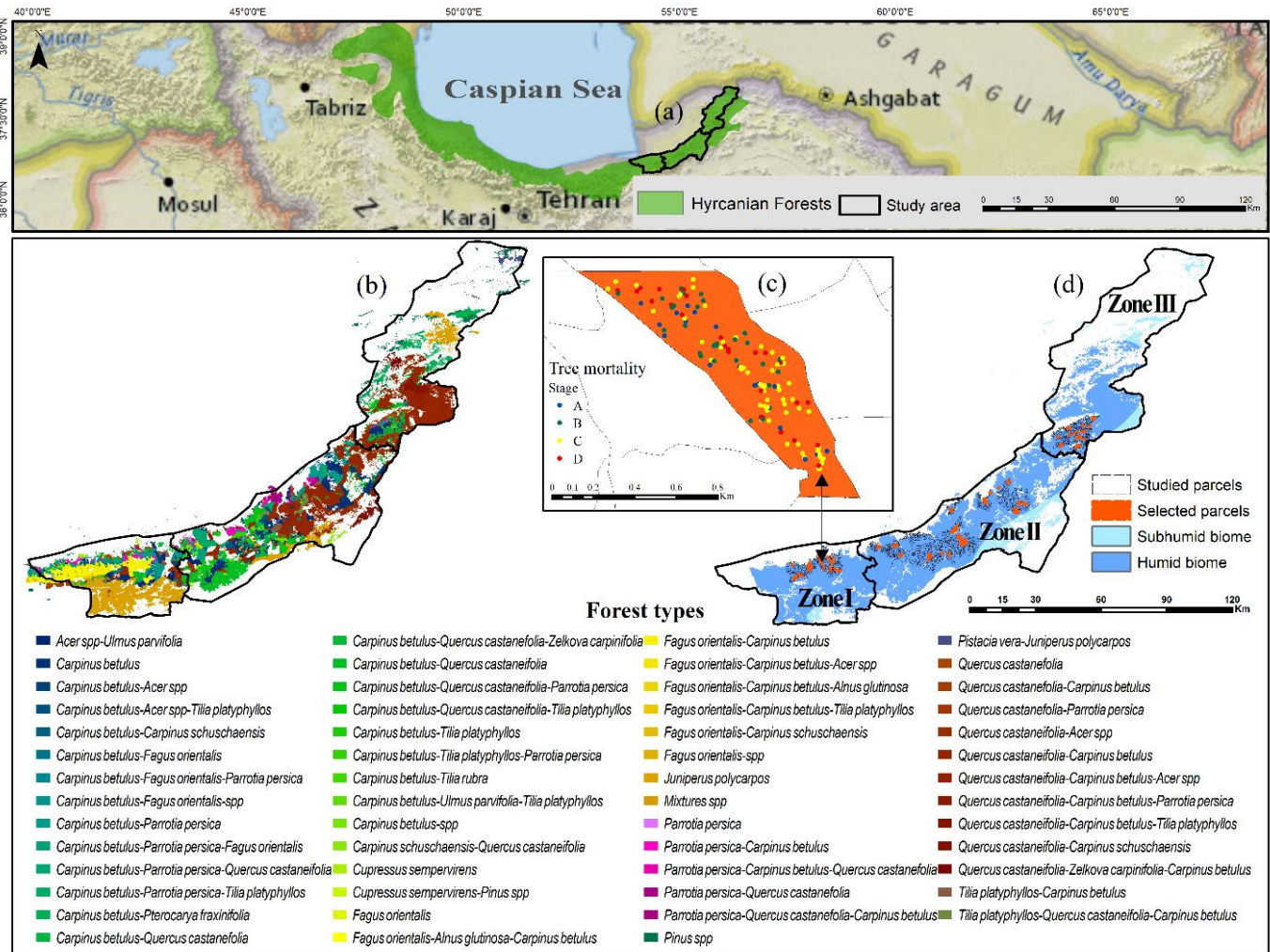


**Figure 4.1** Spatial location of the study area in the Hyrcanian forests (a), tree species types (b), an example of scattering of tree species dieback-samples in one parcel out of 100 selected parcels (c), and distribution the total studied parcels (1162) for exploring the stress of the forest types and the selected parcels (100) for the sampling of tree mortality, and the forest biomes in northeastern Iran (d).

To explore how the variations of climate and hydrological drivers control forest growth and forest water-content, we assessed long-term anomalies of monthly precipitation, day/night LST and ETa, and also the anomalies of surface water and groundwater levels. Time-series precipitation (1987–2016), groundwater (1985–2016) and surface water (2000–2014) data were obtained from 24 to 94 rain gauge stations, 34 to 52 streamflow gauging stations and 150 to 260 piezometric wells. Ordinary Kriging and Empirical Bayesian Kriging [223] were carried out to interpolate monthly precipitation, groundwater and surface water values from the measured points to the surface of the study region. We calculated the monthly precipitation anomalies using the Standardized Precipitation Index (SPI) [224]; the monthly surface-water anomalies using the Streamflow Drought Index (SDI) [225] and; the monthly groundwater anomalies

using the Surface Water Index (SWI) [226] for a specific month ( $j$ ) of a specific year ( $k$ ) at a specific cell ( $i$ ). To obtain the SPI, SDI and SWI, we calculated Z-scores (Equation 4.1).

$$Zm_{jki} = \frac{X_{jki} - \mu_{ji}}{\sigma_{ji}}, \quad (4.1)$$

where  $X_{jki}$  represents the value of a variable (i.e., precipitation, surface water and groundwater levels) in the  $j$ th month,  $\mu_{ji}$  is the long-term mean and  $\sigma_{ji}$  is the standard deviation of the variable for the  $j$ th month at  $i$ th cell. To assess LST anomalies, a total of 776 8-day images of Terra MODIS Land Surface Temperature and Emissivity L3 1 km product (MOD11A2) from 2000 to 2016 were obtained from the online Data Pool of the NASA Land Processes Distributed Active Archive Center (LP DAAC), USGS/EROS, ([https://lpdaac.usgs.gov/data\\_access/data\\_pool](https://lpdaac.usgs.gov/data_access/data_pool)). MOD11A2 contains the daytime and nighttime surface temperature data and their quality condition (QC) [227]. The monthly median of 8-day images were calculated to improve their stability and were reduced to 202 images. The daytime and the nighttime LST anomalies (SDLST and SNLST) were calculated using Z-scores (Equation 4.1), which  $X_{jki}$  equals the LST value of the  $j$ th month of the  $k$ th year,  $\mu_{ji}$  and  $\sigma_{ji}$  represent the average and standard deviation of the 17-year LST for the  $j$ th month at  $i$ th cell. In addition, to assess ETa anomalies, we obtained 168 monthly actual evapotranspiration (ETa) images derived from the MODIS data using the Simplified Surface Energy Balance (SSEBop) model [200] from 2003 to 2016 from <https://earlywarning.usgs.gov/fews> from 2003 to 2016. The ETa anomalies (SETa) were obtained using Z-scores (Equation 4.1) as well, which  $X_{jki}$  represents the ETa value of the  $j$ th month of the  $k$ th year,  $\mu_{ji}$  and  $\sigma_{ji}$  represent the average and standard deviation of the 14-year ETa values at  $i$ th cell.

The annual anomalies of meteorological and hydrological drivers were calculated from the median of anomalies of the months within each hydrological year (from October of the previous year to September of the current year) or growing season (March–October) at each cell. The anomaly values of meteorological and hydrological drought-indices were classified based on the first standard deviation from extreme wet to extreme drought conditions (Table 4.S1).

#### 4.4.2 Forest anomalies

To explore biological responses of forests to meteorological and hydrological droughts, we derived two vegetation indices including NDWI and NDVI from MODIS products for retrieving



forest water content and forest greenness anomalies. Hence, we obtained 16-day time-series of 389 images of Terra MODIS VI c5 product (MOD13Q1) with a 250m resolution through LP DAAC from 2000 to 2016. The NDWI and NDVI were derived from Red (0.6-0.7  $\mu\text{m}$ , band 1), NIR (0.7–1.1  $\mu\text{m}$ , band 2) and SWIR (2.105–2.155  $\mu\text{m}$ , band 7) as Equation 4.2 [29] and 4.3 [28].

$$NDWI = \frac{\rho_{NIR} - \rho_{SWIR}}{\rho_{NIR} + \rho_{SWIR}} \quad (4.2)$$

$$NDVI = \frac{\rho_{NIR} - \rho_{red}}{\rho_{NIR} + \rho_{red}} \quad (4.3)$$

Then, we derived 16-day NDWI and NDVI anomalies (SNDWI and SNDVI) based on the z-score formula (Equation 4.1), which  $X_{jki}$  represents the NDWI/NDVI value of the  $j$ th 16-day of the  $k$ th year,  $\mu_{ji}$  and  $\sigma_{ji}$  represent the average and standard deviation of the 17-year NDWI/NDVI values at  $i$ th cell.

The seasonal anomalies of the NDWI and NDVI were calculated from the median of anomalies of the 16 days within each growing season at each cell. The anomalies of the NDWI and NDVI were classified to the five vegetation condition schemes (Table 4.S1) based on the first standard deviation method [228] as well.

#### 4.4.3 Features of droughts

Different dimensions of droughts were derived from the anomalies' indices, which include severity, frequency, duration, onset and end time, and spatial extent of droughts [25,26]. Severity was defined as the scores of the indices below the normal condition, which escalates from low values to the high values. Frequency and duration were accounted as the number of recurrences and consecutive recurrences of drought within a year. The onset and end time of drought were determined from the threshold values of the indices within a year.

We used these features to create drought hazard intensity (DHI), as an indication that aggregated different dimensions of drought in a specific place within a year.

#### 4.4.4 Drought hazard intensity

Drought hazard intensity was computed based on the severity ( $S$ ) and the probability of drought occurrence derived from the frequency ( $F$ ) and duration ( $D$ ) of meteorological, hydrological and forest droughts within each year and cell. The values of the dimensions of

drought events were standardized through the fuzzy membership functions [229]; Fuzzy Linear for the severity and Fuzzy Large for the frequency and duration values. Fuzzy Gamma operation was used to combine the fuzzified values of the drought dimensions ( $\mu_i$ ) to derive the yearly drought hazard intensity for each driver within a specific cell ( $DHI_k$ ) (Equation 4.4).

$$DHI_k = (1 - \prod_{i=1}^n (1 - \mu_i))^\gamma \times (\prod_{i=1}^n \mu_i)^{1-\gamma} \quad (4.4)$$

The final hazard intensity of a cell associated with a specific drought was calculated from the median yearly DHI values of that driver within the study period. Output values of DHI ranging between 0 and 1, the values near to 1 are indicating higher drought hazard intensity and vice versa.

#### 4.4.5 Surveying of individual-tree mortality

We selected randomly 100 parcels from 19 FMPs, which were less affected by human activities and remained intact. We surveyed all tree species showing a physical symptom of diebacks such as canopy thinning, defoliation, crown dieback, foliage and bark discolouration, epicormic growth, and die-off [43,180] within a parcel. A total of 29,937 individuals were explored from 15 commercial tree species, which 14,222 of trees showed at least one symptom of dieback. We recorded the attributes of the trees including the diameter at breast height ( $\approx 1.30$  m) of all individuals above 12 cm, tree species, dieback symptoms, and spatial location (X, Y). All dieback-suspected individuals were classified based on the intensity of dieback into four categories: Stage A; dieback  $\leq 25\%$  (canopy thinning, low defoliation), Stage B;  $25 < \text{dieback} \leq 50\%$  (medium to high crown defoliation), Stage C;  $50 < \text{dieback} \leq 75\%$  (epicormic growth, insect and fungal infestations), and Stage D; dieback  $> 75\%$  (high dieback and dead trees). Roughly 44% and 20% of the samples were classified in Stages D and A, and the remaining samples were distributed equally within Stages B and C.

#### 4.4.6 Diversity index of individual-tree mortality

To quantify the intensity of tree mortality, we calculated the diversity of individual-tree species affected by dieback within a parcel using Simpson's Diversity Index (D) [230], shown in Equation 4.5:

$$D = 1 - \sum_{i=1}^s \left( \frac{ba_i}{ba} \right)^2 \quad (4.5)$$

where  $ba_i$  is the basal area of individuals of the species  $i$  affected by dieback within a given parcel,  $ba$  is the total basal areas of trees, and  $s$  is the number of tree species within the given parcel. The

values of  $D$  range from 0 (no diversity) to 1 (infinite diversity) and represent the probability that two individuals randomly selected from a location belong to different species [231].

Moran's  $I$  [232] was used to examine whether spatial relationships happen in shaping the patterns of diversity of tree mortality over the studied zones within each dieback stage.

#### 4.4.7 Spatial autoregressive between drought hazards and diversity of individual-tree mortality

Spatial autoregressive approaches include the spatial lag (SL) and spatial error (SE) models were used to determine significant meteorological and hydrological drivers that control the biological responses of forests to drought events. We employed the DHI indicators for spatial-statistical analyses among the variables. Conventional regression models such as the ordinary least square (OLS), estimate a linear dependence between dependent and explanatory variables and assume errors show a normal distribution. The existence of spatial autocorrelation of a model is indicating a significant correlation among error terms of observations and reinforces the coefficients of the model [233]. The SL model includes a spatially lagged dependent variable ( $\omega\gamma$ ), the coefficients of the explanatory variables ( $\beta$ ), and the error term ( $\varepsilon$ ) as Equation 4.6. In the SE model (Equation 4.7), the error term ( $\varepsilon$ ) decomposes to the spatial lag of the errors with an autoregressive coefficient ( $\lambda$ ) and a “well-behaved” error ( $\epsilon$ ) with a normal distribution [73]. Furthermore, these models were used to examine how the diversity of tree mortality associated with the biological responses of forests to droughts. Specifically, we analysed the spatial intensity of tree mortality associated with the DHI-related water content deficit and greenness loss of forests in each step of dieback.

$$y = \rho\omega\gamma + X\beta + \varepsilon \quad (4.6)$$

$$y = X\beta + \varepsilon \quad (\varepsilon = \lambda\omega + \epsilon) \quad (4.7)$$

Existing spatial autocorrelation in the spatial autoregressive approaches was tested using the parameters of Moran's  $I$  and Lagrange Multiplier [233,234] at an alpha level of 0.05. The goodness-of-fit of the regression models was measured using R-squared, Log-likelihood (LI), Akaike Info Criterion (AIC), and Schwarz Criterion (SC) [73]. The superior model was selected depending upon the highest values of R-squared and LI, and the lowest values of AIC and SC.

## 4.5 Results

### 4.5.1 Drought dimensions

#### 4.5.1.1 Meteorological drought

The median of precipitation anomalies indicated that about 25.6% of the forests experienced severe droughts, which about 64% of the area recorded more than six months drought condition and about 65% of the area have experienced three consecutive months of droughts during a hydrological year (Figure 4.S1–S3). Moreover, the LST anomalies show critical values for both day-time LST (59.3%) and night-time LST (45.9%) with a frequency of more than four months in 66.5 and 62.9% of the forests and three consecutive months of drought events in 59.3 and 45.9% of the forest during a seasonal growth (Figure 4.S1–S3). Likewise, about 65.6% of the forests experienced severe ETa anomalies, which about 66.8% of the area recorded more than four months of the negative condition and about 60.8% of the forests experienced three consecutive months of the negative condition during a seasonal growth (Figure 4.S1–S3).

#### 4.5.1.2 Hydrological drought

Although the median of severe surface water droughts was recorded in the few areas (18.21%), about 44.26% of the forests experienced a frequency of more than six months with the longer consecutive months of drought condition including five (35.9%) and six (32.6%) months during a hydrological year (Figure 4.S1–S3). The severe condition of groundwater drought obtained in 17.31% of the forests with a lower frequency of more than six months (10.7%) and shorter duration in a hydrological year (Figure 4.S1–S3).

#### 4.5.1.3 Forest drought

The medians of the anomalies of vegetation indices indicated that about 57.4 and 51.5% of the forests affected by the severe deficit of water content and the loss of greenness during a growing season (Figure 4.S1). The frequency of more than eight DOYs of the negative NDWI and NDVI was recorded in 61.5 and 35.3% of the forests (Figure 4.S2), and the duration of the four DOYs of the negative condition was observed in 38.1 and 31.3% of the area (Figure 4.S3), respectively.

#### 4.5.2 Spatial variations of drought hazard intensity (DHI)

The average hazard intensity of meteorological droughts was higher than hydrological droughts in the study area. Among the meteorological drivers, the higher average values of the DHI recorded for the ETa (0.48), day-time LST (0.36), night-time LST (0.31), and precipitation (0.27), respectively. The mean values of surface water (0.23) was higher than the groundwater (0.18). Critical values of hazard intensity of the meteorological droughts are distributed in the western and the eastern zones (Figure 4.2a–d), while the higher values of the hydrological droughts are recorded in the eastern zone of the study area (Figure 4.2e and f). The obtained hazard intensity values for forest droughts are greater than meteorological and hydrological droughts. The average values of the DHI for the deficit of forest water-content (0.48) was greater than the values of the loss of forest greenness (0.41), with higher intensity in the western and middle zones (Figure 4.2g and h).

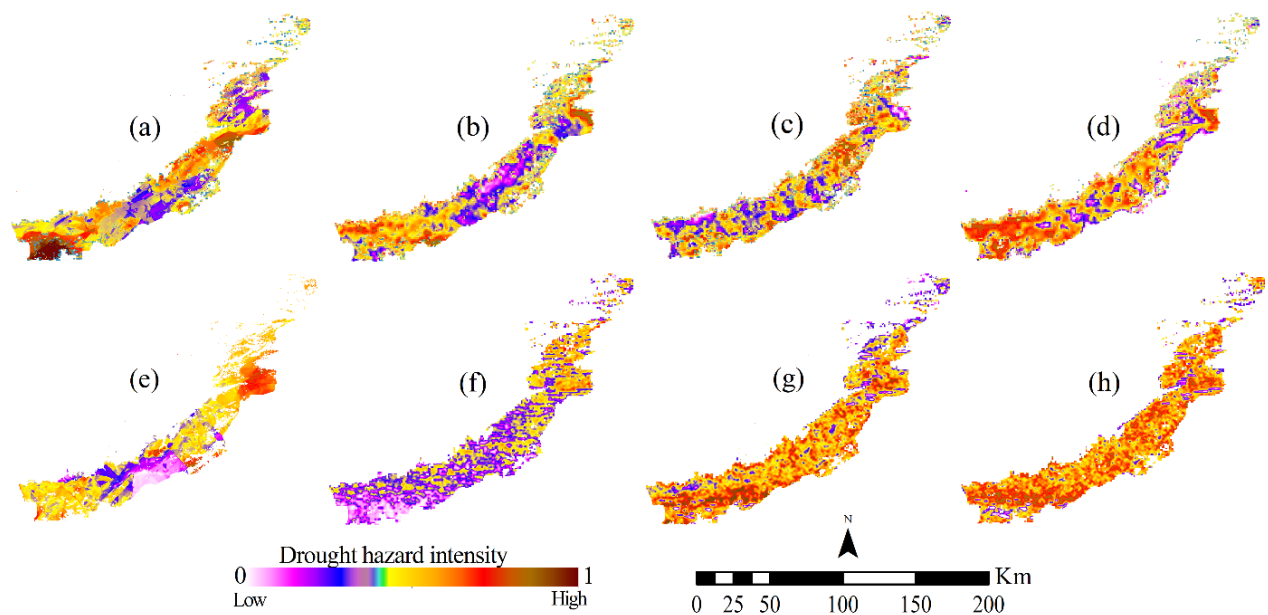


**Figure 4.2** Drought hazard intensity is a combination of the severity, frequency and duration of drought events for each year. The median values of the periods are used as the final hazard intensity of the meteorological droughts: the precipitation (a), day-time land surface temperature (b), night-time land surface temperature (c) and actual evapotranspiration (d); hydrological droughts: the surface water (e) and groundwater (f) levels; forest droughts: the deficit of forest water-content (g) and loss of forest greenness (h) in northeastern Iran. Although the average values of the hazard intensity of meteorological droughts are greater than the hydrological droughts, the hazard intensity values of forest droughts are considerable throughout the study area.

#### 4.5.3 Diversity of individual-tree mortality

The spatial variability of the diversity of tree species mortality showed significant spatial autocorrelation of Simpson's diversity values in all four species dieback stages. The higher values of diversity of species mortality were obtained in the stage C by  $0.587 \pm 0.035$  (95% CI, Moran's  $I = 0.293$  and  $P < 0.05$ ), stage B by  $0.567 \pm 0.041$  (95% CI, Moran's  $I = 0.487$  and  $P < 0.01$ ), stage D by  $0.493 \pm 0.035$  (95% CI, Moran's  $I = 0.390$  and  $P < 0.01$ ), and stage A by  $0.419 \pm 0.039$  (95% CI, Moran's  $I = 0.283$  and  $P < 0.05$ ), respectively. The spatial variations of local statistics of Simpson's index described that the diversity of species mortality in the central and eastern parcels (Figure 4.3b and c) is higher than the western parcels (Figure 4.3a).

The total basal area of the tree species affected by dieback was obtained about  $0.5089 \text{ m}^2.\text{ha}^{-1}$  in four stages. Although Stage B and Stage C recorded a higher diversity of tree mortality, the higher basal area was observed in Stage D by  $0.1463 \text{ m}^2.\text{ha}^{-1}$  and Stage A by  $0.1426 \text{ m}^2.\text{ha}^{-1}$ . On the other hand, the domination of the basal area of a few species such as *Carpinus betulus* (Stage A and D), *Parrotia persica* (Stage D) and *Quercus castanefolia* (Stage A) caused a lower diversity of species-dieback in Stage D and A by comparison with Stage C and B. To compare to the western zones (Figure 4.3a), the parcels of the central and the eastern zones recorded a higher diversity of tree mortality (Figure 4.3b and c).

#### 4.5.4 Spatial dependence between the hazard intensity of forest droughts with meteorological and hydrological droughts

The indicators of regression diagnostics show evidence of having spatial dependence in the SL and SE models (Table 4.S2). Highly significant scores of Moran's  $I$  with 0.53 and 0.38, as well as significant Robust LM ( $P < 0.01$ ), are indicating strong spatial autocorrelation of residuals' of the forest drought hazard intensity based on the NDWI and NDVI. The indicators of goodness-of-fit show higher performance of the SE model than the SL and OLS models (Table 4.1). The R-squared values are 0.35 and 0.26, and the LL values are 5521 and 7040 in the SE model for the  $\text{NDWI}_{\text{DHI}}$  and  $\text{NDVI}_{\text{DHI}}$ , respectively.

The SE parameters show that there is a significant spatial dependence between the hazard intensity of forest droughts and meteorological droughts. The hazard intensity of the deficit of



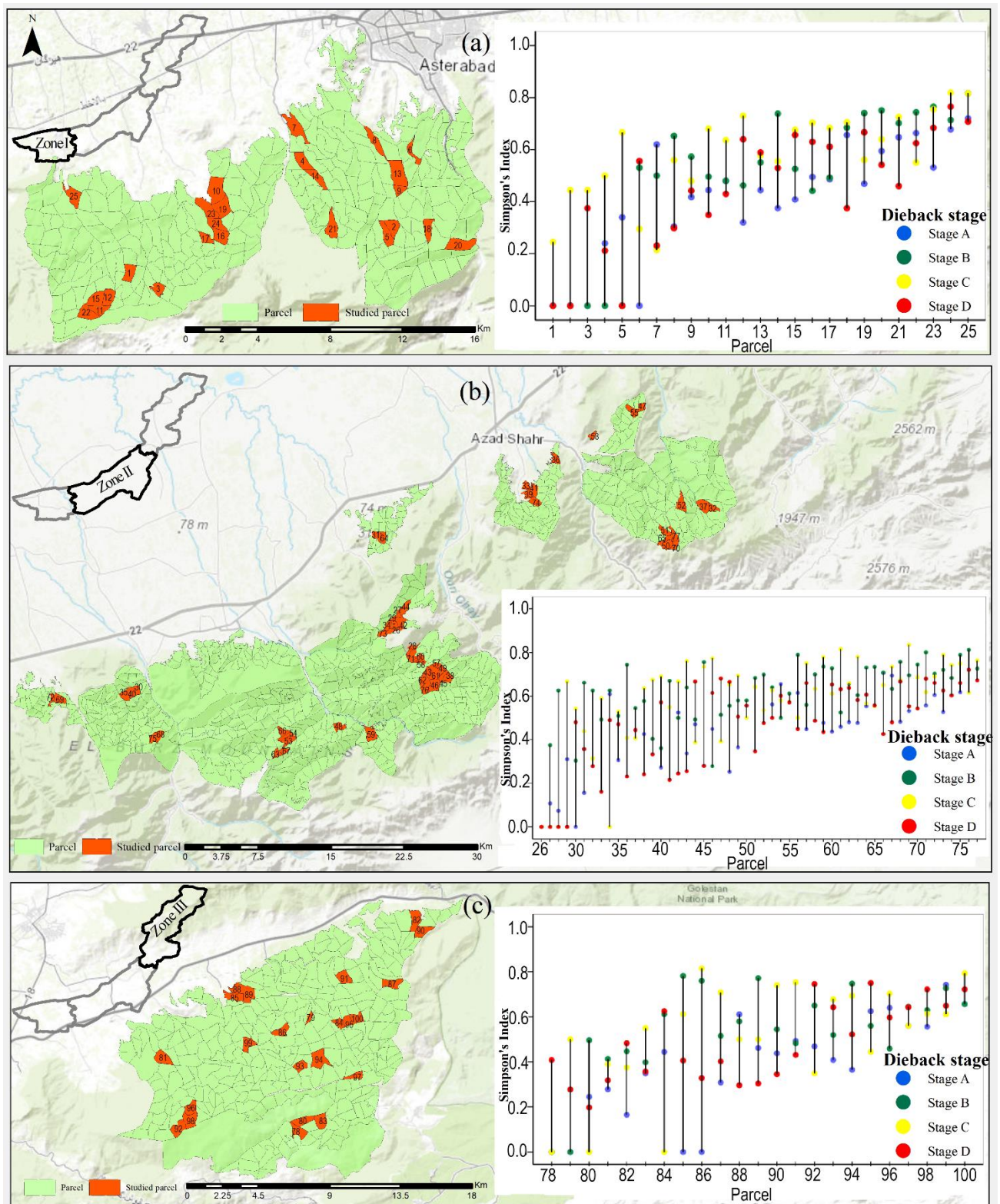


**Figure 4.3** Spatial distribution of diversity of the tree species diebacks measured using Simpson's diversity index for the four dieback stages in the studied parcels of three zones in northeastern Iran.

forest water-content showed significant coefficients with the DHI values of the night-time LST (0.259), ETa (0.2143) and day-time LST (0.1803) ( $P < 0.01$ ), as well as the precipitation (0.0359) ( $P < 0.05$ ), respectively. Likewise, the spatial coefficients of drought hazard intensity between the

loss of forest greenness and the night-time LST (0.1991), ETa (0.1550) and day-time LST (0.1426) are significant (Table 4.1). Although the hazard intensity of forest droughts showed significant spatial dependence with the hazard intensity of the surface water drought ( $P < 0.05$ ), they did not show significant relationships with the groundwater drought ( $P > 0.05$ ) (Table 4.1).

**Table 4.1** The model coefficients and the parameters of model fit resulting from the spatial relationships between the hazard intensity of forest droughts, based on water-content (NDWI) and greenness (NDVI) properties, with the hazard intensity of the meteorological (precipitation, day-time LST, night-time LST and actual evapotranspiration) and hydrological (surface water and groundwater levels) droughts in northeastern Iran.

Type of drought		NDWI <sub>DHI</sub>			NDVI <sub>DHI</sub>		
Model		OLS	SL	SE	OLS	SL	SE
Intercept		0.5050**	0.1316**	0.4916**	0.3750**	0.1759**	0.3762**
Precipitation		-0.0235 <sup>ns</sup>	-0.0015 <sup>ns</sup>	0.0359*	0.0368**	0.0270**	0.0385**
Day-time LST		0.1710**	0.1507**	0.18031**	0.1545**	0.1328**	0.1426**
Night-time LST		0.2448**	0.2300**	0.2590**	0.1933**	0.1839**	0.1991**
Actual evapotranspiration		0.2690**	0.2068**	0.2143**	0.1674**	0.1466**	0.1550**
Groundwater level		-0.019 <sup>ns</sup>	0.0021 <sup>ns</sup>	-0.006 <sup>ns</sup>	-0.0348**	-0.016 <sup>ns</sup>	-0.015 <sup>ns</sup>
Surface water level		-0.0057 <sup>ns</sup>	-0.008 <sup>ns</sup>	0.0230*	0.0164*	0.0155*	0.0204*
$\rho_{wy}$		-	0.5427*	-	-	0.3871**	-
Lambda ( $\lambda_{wv}$ )		-	-	0.6035**	-	-	0.4389**
Model fit	R-squared	0.1572	0.3273	0.3507	0.1704	0.2474	0.2596
	Sigma-square	0.0120	0.0095	0.0092	0.0065	0.0059	0.0058
	Log likelihood	4900.95	5452.9	5521.26	6778.14	7010.62	7039.6
	Akaike info criterion	-9787.9	-10889.8	-11028.5	-13542.3	-14005.2	-14065.2

Note: \* p-value < 0.05, \*\* p-value < 0.01, and ns: not significant. LST: land surface temperature; NDWI: normalized difference water index; NDVI: normalized difference vegetation index; DHI: drought hazard intensity; OLS: ordinary least squares; SL: spatial lag; SE: spatial error.

#### 4.5.5 Spatial dependence between the diversity of individual-tree mortality and forest droughts

The parameters of spatial models represent that the diversity of the four stages of tree species mortality show different responses to the forest droughts based on the deficit of water content and loss of greenness (Table 4.2). There was no significant spatial dependence between the diversity of individual-tree mortality and the hazard intensity of forest droughts in the first stage of dieback ( $p > 0.05$ ). We observed significant positive relationships between the diversity of tree mortality and the hazard intensity of the deficit of forest water content in Stage B, Stage C and Stage D. Though we observed strong positive associations between the diversity of tree species



mortality and the hazard intensity of the loss of forest greenness in Stage C, there were no significant relationships in Stage B and Stage D ( $p > 0.05$ ).

**Table 4.2** The model coefficients and the parameters of model fit resulting from the spatial relationships between the diversity of tree species mortality and the hazard intensity of forest droughts retrieved from the NDWI and the NDVI within four stages of diebacks in northeastern Iran.

Tree species dieback		Stage A			Stage B			Stage C			Stage D		
Model		OLS	SL	SE	OLS	SL	SE	OLS	SL	SE	OLS	SL	SE
Intercept		0.6365*	0.581*	0.589*	0.688*	0.658*	0.687*	0.319	0.295	0.345*	0.558*	0.455*	0.426*
NDWI <sub>DHI</sub>		0.0286 <sup>ns</sup>	-0.03 <sup>ns</sup>	-0.020 <sup>ns</sup>	0.4107*	0.335*	0.2980*	0.106 <sup>ns</sup>	0.081 <sup>ns</sup>	0.086*	0.135 <sup>ns</sup>	0.104*	0.245*
NDVI <sub>DHI</sub>		-0.431 <sup>s</sup>	-0.347 <sup>ns</sup>	-0.290 <sup>ns</sup>	-0.744*	-0.674*	-0.600*	0.349 <sup>ns</sup>	0.347 <sup>ns</sup>	0.326*	-0.291 <sup>ns</sup>	-0.227 <sup>ns</sup>	-0.220 <sup>ns</sup>
pwy		-	0.145*	-	-	0.102 <sup>ns</sup>	-	-	0.092 <sup>ns</sup>	-	-	0.224*	-
Lambda ( $\lambda_{wv}$ )		-		0.177*	-	-	0.221*	-	-	0.264*	-	-	0.384*
Model fit	R-squared	0.0251	0.069	0.063	0.058	0.086	0.119	0.037	0.065	0.134	0.010	0.155	0.2225
	Sigma-square	0.0404	0.037	0.0377	0.0384	0.0361	0.0348	0.032	0.030	0.028	0.032	0.026	0.0246
	Log likelihood	19.965	21.77	21.237	22.589	23.843	24.820	31.59	32.86	35.21	31.21	37.94	39.570
	Akaike info criterion	-33.930	-35.54	-36.47	-39.18	-39.69	-43.64	-57.18	-57.72	-64.43	-56.43	-67.87	-73.14

Note: \* p-value < 0.05, \*\* p-value < 0.01, and ns: not significant. NDWI: normalized difference water index; NDVI: normalized difference vegetation index; DHI: drought hazard intensity; OLS: ordinary least squares; SL: spatial lag; SE: spatial error.

The spatial regression models show significant indications of spatial dependence diagnostics in the three stages of species dieback. The SE model shows higher performance than the SL and OLS models (Table 4.2). The coefficients of NDWI<sub>DHI</sub>, based on the SE model, are about 0.298, 0.087 and 0.246 in the three critical stages (B, C and D), respectively. The coefficient of NDVI<sub>DHI</sub> is approximately 0.326 in Stage C based on the SE model as well.

## 4.6 Discussion

To obtain an appropriate indicator to assess the intensity of drought hazard, we derived multiple features of meteorological, hydrological and forest drivers from the MODIS products as well as in situ measurements. The drought hazard intensity indicator is a combination of the severity, frequency and duration of the drought events, which determines the degree of vulnerability of each pixel to the long-term meteorological, hydrological and forest droughts (Figure 4.2). The relationships between the hazard intensity of forest droughts and the hazard intensity of

meteorological and hydrological droughts were investigated using the spatial autoregressive approaches.

This research reveals that Hyrcanian broadleaf forests suffer from the high intensity of declining water content ( $NDWI_{DHI}$ ) and browning of greenness ( $NDVI_{DHI}$ ) (Figure 4.2g and h). Spatial error model depicts that the high intensity of Hyrcanian forest droughts is resulting from the high DHI values of the day/night-time land surface temperature and actual evapotranspiration (Table 4.1). Likewise, the significant responses of forested areas to drought conditions were reported by analyzing relationships between the NDVI and some indicators of meteorological droughts such as the SPEI [34] and MSPE [24] at global and regional scales. Our findings add that drought hazard intensity of Hyrcanian forests is more correlated to the meteorological drivers, with higher impacts on the deficit of forest water content in comparison with the loss of forest greenness (Table 4.1).

Although the hazard intensity of precipitation-deficit was significant throughout the region, its values were less than the hazard intensity of the ETa and the LST (Figure 4.2a–d). Some previous studies have represented that increases in the LST and ETa values are the primary causes of exceptional forest droughts even in the condition of prolonged normal precipitation [197,201]. Moreover, high positive coefficients of the land surface temperature and evapotranspiration in relation to the forest drought metrics are representing the importance of both physiological and meteorological aspects for quantification of the responses of Hyrcanian forests to drought events [24]. High temperatures of the canopy, declining forest greenness and water content due to drought have been highlighted by several scholars in Amazonian forests as well [47,202,203]. Luce et al. [41] reported the impacts of prolonged warming- and precipitation deficit-related on the increase of the risk of hydraulic deterioration of trees and reduction in the carbon balance and tree growth. Higher temperatures and drier conditions affect the soil moisture, which resulted in increasing tree respiration and heat-related individual-tree mortality.

The long-term meteorological droughts have affected the level of surface water and groundwater in the Hyrcanian forests as well. Hyrcanian forest showed positive responses to the hazard intensity of the deficit of surface water in northeastern Iran (Table 4.1). This severe condition has appeared as the declining groundwater level and soil moisture throughout the study area. For example, water-table has decreased about 9.25 cm per annum since the establishment of the network in 1973, where the higher cumulative declines were recorded for severe drought

conditions by 4.22, 4.79, 4.73 and 4.27 m during 2001, 2008, 2011 and 2014, respectively (Figure 4.4). Although Hyrcanian forest did not show a significant relationship with the drought hazard intensity of groundwater level, the rapid speed of declining water-table elevation of groundwater networks is considered as a big threaten for disturbing of Hyrcanian forests in the future. Furthermore, recent droughts have instigated farmers to change the agricultural system from dry-farming into irrigated farming, which uses the maximum of renewable reservoirs of the groundwater and surface water resources in this region. The responses of trees to the depletion of groundwater, surface water, and soil moisture are closing the stomata, reducing evapotranspiration and photosynthesis operations, which lead to morphological deficiencies including low growth-speed of tree components, forest dieback, and tree mortality [210–212].

The results of spatial error model describe that the diversity of tree species mortality showed a remarkable positive relationship with the hazard intensity of the deficit of forest water-content during the moderate (B), severe (C) and extreme (D) stages as well as with the loss of forest greenness during the severe stage (C) of forest dieback (Table 4.2). The critical deficit in forest water content affected by the precipitation deficit, heat stress, evapotranspiration stress, and surface water deficit (Table 4.1) has caused this significant diversity of tree mortality throughout the Hyrcanian region. Previous studies demonstrated that water stress was the leading cause of tree mortality rates in other forest biomes as well [187,189,220]. When the canopy is affected by thinning in the lower severity of dieback, the trees still have green foliage and affect by low stress of water-content, therefore, neither  $NDWI_{DHI}$  nor  $NDVI_{DHI}$  have shown significant relationships with the diversity of species diebacks in Stage A. In the moderate stage, the hydraulic function of trees is affected by droughts, although tree mortality diversity did not show significant spatial association with the  $NDVI_{DHI}$ , it showed a significant relationship with the  $NDWI_{DHI}$ . In the high stage, severe droughts have caused changes in the forest water-content as well as changes in forest canopy like severe foliage browning and defoliation [47,188,219], which is indicated by significant relationships with forest stresses retrieved from the  $NDWI$  and the  $NDVI$ . Dead trees showed a positive relationship only with the deficit of forest water content, which substantiates previous studies that have pointed to massive drought-induced tree mortality due to the declining of hydraulic operations and carbon sequestrations [43,45–48].

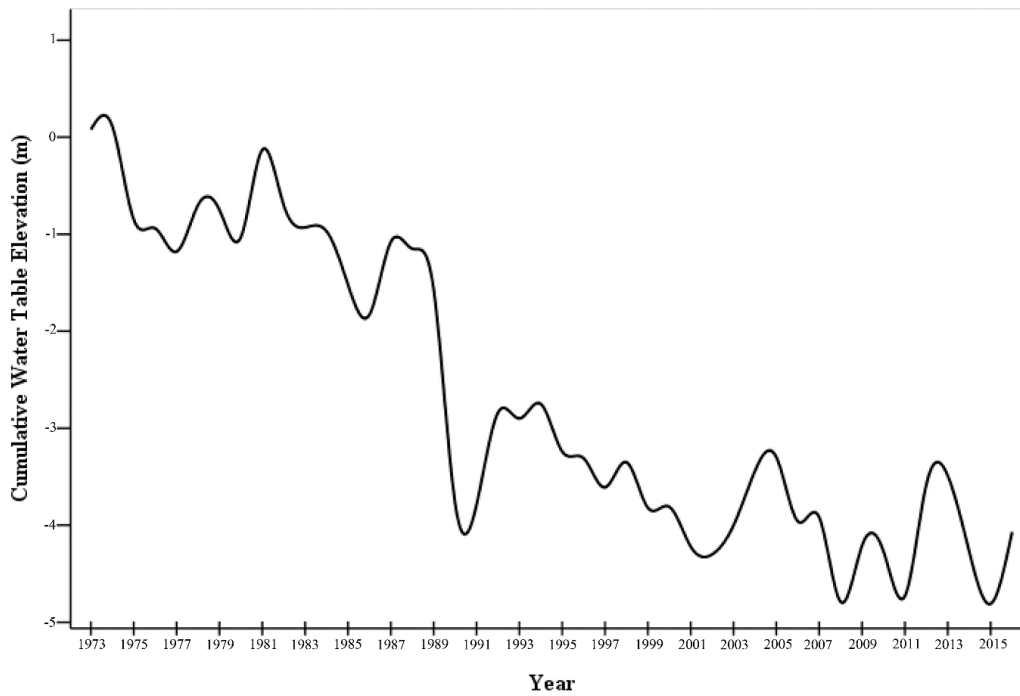


**Figure 4.4** Fluctuation in water-table elevation relative to establishing the date of assessment network in northeastern Iran from 1973 to 2016.

Our findings verify that the MODIS-derived NDWI shows higher performance than the MODIS-derived NDVI for quantification drought-induced individual-tree mortality in the Hyrcanian forests. Although Verbesselt et al. [69] found a higher performance of the NDVI than the NDII (as an index of water-content) for prediction of the diversity of tree mortality in southern New South Wales, Australia, Anderson et al. [213] reported the significant performances of both water content (NDWI) and greenness (EVI) indices in the estimation of tree mortality rates during the drought period of Amazonian tropical forests as well.

Our analyses concerning the sensitivity degrees of Hyrcanian forest types to drought hazard intensity, based on the  $NDVI_{DHI}$  and  $NDWI_{DHI}$ , indicating higher values for the climax species such as *Fagus orientalis*, *Quercus castanefolia* and *Carpinus betulus* throughout the 1162 studied parcels. The highest  $NDWI_{DHI}$  and  $NDVI_{DHI}$  values observed for *Fagus orientalis*- *Alnus glutinosa*- *Carpinus betulus* ( $0.80 \pm 0.175$ ) and *Fagus orientalis* ( $0.609 \pm 0.097$ ) in the western parcels (zone I), *Parrotia persica*-*Quercus castanefolia* ( $0.801 \pm 0.104$ ) and *Carpinus betulus*-*Acer spp* ( $0.595 \pm 0.052$ ) in the central parcels (zone II), and *Parrotia persica*-*Quercus castanefolia* ( $0.910 \pm 0.050$  and  $0.688 \pm 0.050$ ) in the eastern parcels (zone III) of the study area (Figure 4.5).

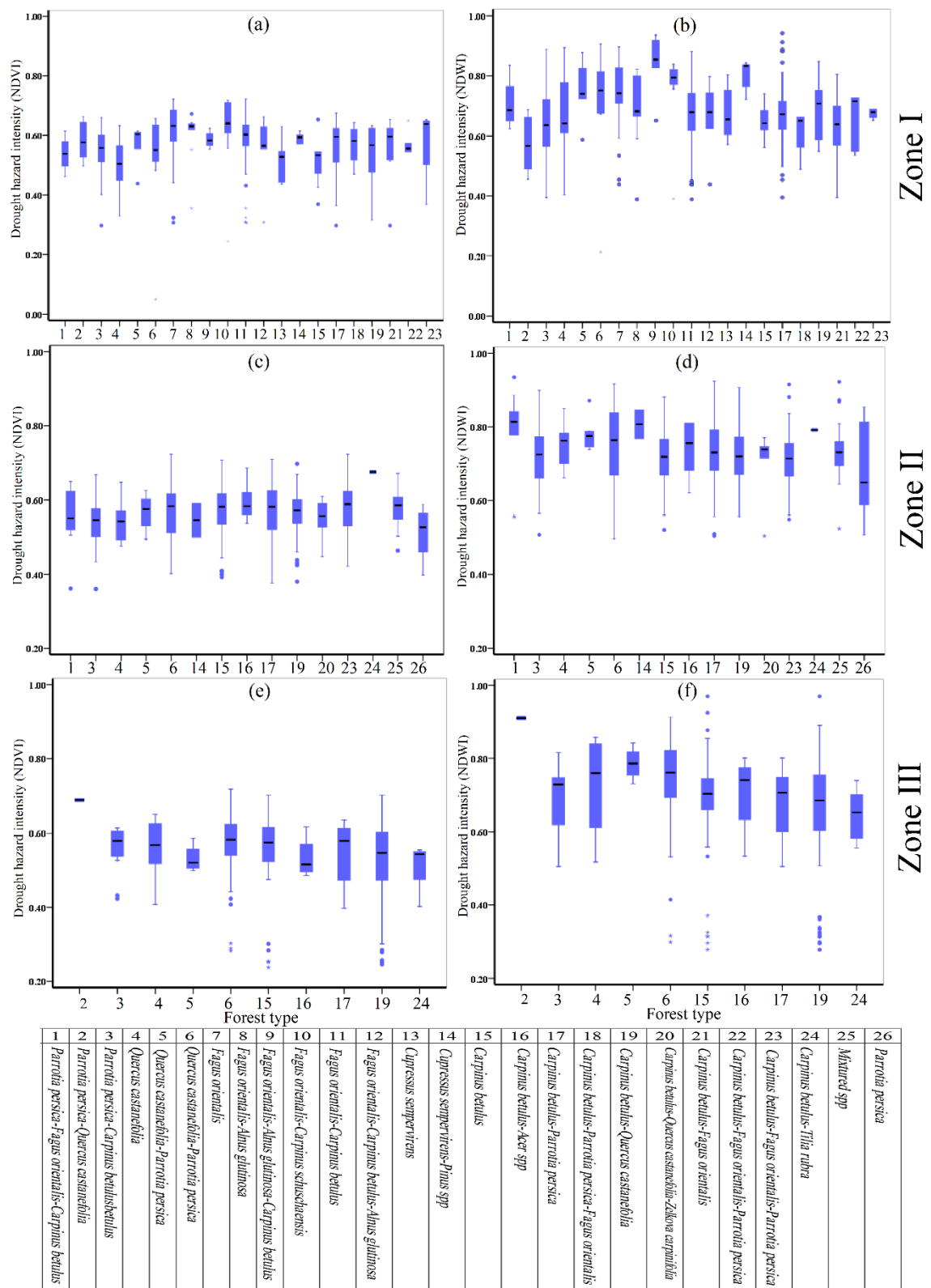


**Figure 4.5** The sensitivity of some forest types to the intensity of forest drought hazards retrieved from the NDVI (a, c and e) and NDWI (b, d, and f) in the western (zone I), middle (zone II) and eastern (zone III) of northeastern Iran.

This high sensitivity of diverse Hyrcanian forest types alerts forest managers that there is a subsequent threat of increasing rates of tree mortality induced by prolonged droughts [47], even under a relative precipitation deficit and moderate heat waves [207–209,235]. Furthermore, analyzing the diversity of tree species mortality showed that commercial species with a high basal area such as *Carpinus betulus*, *Parrotia persica* and *Quercus castanefolia* recorded higher rates of the diversity of mortality in northeastern Iran, especially in the beginning and ending stages of the diebacks. Likewise, the impacts of forest droughts on the large and old tree populations were represented in the previous studies in different forest biomes [184,188,222,236].

This research addressed the impact of meteorological and hydrological droughts on the Hyrcanian forest droughts and dieback, therefore, we would encourage researchers to investigate the implications of other biotic and abiotic agents such as relief, anthropogenic activities, insect infestation and eruptions, and sprawling diseases and wildfires on the forest die-off and tree mortality [12,180] in this region as well.

## 4.7 Conclusion

With the contribution of time series moderate resolution imaging spectroradiometer products, ground-based data and spatial autoregressive models, we developed new analysis approach to investigate the physiological responses of the Hyrcanian forests to the hazard intensity of the meteorological and hydrological droughts in northeastern Iran. We can conclude from the analyses that meteorological droughts more than hydrological droughts affected the water content and greenness properties of the Hyrcanian forests. The impacts of the hazard intensity of high land surface temperatures and actual evapotranspiration were more severe than the hazard intensity of the deficits of precipitation and surface water on the deficit of water content and loss of greenness of Hyrcanian forests. Moreover, the high diversity of tree mortality was significantly correlated with the high values of the hazard intensity of forest droughts. Moderate to die-off stages of tree mortality are predictable through the indicator of forest-water-content deficit (NDWI), however, the only high defoliation stage of tree mortality is predictable through the indicator of forest-greenness loss (NDVI) throughout the Hyrcanian forests. Climax tree species such as *Fagus orientalis* and *Quercus castaneifolia* recorded the higher

rates of hazard intensity of forest droughts and diversity of mortality in this biome. Further studies will have to continue to explore the impacts of other biotic and abiotic agents on the forest die-off and tree mortality of the Hyrcanian region.

## Acknowledgements

This manuscript is a part of the first author's doctoral studies under the supervision of the third author. We benefited greatly from the comments of anonymous reviewers





---

## Climate-Triggered Insect Defoliators and Forest Fires Using Multitemporal Landsat and TerraClimate Data in NE Iran: An Application of GEOBIA TreeNet and Panel Data Analysis

Omid Abdi

### Contributions:

Omid Abdi implemented all parts of this paper including design of the work, the mapping of insect infestation using eCognition® and Salford Predictive Modeler®, analyzing panel data in R, and writing the manuscript.

### Citation:

Abdi, O. Climate-Triggered Insect Defoliators and Forest Fires Using Multitemporal Landsat and TerraClimate Data in NE Iran: An Application of GEOBIA TreeNet and Panel Data Analysis. *Sensors* **2019**, *19*, 3965.

## 5.1 Abstract

Despite increasing the number of studies for mapping remote sensing insect-induced forest infestations, applying novel approaches for mapping and identifying its triggers are still developing. This study was accomplished to test the performance of Geographic Object-Based Image Analysis (GEOBIA) TreeNet for discerning insect-infested forests induced by defoliators from healthy forests using Landsat 8 OLI and ancillary data in the broadleaved mixed Hyrcanian forests. Moreover, it has studied mutual associations between the intensity of forest defoliation and the severity of forest fires under TerraClimate-derived climate hazards by analyzing panel data models within the TreeNet-derived insect-infested forest objects. The TreeNet optimal performance was obtained after building 333 trees with a sensitivity of 93.7% for detecting insect-infested objects with the contribution of the top 22 influential variables from 95 input object features. Accordingly, top image-derived features were the mean of the second principal component (PC2), the mean of the red channel derived from the grey-level co-occurrence matrix (GLCM), and the mean values of the normalized difference water index (NDWI) and the global environment monitoring index (GEMI). However, tree species type has been considered as the second rank for discriminating forest-infested objects from non-forest-infested objects. The panel data models using random effects indicated that the intensity of maximum temperatures of the current and previous years, the drought and soil-moisture deficiency of the current year, and the severity of forest fires of the previous year could significantly trigger the insect outbreaks. However, maximum temperatures were the only significant triggers of forest fires. This research proposes testing the combination of object features of Landsat 8 OLI with other data for monitoring near-real-time defoliation and pathogens in forests.

## 5.2 Introduction

Despite prosperous traditional approaches such as dendrological assessment and field observations for identifying driving forces of insect outbreaks from individual tree to stand scales [6], remotely sensed approaches are extensively progressing either for delineation insect-infested objects or the mensuration of infestations induced by abiotic and biotic agents throughout forest

biomes [76,237–239]. However, some novel algorithms for data mining and machine learning such as TreeNet [77] for delineation insect-infested objects from non-insect-infested objects of images, some high-resolution climate data such as TerraClimate [240] for assessing drought and climate hazards dimensions, and some associations such as interactions between insect outbreaks, forest fires, and climate hazards have received less attention in earlier studies.

Although monitoring the bark beetle infestation and coniferous defoliation are dependent on high-resolution and multi-spectral images [241,242], detecting broadleaved defoliation has been predestined by the spectral–temporal information of images, even by single near-infrared-derived vegetation indices of images with high-temporal resolutions [243]. Moreover, Landsat images have indicated high accuracy for detecting forest-infested patches using either classification algorithms in a specific date [2] or by applying multitemporal spectral-derived indices [63,64,244]. Moderate stages of tree infestation are significantly discernible through multitemporal spectral indices, while the severe infestation is highly discernible through classification approaches [245].

Several numbers of studies exerted data mining and machine learning algorithms such as random forest [75,76,246] and decision tree [247] or maximum likelihood classification [248,249] to discern insect-defoliated from non-insect-defoliated forests. However, numerous remote sensing-derived indices are growing for quantifying the insect-induced defoliation intensity in terms of the long-term archive of Landsat products [63,64,247]. For example, Townsend et al. [64] claimed that Landsat-derived near-infrared (NIR) and short-wave infrared (SWIR) indices such as the normalized different infrared index (NDII) and the moisture stress index (MSI) were superior to the Landsat-derived red and NIR indices such as the normalized difference vegetation index (NDVI) for estimating the defoliation induced by *Lymantria dispar* in the oak forests at five different times. Similarly, Rullán-Silva et al. [63] examined the efficiencies of 10 Landsat-derived vegetation indices for estimating the defoliation induced by *Rhynchaenus fagi* in the beech forests. They concluded that the MSI showed the highest correlation with the intensity of defoliation concerning the mixed-effects model. However, the attitude of analyzing meaningful image-objects for the classification of infested and non-infested forests [250] by the cooperation of image-derived features and GIS-based methods and databases is developing, that is, Geographic Object-Based Image Analysis (GEOBIA) [79]. Besides, earlier results of studies have demonstrated that the combination of object features derived from medium-resolution images such as Landsat and SPOT with ancillary data such as topography has increased the

precision of discerning forest infestations induced by bark beetle [241]. Machine learning algorithms such as random forest improved the classification efficiency with image-derived object features for mapping forest infestations [251]. However, evaluating the efficiency of combination GEOBIA and other machine learning methods such as TreeNet for mapping infested forests induced by defoliators has not been addressed up to now.

Forests are mainly degraded by interactions between abiotic agents such as high temperatures, drought, moisture variability, anthropogenic interventions, and forest fires and biotic agents such as invasive species, tree mortality, insect infestations, and pathogens [4,35–37]. The abiotic agents can trigger the effects of biotic agents, and their synchronization significantly results in tree species' hydraulic deterioration and carbon starvation [2,35–37]. Climate change studies demonstrated that defoliators' population rate during a growing season is correlated to the temperature condition of its hydrological year [252]. Temperature increases can enable insects to survive during the cold season [49–51] and provide rich sources of nutrition from the mature leaves by changing the trees phenology cycle; along with that, they can also increase the risk of insect outbreaks during the growing season [253]. However, there is existing uncertainty about the effects of droughts on the insect outbreaks in the forest biomes [52]. Increasing the droughts' dimensions may result in providing conditions for insect outbreaks [2], tree mortality [5], or increasing the forest fires severity [3]. However, the serious effects of insect defoliators emerge during the moderate drought condition or wetter seasons following droughts occurring [2,35,52,254]. Changes in moisture capacity regarding either high moisture availability [6,255] or low moisture availability [256] are identified as the main driver forcing of some insect outbreaks. The synchronization of droughts following the conditions of above-average moisture availability may result in providing an appropriate condition for insect outbreaks [35] as well.

Mutual interactions between insect infestations and forest fires were documented in some studies [56]. Insect infestations may affect the fuel loads of the tree species and increase the severity of forest fires at landscape-level scales [5,55,56]. However, some studies reported declining the severity of forest fires by increasing the mortality induced by insect attacks [57] or neutral effects of insects and pathogens on the fire characteristics [58,59], particularly in the coniferous forests. Additionally, there is evidence of the probability of increasing the risk of insect outbreaks in those trees that were damaged or weakened following a low severity of forest fires [53] or in fire-induced larger patches of canopy cover [54].

The Caspian Hyrcanian broadleaves and mixed forests have been degrading, as a virgin ecoregion of the temperate forests' biome, by a variety of biotic and abiotic agents such as deforestation [83], forest fires [84], drought [206], and climate hazards with consequences of massive tree mortality [257] in the northeast (NE) Iran during recent decades. Droughts' dimensions could significantly affect the water content and greenness properties of Hyrcanian forests based on the MODIS-derived normalized difference water index (NDWI) and NDVI [206,257]. The stages of moderate to extreme tree mortality events showed a significant association with the high intensity of forest water content deficit derived from the MODIS-NDWI; however, the severe defoliation only showed a significant relationship with the intensity of forest greenness loss derived from NDVI in NE Iran [257]. In addition to climate hazards, drought, and forest fires, there has been rising concerning reports about the outbreaks of some insect defoliators such as *Lymantria dispar*, *Erannis defoliaria*, and *Operophtera brumata* [85,258] as well as pathogens [86,87,259] throughout Hyrcanian forests during recent years. Therefore, this study used TreeNet to delineate insect-infested forests from non-insect-infested forests using numerous Landsat 8 OLI-derived object features, topographic-derived features, and tree species types in Hyrcanian forest, NE Iran. Moreover, it will explore the mutual relationships between the intensity of insect infestation and the severity of forest fires in the presence of TerraClimate-derived climate hazard variables for the period of insect outbreaks and forest fires within the TreeNet-derived insect-infested forest objects.

## 5.3 Materials and Methods

### 5.3.1 Study area

The eastern forests of the Hyrcanian ecoregion were selected for this research. This area is extended from Gorgan to Galikesh in the Golestan province, NE Iran (Figure 5.1). These forests comprise a mixture of broadleaved tree species such as *Quercus castaneifolia*, *Fagus orientalis*, *Carpinus betulus*, *Acer spp.*, *Tilia platyphyllos*, and *Parrotia persica* [82]. The western parts were infested by the defoliators of *Erannis defoliaria* and *Operophtera brumata*, while the eastern parts were affected by *Lymantria dispar* (Figure 5.1). Moreover, the frequency of forest fire events has been increasing in this region during recent years (Figure 5.1).

### 5.3.2 Data and field mensuration

This study identified the insect-infested regions from available reports, local media, and field observations. The attributes of defoliated spots including the type of defoliators, the position, the dominant type of host tree species, and the evidence of current and previous egg-laying were documented. The accurate spatial extent areas of the defoliation were delineated using time-series composite bands of Landsat 8 OLI [260] and the images of Google Earth (Figure 5.2) coincided with the advanced larval stage of insect defoliators (Figure 5.1). A peak of attack was recognized in 2014; the infested objects for this time were delineated from the healthy forest using GEOBIA and TreeNet. The forest fires data were achieved from field surveying, local media, and the available historical database that were provided by the Department of Natural Resources and Watershed Management of Golestan province from 2010 to 2017. The burnt area, duration, and frequency of forest fires were used during a fire season to reach the forest fire severity of a specific location.

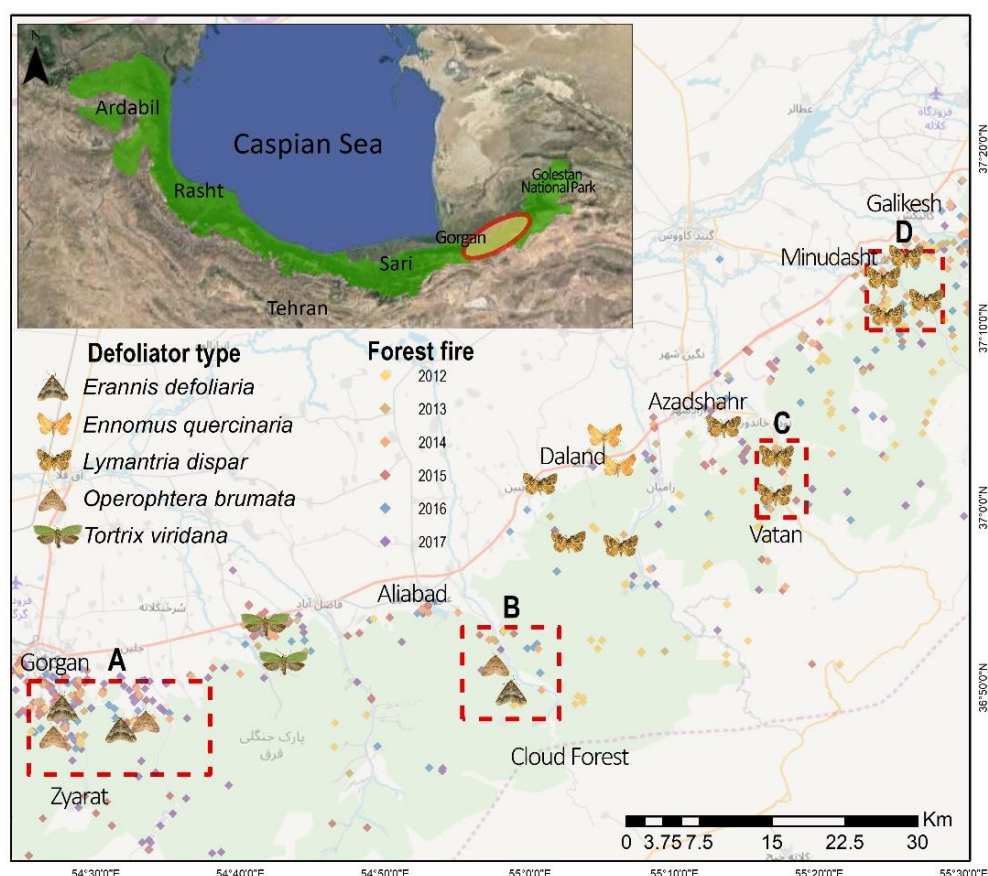


**Figure 5.1** Study area in the Hyrcanian forest ecoregion in the southeast Caspian Sea. Spatial scatter of the insect defoliators and forest fires samples of 2012–2017 in the northeast (NE) Iran. The eastern part of the study area was affected by *Lymantria dispar*, while the western area was affected by *Erannis defoliaria* and *Operophtera brumata*.



We used monthly TerraClimate data for calculating [240] long-term dimensions of anomalies of drought, temperature, and soil moisture from 1987 to 2017. We derived the annual intensity hazard of climate variables from their dimensions as causes of triggering insect attack and forest fires for modelling by the panel data approaches (see Section 5.3.3.3). The ancillary data such as the Topographic Position Index (TPI), Terrain Ruggedness Index (TRI), and Topographic Wetness Index (TWI) were derived from the ALOS PALSAR data elevation [261] for the study area. Forest types were vectorized concerning the scanned maps of the forest management plans [262]. These data were used for mapping insect-infested forests along with Landsat 8 OLI data.

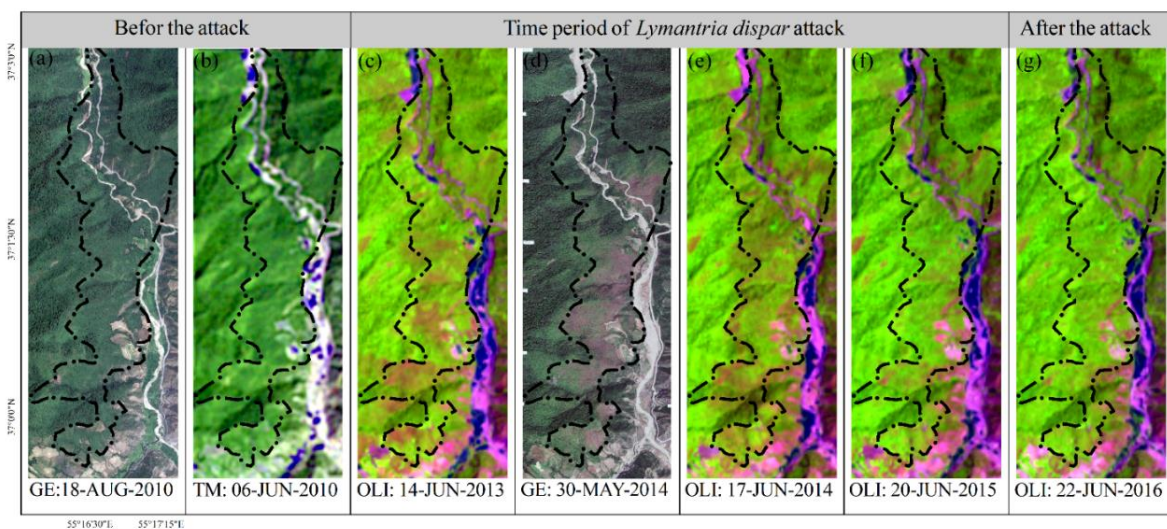


**Figure 5.2** Site C (Figure 5.1): The images of Google Earth (GE) [263] and Landsat 5 TM (SWR, NIR, R) show that the forest was in a healthy condition before the attack of *Lymantria dispar* in 2010 (a, b); the symptoms of the infestation emerged on the Landsat 8 OLI (SWR1, NIR, R) as “olivenite green” in 2013 (c); the insect significantly infested the region based on the GE (d) and Landsat 8 OLI (e) images in 2014, while it declined in 2015 (f) and ended in 2016 (g).

### 5.3.3 Methodology

#### 5.3.3.1 TreeNet-based insect-infestation mapping

GEOBIA was used to delineate the insect-defoliated areas from the healthy forests through image segmentation and TreeNet classification. We derived image objects from a set combination of the main spectral and panchromatic channels of Landsat 8 OLI for the peak times of defoliation (May–June) through the multiresolution segmentation algorithm. To minimize the mean heterogeneity of image objects, we assigned optimal scale parameters by trial and error, with higher weights for the red, NIR, and SWIR bands; the compactness value of 1; and the shape value of 0 in the eCognition Developer 9 [264].

- Object features

Various object features (95 features) were derived from the main channels of Landsat 8 OLI, topography data, and forest types, as shown in Table 5.1. The object features were classified into four main groups including spectral features, surface texture features, geometric features, and the features derived from ancillary data in the GIS. A single database was created including all the derived features of segment objects and was utilized for classification using TreeNet.

**Table 5.1** Object features derived from Landsat 8 OLI channels and ancillary data (topographic and forest data) for discriminating defoliated forests from healthy forests in NE Iran.

Object features	Input data	Features <sup>1</sup> (No.)
Spectral features (32)	Blue, Green, Red, NIR, SWIR1, SWIR2	Mean (6), StdDev (6) of the spectral bands
		Mean & StdDev of spectral indices (14) (IPVI [265], GEMI [266], ARVI [267], GVI [268], NDVI [28], EVI2 [269], NDWI [29])
		Principal components (6) [270], Greenness (2), Wetness (2) [271], Brightness (1), Max. diff. (1)
Surface texture-features (56)	Single bands and all bands in all directions	GLCM <sub>all dir.</sub> (Homogeneity (7), Contrast (7), Dissimilarity (7), Entropy (7), Mean (7), Angle 2nd moment (7), StDev (7), Correlation (7))[272,273]
Geometric features (3)	Objects	Area (1), Compactness (1), Asymmetry(1) [273]
Ancillary data (4)	ALOS PALSAR Forest data	Topographic wetness index [274], Topographic position index [275], Terrain ruggedness index[276], Forest types

<sup>1</sup> StdDev: Standard deviation; IPVI: Infrared percentage vegetation index; GEMI: Global environment monitoring index; ARVI: Atmospherically resistant vegetation index; GVI: Green vegetation index; NDVI: Normalized difference vegetation index; EVI2: Enhanced vegetation index 2; NDWI: Normalized difference water index; GLCM: gray-level co-occurrence matrix.

- TreeNet classification

The stratified random sampling method was used for selecting samples of insect-infested objects (defoliation >50%) and non-insect-infested objects for assessing the object features that control insect outbreaks and discriminate them from the non-insect-affected forests. The TreeNet algorithm was applied for determining influential variables depending on the test sets and generalizing the obtained scores to all feature objects to distinguish between the insect-infested and non-insect-infested objects. Classification in TreeNet is a particular form of regression that produces a possibility of response for a variable and accurately ranks the predictor variables based on their importance from “most likely” to “least likely” to the target variable. TreeNet creates boosting regression models through sequentially fitting a very small tree in several stages. Accordingly, each stage learns from the available training data by a specific learning rate [77].



We applied TreeNet in Salford Predictive Modeler 8.3 [277] to build our model concerning its classification precision, working with both parametric and non-parametric variables, handling big data and missing datasets, connecting to GIS, plotting the univariate and bivariate relationships between the response and predictor variables through partial dependency plots (PDPs), yielding reliable results despite existing non-stationary in data, and ranking the predictor variables in terms of their importance in the model [77,78,278]. One-third of the samples were randomly assigned for the testing set, and the remaining were considered as the learning samples. We set the number of trees and maximum nodes per tree to 500 and 6, respectively. The shrinkage method was chosen as “auto” to eliminate the complexity of overfitting and to set the learning rate of the model, which was calculated to be 0.01. Moreover, we evaluated the number of optimal trees using the criterion of the area under the receiver operating characteristic (ROC) curve and the misclassification rate for the test samples. The confusion matrix was used to assess the performance of the classification model with respect to the test samples using four measures: (1) Sensitivity: the proportion of the insect-infested objects that are correctly classified, (2) Specificity: the proportion of the non-insect-infested objects that are correctly classified, (3) Precision: the proportion of the actual classified insect-infested objects divided by the total number of the insect-infested class testing objects, and (4) an F1 statistic derived from the sensitivity and precision metrics as shown in Equation 5.1, in which its values close to one indicate a high sensitivity of the model:

$$F1\ statistic = \frac{2(Sensitivity \times Precision)}{Sensitivity + Precision} \quad (5.1)$$

### 5.3.3.2 Intensity of insect infestation, the severity of forest fire, and climate hazards

The intensity of defoliation was retrieved by analyzing the long-term deficit of NDWI-derived forest-water content within the TreeNet-derived insect-infested polygons. We calculated the dimensions of defoliation including the severity, frequency, and duration of the yearly defoliations from the anomalies of the Landsat NDWI from 1987 to 2017. The yearly hazard intensity of defoliation was mapped concerning the introduced approach by Abdi et al. [257], which is a combination of standardized values of defoliation dimensions through the fuzzy gamma operator [279].

We obtained the spatial variations and characteristics of daily forest fires from diverse resources from 2010 to 2017. Several studies verified the strength of Landsat-derived burn

severity indices such as the differenced Normalized Burn Ratio (dNBR) [280] and the Relativized dNBR (RdNBR) [281] for large fires; however, some fires' characteristics such as size area, duration, and the type of fire may restrict these indices applications for post-fire monitoring in northeast Iran. Therefore, the severity of forest fires was calculated from the combination of the ground-based characteristics of fires including the frequency, size, and duration of fires within segment objects. The fire characteristics' values were standardized between zero (low) and one (high) by exerting the membership function of fuzzy linear [229]. The severity of forest fires was obtained by overlaying the standardized layers of fire characteristics using the fuzzy gamma operator [279] during a fire season.

TerraClimate data were applied to model the hazard intensity of climate variables throughout the hydrological years (October to September) from 1987 to 2017. The features (i.e., severity, frequency, and duration) of yearly anomalies of the climate variables were combined to obtain the hazard intensity indices of drought, maximum temperatures, and soil moisture deficit using the fuzzy gamma operator [279] as well.

#### 5.3.3.3 Relationships of insect infestation, forest fires and climate hazards

We examined mutual relationships between insect infestation and forest fires in the presence of the hazard intensity of climate variables within the insect-affected objects using the panel data models. To include both the spatial and time effects of the data, we performed the panel data models [282] for the estimation of the intensity of defoliation affected by forest fire severity and climate hazards (Equation 5.2), as well as the severity of forest fires induced by insect defoliation and the climate hazards (Equation 5.3):

$$\text{Insect infestation} = fn(F_{t-1}, D_t, D_{t-1}, T_t, T_{t-1}, S_t, S_{t-1}) \quad (5.2)$$

$$\text{Fire severity} = fn(I_t, I_{t-1}, D_t, D_{t-1}, T_t, T_{t-1}, S_t, S_{t-1}) \quad (5.3)$$

where  $I_t$ ,  $F_t$ ,  $D_t$ ,  $T_t$ , and  $S_t$  are the averages of insect infestation intensity, fire severity, drought intensity, high temperature, and soil moisture deficits in the current year ( $t$ ); and  $I_{t-1}$ ,  $F_{t-1}$ ,  $D_{t-1}$ ,  $T_{t-1}$ , and  $S_{t-1}$  are the averages of these variables for the previous year ( $t-1$ ), respectively.

#### Panel data models

Analyzing the panel data was established based on the combination of multiple observations for the same cross-sections and time series, which is written in a standard model as shown in Equation 5.4 [283]:

$$y_{i,t} = \beta' X_{it} + Z_i \alpha + \varepsilon_{it} \quad (5.4)$$

For  $i = 1, 2, 3, \dots, N$  and  $t = 1, 2, 3, \dots, T$ ; where  $N$  stands for the number of individuals (cross-sections), and  $T$  is the number of times. The vector  $X_{it}$  refers to the  $k$  regressors (Equations 5.2 and 5.3). The vector  $\beta'$  refers to unobserved coefficients, which need to be estimated. The term  $Z_i \alpha$  expresses the cross-section specific effects. The error terms of the model were indicated by  $\varepsilon_{it}$ . Three panel data models are defined regarding the nature of included variables in the vector  $Z_i$ , including the common effects, fixed effects, and also random effects models (Equations 5.5–5.7).

The common effects model does not consider time and cross-sectional effects. The vector  $Z_i$  contains only one constant coefficient:  $\alpha$ . The coefficients of this model are estimated by applying the ordinary least squares (OLS) approach:

$$y_{i,t} = \beta' X_{it} + \alpha + \varepsilon_{it} \quad (5.5)$$

The fixed effects model assumes specific cross-sectional effects from different intercepts to obtain unobserved heterogeneity. The parameter of fixed effect  $\alpha_i$  is constantly estimated over time with the estimators' normality assumption. This model assumes that cross-sectional effects are correlated with the included regressors  $X_{it}$ :

$$y_{i,t} = \beta' X_{it} + \alpha_i + \varepsilon_{it} \quad (5.6)$$

The random effects model assumes that unobserved cross-sectional heterogeneity is not correlated to the included regressors  $X_{it}$ . The coefficients of this model are estimated using the generalized least squares (GLS) estimator:

$$y_{i,t} = \beta' X_{it} + \alpha + \mu_{it} \quad (5.7)$$

$$\mu_{it} = \alpha_i + \varepsilon_{it}$$

The random effects model is preferable to the fixed effect model if samples were taken from a larger population and the estimations' generalization to the population was aimed. The higher accuracy of estimates and greater flexibility of this model were reported in comparison with the fixed effects model [284,285] as well.

#### Testing for fixed effects and random effects

Tests were accomplished to make a distinction between panel data models. The Chow test was used for testing fixed effects against common effects [283], which determines whether a single regression model (common effects) is superior to the two separate regression models (fixed effects). The Hausman's specification test [286] was used for selecting whether the fixed effects model or the

random effects model is appropriate [287]. The Hausman test makes a distinction between a model that assumes its cross-sectional effects are not correlated with its regressors (random effects), and a model that assumes that these relationships are established (fixed effects) [283].

## 5.4 Results

### 5.4.1 Insect defoliation mapping

The highest performance of TreeNet was obtained after the formation of 333 trees with the optimal ROC value of 93.4% for discriminating insect-infested and non-insect-infested forest objects. The model results using 83 out of 95 predictor variables yielded average correctness of 87% for testing samples to predict the insect-infested and non-insect-infested forests (Table 5.2).

**Table 5.2** Classification correctness of test samples for the TreeNet analysis to discriminate the insect-infested from the non-insect-infested forests in NE Iran

Measure	Average	Overall accuracy	Specificity	Sensitivity	Precision	F1 statistic
Percent	87.15	86.76	80.56	93.75	81.08	86.96

Relative variable importance values describe that the top predictors are the mean of PC2, tree species, and the mean of the red channel derived from the grey-level co-occurrence matrix (GLCM), NDWI, and global environment monitoring index (GEMI) (Figure 5.3). The positive log-odds values of the insect-infested class were significantly increased when the mean of the PC2 values had passed the point of 0.70. Tree species with the domination of *Carpinus betulus-Quercus castaneifolia* and *Carpinus betulus-Acer spp.-Tilia platyphyllos* exhibited the highest partial relationships with the insects' presence. The average log-odds values of the insect-infested class were increased from -0.287 to 0.314, where the mean of the red band derived from GLCM ranged from 122 to 130. The average log-odds dropped at values of 0.264 and 0.635 of the NDWI and GEMI, respectively, where the probability of infestation also reduced (Figure 5.4). The TreeNet model was rebuilt with respect to the top influential object features that have gained a minimum score of 15% importance relative to the most important variable. The insect-infested and non-insect-infested map was created with the contribution of the top 22 predictor variables over the study area (Figure 5.5). The hazard intensity of defoliation derived from the time-series anomaly of Landsat-NDWI was mapped as an insect infestation indication within the delineated insect-infested forest objects from 2010 to 2017 (Figure 5.6). The maps demonstrated that the infestation intensity was considerable in 2011, 2014, and 2015 (Figure 5.6b,e,f).

(a) Bar chart showing model output for various tree species combinations. The y-axis ranges from -0.9 to 0.5. The x-axis lists combinations such as Quercus castaneifolia-Carpinus betulus-Parrotia persica, Carpinus betulus-Quercus castaneifolia-Parrotia persica, Pinus spp., etc.

(b) Line graph showing model output versus Me.PC2. The y-axis ranges from -0.4 to 0.6. The x-axis ranges from 0.65 to 0.79. The output starts at approximately -0.4, rises sharply around 0.71, and plateaus near 0.5.

(c) Line graph showing model output versus Me.GLCM\_R. The y-axis ranges from -0.3 to 0.4. The x-axis ranges from 116 to 138. The output starts at approximately -0.3, rises sharply around 126, and plateaus near 0.3.

(d) Line graph showing model output versus Me.NDWI. The y-axis ranges from -0.5 to 0.2. The x-axis ranges from 0.10 to 0.34. The output starts at approximately 0.15, remains relatively stable until 0.26, then drops sharply to about -0.45.

(e) Line graph showing model output versus Me.GEMI. The y-axis ranges from -0.08 to 0.1. The x-axis ranges from 0.5 to 0.9. The output starts at approximately 0.09, remains stable until 0.68, then drops sharply to about -0.07.

**Figure 5.4** Univariate partial dependency graphs for the top five-predictor variables for classification of insect-infested forests in NE Iran. Positive values of the outputs indicate a direct association of a class of the categorical variables or values of the continuous variables with the focus class. Eight tree species show positive relationships with the infested class (a), the mean of PC2 and the mean of red band derived from GLCM show a positive association at values of greater than 0.711 (b) and 126.30 (c), and the mean values of the NDWI and GEMI show a positive relationship with the presence of infestation until the values of 0.267 (d) and 0.697 (e).

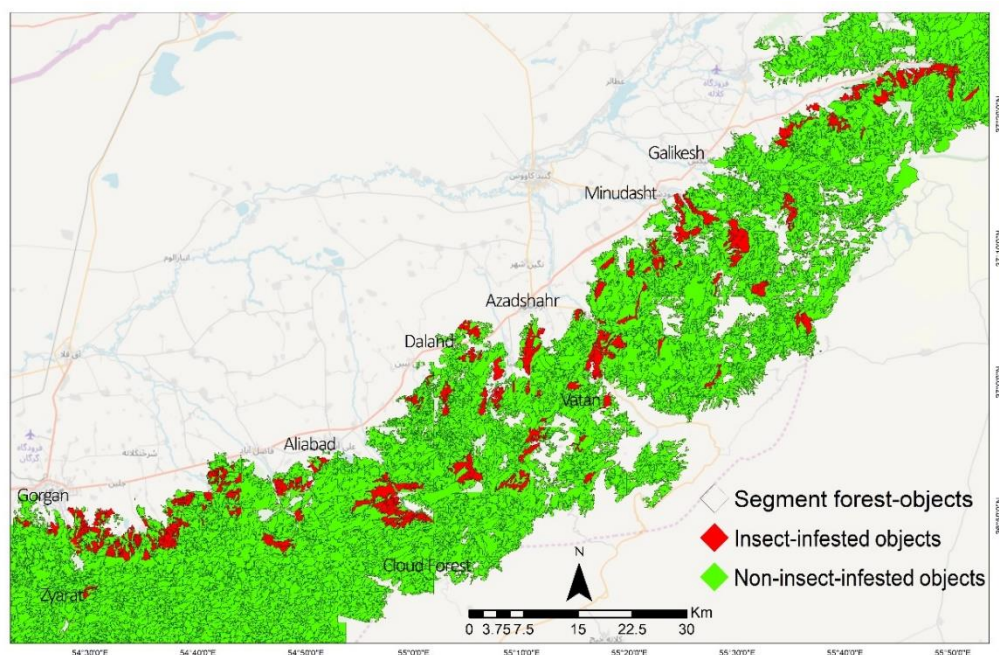


**Figure 5.5** The insect-affected and non-insect-affected forest-objects derived from the influential object features of Landsat 8 OLI and ancillary data using Geographic Object-Based Image Analysis (GEOBIA) and TreeNet in the Hyrcanian region, NE Iran.

#### 5.4.2. Insect infestation, forest fires and climate hazards modelling

The results of the Hausman test indicate that the random effects model was superior to the fixed effects model for the variables expressing that control either the intensity of insect infestation ( $X^2 = 11.87$ ,  $df = 7$ ,  $p = 0.105$ ) or severity of forest fires ( $X^2 = 6.72$ ,  $df = 8$ ,  $p = 0.567$ ). Furthermore, the results of the Chow test showed that the fixed effects model was superior to the common effects in both models ( $X^2 = 37.39$ ,  $df = 18$ ,  $p = 0.004$ ;  $X^2 = 43.31$ ,  $df = 18$ ,  $p = 0.000$ ).

The summary of the random effects model reveals that the drought condition (SPI), maximum temperature (Tmax), and the deficit of soil moisture of the current year—along with the maximum temperature, high soil moisture availability, and the severity of forest fires of the previous year—were the significant variables, which are controlling the insect infestation intensity during 2010–2017 in the study area (Table 5.3). However, the intensity of drought of the previous year was not significant, but its coefficient is positive. Although the majority of climate hazards demonstrated positive coefficient with the severity of forest fires, Tmax of the current year ( $\beta = 0.330$ ,  $P < 0.05$ ) and Tmax of the previous year ( $\beta = 0.196$ ,  $P < 0.01$ ) were the only significant variables. The insect infestation (II) of the previous year showed a positive relationship with the severity of forest fire as well; however, it is not statistically significant ( $\beta = 0.106$ ,  $P > 0.05$ ) in NE Iran (Table 5.4).



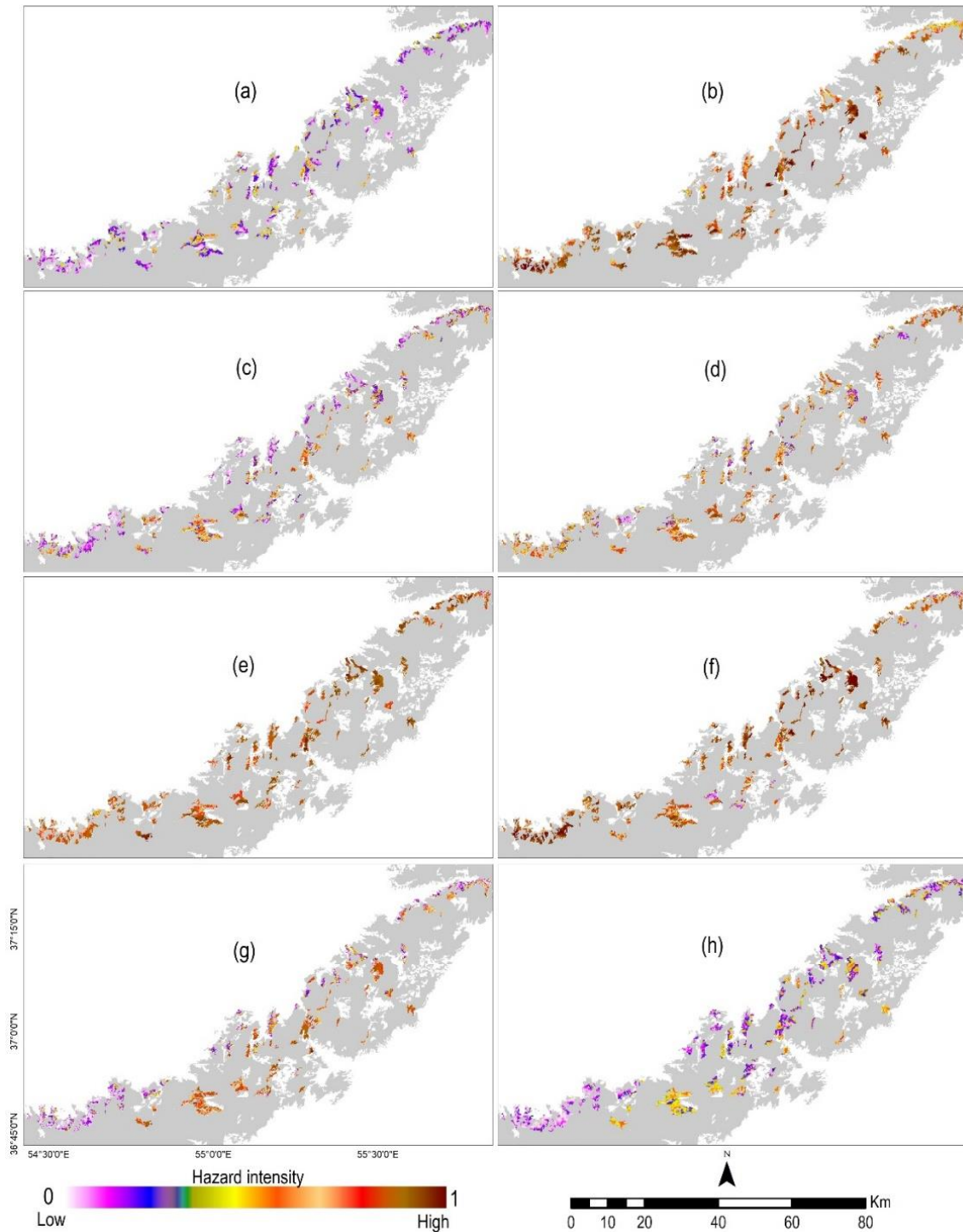


**Figure 5.6** The yearly hazard intensity of defoliation for the time period of 2010 to 2017 (a–h) within the insect-infested forest objects. The monthly anomalies of NDWI were obtained from the time series of Landsat 5, 7, and 8 from 1987 to 2017. The dimensions of forest water content deficit including severity, frequency, and duration were derived from Landsat–NDWI anomalies for the period of defoliation (2010–2017). The values of these dimensions were standardized by the membership functions of fuzzy linear and fuzzy large between zero and one. The hazard intensity of defoliation was obtained by overlaying the standardized layers of dimensions of the NDWI anomalies using the fuzzy gamma operator within the insect-infested segment objects during a growing season in Hyrcanian forests, NE Iran.

**Table 5.3** Results of panel data models for relationships between the intensity of insect infestation with the intensity of climate hazards of the current year and previous year as well as forest fires of the previous year in NE Iran.

Model	Constant	SPI <sub>t</sub>	SPI <sub>t-1</sub>	Tmax <sub>t</sub>	Tmax <sub>t-1</sub>	SoilM <sub>t</sub>	SoilM <sub>t-1</sub>	Fire <sub>t-1</sub>	R <sup>2</sup>
Common effects	0.204**	0.184*	0.070 <sup>ns</sup>	0.463*	0.165*	0.144*	-0.134*	0.171*	0.680
Fixed effects	0.290**	-0.039 <sup>ns</sup>	-0.080 <sup>ns</sup>	0.762**	0.367*	0.152*	-0.072 <sup>ns</sup>	0.154*	0.798
Random effects	0.210**	0.153*	0.048 <sup>ns</sup>	0.718**	0.321*	0.146*	-0.126*	0.194*	0.706

\*\* p-value < 0.01, \* p-value < 0.05, and ns: not significant. SPI: standardized precipitation index; Tmax: maximum temperature; SoilM: soil moisture deficit; Fire: forest fire; *t*: current time; and *t-1*: previous time.

**Table 5.4** Results of panel data models for relationships between the severity of forest fires with the intensity of climate hazards and insect infestation of the current year and the previous year in NE Iran.

Model	Constant	SPI <sub>t</sub>	SPI <sub>t-1</sub>	Tmax <sub>t</sub>	Tmax <sub>t-1</sub>	SoilM <sub>t</sub>	SoilM <sub>t-1</sub>	II <sub>t</sub>	II <sub>t-1</sub>	R <sup>2</sup>
Common effects	-0.0169 <sup>ns</sup>	-0.085 <sup>ns</sup>	0.030	0.385*	0.177*	0.032 <sup>ns</sup>	-0.163 <sup>ns</sup>	-0.059 <sup>ns</sup>	0.105 <sup>ns</sup>	0.210
Fixed effects	-0.032 <sup>ns</sup>	-0.113 <sup>ns</sup>	0.094 <sup>ns</sup>	0.254 <sup>ns</sup>	0.213**	0.049 <sup>ns</sup>	-0.126 <sup>ns</sup>	-0.031 <sup>ns</sup>	0.106 <sup>ns</sup>	0.550
Random effects	-0.017 <sup>ns</sup>	-0.101 <sup>ns</sup>	0.117 <sup>ns</sup>	0.330*	0.196**	0.041 <sup>ns</sup>	-0.148 <sup>ns</sup>	-0.020 <sup>ns</sup>	0.106 <sup>ns</sup>	0.236

\*\* p-value < 0.01, \* p-value < 0.05, and ns: not significant. SPI: standardized precipitation index; Tmax: maximum temperature; SoilM: soil moisture deficit; II: insect infestation intensity; *t*: current time; and *t-1*: previous time.

## 5.5 Discussion

This study exerted novel remote sensing-based data collections (e.g., Landsat and TerraClimate) and approaches (e.g., TreeNet and panel data models) to discern insect-infested forests and quantify the multitemporal intensity of forest defoliation, climate hazards, drought, and the severity of forest fires along with modelling their temporal and spatial interactions in NE Iran.

We obtained reliable discrimination between insect-infested forests and non-insect-infested forests (Table 5.2) using the important collections of Landsat 8 OLI-derived and ancillary object features using the TreeNet algorithm. The summary of variable importance represented that the object features extracted from the Landsat channels show higher performance in comparison with the main spectral channels of Landsat (Figure 5.3). For example, the highest value recorded for the mean of PC2, and after that the mean of red channel derived from GLCM and the mean values of vegetation indices, including the NDWI



and GEMI, respectively. Analyzing one partial dependency revealed that the probability of the presence of defoliation increases along with the increase of average values of the PC2 and the mean of the red channel derived from GLCM, while it decreases by the increase of values of the NDWI and GEMI (Figure 5.3). The PC2 was positively loaded on the visible bands of Landsat 8 OLI with a higher coefficient for the red and green bands, which high-defoliated forest objects have obtained high values on PC2 (Figure 5.4b). The increase in the reflectance of some ranges of visible wavelengths due to the vegetation stress was reported in earlier studies [288,289], which are near to the green and red bands of Landsat 8 OLI. In contrast, PC2 was loaded negatively on the NIR and SWIR bands, as the objects with high biomass showed lower values on the PC2. While our analysis indicated that the PC2–Landsat 8 OLI is the top variable predictor, the third principal component (PC3) was positively loaded on the red band and showed considerable importance value in discriminating between insect-infested forest objects and healthy forest objects (Figure 5.3) as well. Also, the ability of PC3 was reported for identifying year-to-year forest defoliation by *Lymantria dispar* L. using the time series of SPOT [290]. Moreover, the importance of Landsat-derived indices was presented for detecting insect-affected forests for different types of insects in other biomes [63,64,247]. This study results confirm that vegetation indices with respect to the NIR–SWIR (i.e., NDWI) are superior to those vegetation indices that are depending on the visible NIR channels for the delineation of insect-infested forest objects [63,64] in the Hyrcanian ecoregion as well.

Insect defoliators can affect the structure of vegetation [291]; therefore, image-derived textural attributes are appropriate for detecting insect-defoliating forest objects. However, the mean of the red channel derived from GLCM was among the top five predictors; Figure 5.3 indicates that about one-third of effective predictor variables are categorized in the first-order or second-order textural attributes for detecting the defoliation induced by insects in NE Iran. The superiority of image textures derived from GLCM and grey-level occurrence matrices (GLOM) [291,292] for detecting vegetation degradation induced by insect defoliation has been particularly demonstrated for the high spatial resolution images.

The results of variable importance describe that the type of tree species has a significant effect on the insect outbreaks as well. However, the partial dependence plot shows that mixed forest stands such as *Carpinus betulus* and *Quercus castaneifolia* with the other tree species types were highly correlated with the positive values of probability infestation in the Hyrcanian

forests (Figure 5.4a). However, some studies reported insect defoliation in the monospecific stands in the other forest biomes [63,242,293].

The results of interactions between the intensity of insect defoliation with the intensity of climate hazards demonstrated that Tmax, drought, and soil moisture significantly increased the intensity of insect infestation. Both current and previous temperatures presented significant coefficients (Table 5.3). The high temperatures of the previous year can enable insects to survive during the winter [49–51] and change the cycle of forest phenology with the insect outbreaks consequences during the growing season [253].

Although some studies reported uncertainty about the effect of drought on the insect eruption [52], this study's analyses confirmed that drought condition is a key trigger of increasing insect outbreaks in Hyrcanian broadleaved forests (Table 5.3). This area has experienced severe droughts from 2010 to 2011 [206]; however, the wetter seasons during 2012 and 2013 provided the condition for eruption insects during moderate drought seasons. Also, these fluctuations in the wet and dry seasons have been reported as a trigger of insect outbreaks [35]. The panel data models using random effects verified that the soil moisture availability [6,255] in the previous year significantly increased the intensity of insect infestation (Table 5.3). However, the effect of the deficit of soil moisture in the current year was not strongly significant; its positive coefficient indicates that it was more likely that it intensified the insect eruption [256]. Therefore, the conditions of the previous year regarding its high temperatures and availability of moisture have supplied the sources of nutrients for insects and caused massive outbreaks in the current year with existing high temperatures and drought conditions. Earlier studies emphasized that high temperature is the main cause of increasing the intensity of tree mortality in the Hyrcanian forests [257].

Moreover, the random effects model indicated that the severity of forest fires of the previous year was a significant driver in increasing the intensity of insect infestation (Table 5.3). The trends of forest fires were dramatically increased following 2010 in the study area (Figure 5.1). Since the majority of the type of fires are classified as surface fires and single-tree burning in the study area, the likelihood of damaging trees [53] and opening fire-induced spaces [54] have increased the risk of insect infestation in these spots. The presence of insect defoliators was higher in the locations with a high density of fires (Figure 5.1). In contrast, the intensity of insect defoliation either in the current year or in the previous year was not a

significant trigger for increasing the severity of forest fires in the Hyrcanian ecoregion (Table 5.4). The neutral effects of insect infestation on fire severity were demonstrated in the studies accomplished by Meigs et al. [58] and Kane et al. [59] as well. However, some researchers concluded that insect-induced tree mortality has decreased fuels and associated fire proneness, resulting in declining fire severity [57]. We can justify these results for two reasons in Hyrcanian forests: (1) insect infestations have not yet led to such massive tree mortality that could load extensive fuels for fires [5,55,56] in this area, and (2) human activities are identified as the main causes of fires in this area, and mostly occurred in the condition of high temperatures [84]. This study confirmed that the maximum temperature of the current year and previous year are the only significant variables controlling forest fires in the Hyrcanian ecoregion (Table 5.4).

Landsat 8 OLI-derived features have shown reasonable efficiency for mapping insect-defoliated Hyrcanian mixed broadleaved forests for the investigated periods. Alternatively, this study proposes testing the capabilities of new data such as Sentinel-2 with higher spectral, spatial, and swath width that can produce dense time series, which are more appropriate for monitoring near-real-time insect infestation. There have been increasing reports about the outbreaks of other biotic agents such as bark beetles and pathogens in the Hyrcanian forests [86,87,259]; therefore, further investigations are required for identifying the spatial extent of these agents and exploring their triggers. Furthermore, separating mortality induced by insect defoliators from bark beetles or pathogens should be scrutinized.

## 5.6 Conclusions

This study has designed an object-based TreeNet framework to discern insect-defoliated forests using Landsat 8 OLI-derived and ancillary object features. Furthermore, we performed panel data models for quantifying the effects of TerraClimate-derived climate hazards on insect outbreaks and forest fires along with mutual associations of insect infestation and forest fires in the Hyrcanian broadleaved mixed forests, NE Iran. According to the analyses, we drew the following conclusions:

1. GEOBIA TreeNet indicated excellent performance with the contribution of Landsat 8 OLI-derived and ancillary object features for discriminating insect-defoliated forests from healthy forests.
2. Although the object features of Landsat 8 OLI recorded higher importance for discriminating insect-defoliated objects, tree species has obtained the second rank of importance following the mean of PC2. In addition, other top image object features were the mean of the red channels derived from GLCM, the mean of NDWI, and the mean of GEMI, respectively.
3. The random effects model demonstrated higher performance in comparison with the fixed effects and common effects models to model the mutual interaction of the intensity of insect defoliation and the severity of forest fire and their associations with the TerraClimate-derived climate hazards.
4. Maximum temperatures significantly triggered both insect outbreaks and forest fires. Although the drought conditions of the current year and the availability of soil moisture of the previous year were significant regarding the intensity of insect infestation, they have indicated neutral effects on the severity of forest fires.
5. The severity of forest fires of the previous year has triggered the intensity of insect infestation; however, the insect infestation was not effective for the forest fires.
6. Future studies will be required to explore the application of novel satellite images such as Sentinel-2 or the combination of Landsat 8 and Sentinel-2 for monitoring near-real-time insect-induced defoliation, identifying infestations resulting from bark beetles and pathogens, and discriminating between them.

## Acknowledgements

The author acknowledges support by the German Research Foundation and the Open Access Funding by the Publication Fund of the TU Dresden. The author expresses his acknowledgement to the Department of Natural Resources and Watershed Management of Golestan for providing some forest information and fire attributes during the research.

---

## Conclusions and Outlook

### 6.1 Concluding remarks

- The presented study has applied several models for quantifying the relations among variables including common regression models (Chapter 2), spatial autocorrelations (Chapter 3), spatial regression models (Chapter 4), and panel data models (Chapter 5). The overall evaluation revealed that there is evidence of spatial dependence in the models, that is, some models such as spatial error, spatial lag, and random effects models were superior to the ordinary least square model.
- This research progressively improved the analysis of physiological responses of forests to droughts from the only studying their severity (Chapter 3) to analyses concerning severity, frequency, and duration of anomalies (Chapter 4 and 5).
- The analysis of 17-year of MODIS-derived vegetation anomalies revealed that droughts affected both greenness and water content properties of forests and rangelands in NE Iran. The forests strongly responded to precipitation deficits during the middle of the growing seasons, while the rangelands responded to this condition throughout the growing seasons. The anomalies of the rangelands' water content demonstrated higher spatial correlations with the anomalies of precipitation in comparison to their greenness. Some clusters with highly degraded forests did not show significant associations with those that highly affected by droughts, and vice versa (Chapter 3). We conclude that precipitation deficit could not solely determine the

physiological response of forests to drought conditions but other climatic and hydrologic variables may also be relevant (Chapter 4).

- More specifically, the hazard intensity of forest droughts showed higher spatial relationships with increases in temperatures and evapotranspiration rather than with decreases in precipitation and surface water level (Chapter 4).
- The diversity of tree mortality was significantly dependent on the intensity of MODIS-derived forest droughts. The stages of moderate to extreme tree mortality demonstrated significant spatial relations with the high intensity of the forests' water content, but only the stage of severe defoliation was associated with the intensity of forest greenness loss. The Hyrcanian climax tree species were affected by the higher intensity of forest droughts and recorded a higher diversity of tree mortality as well (Chapter 4).
- Further research was required to investigate the biotic and abiotic agents that could trigger by droughts and climate hazards such as insect defoliators and forest fires (Chapter 5).
- Analyses of multitemporal Landsat, TerraClimate and forest fires data demonstrated that maximum temperatures, precipitation deficit, availability of soil moisture and forest fires of the previous year could significantly trigger insect outbreaks during 2010–2017. However, maximum temperatures were the only significant triggers of forest fires during this time (Chapter 5). The analysis of intermittent fires in 2010—from the earlier study—indicated that a combination of environmental, climatic and anthropogenic factors can control fire severity related to critical facts like forest density, daily mean temperatures, daily mean wind speed, and the low density of forest roads (Chapter 2).

## 6.2 Outlook

- The present research assessed forest droughts using the anomalies of NDVI, EVI, and NDWI derived from MODIS data. We suggest that the efficiency of combined indices such as NDDI and NMDI will be evaluated for this purpose.
- So far we excluded human-caused degraded forests and rangelands from the green areas within the applied time-series images for near-real modelling of forest responses

to meteorological and hydrological droughts; however, other drivers may degrade forests and affect the values of satellite-derived indices such as flooding, landslides, forest fires, insect infestations, pathogens, logging, mining, and tourism. These should also be addressed in future studies.

- Climate data substantially contributed to evaluating forest droughts with satellite-derived vegetation indices. Further ancillary data such as physical, environmental and vegetation species information may enhance the performance of VIs for quantifying drought severity in forests and rangelands.
- We checked the relations of anomalies of forests, climate hazards and tree mortality within grid-cell tessellations, which showed that there is a risk of heterogeneity and noise values of variables within a grid-cell that may affect the results. Using object-based analysis may facilitate the study of associations among variables by aggregating similar neighbour cells in a single object and summarizing the attributes of all variables within that object.
- TreeNet GEOBIA yielded satisfactory results for discerning insect-defoliated forests from healthy forests; its capability for analyzing other forest disturbances such as bark beetles, forest fires, and pathogens needs to be explored. Moreover, future studies concerning detection of the insect-affected forests can focus on the object features of other satellite data that have wider wavelengths in the range of the red-edge such as Sentinel-2 and Hyperion data.
- Although the spatial regression models such as spatial lag (SL) and spatial error (SE) demonstrated a better performance than common regression model (OLS) for analyzing relations between anomalies of forests and climate hazards as well as the diversity of tree mortality, regarding their limitations for analyzing big data in the current situation, one strategy would be to apply machine-learning algorithms for this purpose that can handle big and missing data easily.
- This research dealt with the eastern part of Hyrcanian forests. We propose to test the presented or suggested approaches to even better assess the responses of the remaining Hyrcanian forests in the western and central regions of northern Iran to climate hazards.





## References

1. Vose, James M., David L. Peterson, and Toral Patel-Weynand. *Effects of climatic variability and change on forest ecosystems: a comprehensive science synthesis for the US*. en. Tech. Rep. PNW-GTR-870. Portland, OR: US Department of Agriculture, Forest Service, Pacific Northwest Research Station, 2012.
2. Senf, C.; Wulder, M.A.; Campbell, E.M.; Hostert, P. Using Landsat to Assess the Relationship Between Spatiotemporal Patterns of Western Spruce Budworm Outbreaks and Regional-Scale Weather Variability. *Canadian Journal of Remote Sensing* **2016**, *42*, 706–718, doi:10.1080/07038992.2016.1220828.
3. Littell, J.S.; Peterson, D.L.; Riley, K.L.; Liu, Y.; Luce, C.H. Fire and Drought. *Effects of drought on forests and rangelands in the United States: a comprehensive science synthesis*; U.S. Department of Agriculture, Forest Service: Washington, DC, 2016; pp 135–154.
4. Kautz, M.; Meddens, A.J.H.; Hall, R.J.; Arneeth, A. Biotic disturbances in Northern Hemisphere forests - a synthesis of recent data, uncertainties and implications for forest monitoring and modelling. *Global Ecol. Biogeogr.* **2017**, *26*, 533–552, doi:10.1111/geb.12558.
5. Fettig, C.J.; Mortenson, L.A.; Bulaon, B.M.; Foulk, P.B. Tree mortality following drought in the central and southern Sierra Nevada, California, U.S. *Forest Ecology and Management* **2019**, *432*, 164–178, doi:10.1016/j.foreco.2018.09.006.
6. Swetnam, T.W.; Lynch, A.M. Multicentury, Regional-Scale Patterns of Western Spruce Budworm Outbreaks. *Ecological Monographs* **1993**, *63*, 399–424, doi:10.2307/2937153.
7. Eilmann, B.; Weber, P.; Rigling, A.; Eckstein, D. Growth reactions of *Pinus sylvestris* L. and *Quercus pubescens* Willd. to drought years at a xeric site in Valais, Switzerland. *Dendrochronologia* **2006**, *23*, 121–132, doi:10.1016/j.dendro.2005.10.002.
8. Pichler, P.; Oberhuber, W. Radial growth response of coniferous forest trees in an inner Alpine environment to heat-wave in 2003. *Forest Ecology and Management* **2007**, *242*, 688–699, doi:10.1016/j.foreco.2007.02.007.
9. Weber, P.; Bugmann, H.; Rigling, A. Radial growth responses to drought of *Pinus sylvestris* and *Quercus pubescens* in an inner-Alpine dry valley. *Journal of Vegetation Science* **2007**, *18*, 777–792, doi:10.1111/j.1654-1103.2007.tb02594.x.
10. Castagneri, D.; Nola, P.; Motta, R.; Carrer, M. Summer climate variability over the last 250 years differently affected tree species radial growth in a mesic Fagus–Abies–Picea old-growth forest. *Forest Ecology and Management* **2014**, *320*, 21–29, doi:10.1016/j.foreco.2014.02.023.
11. Lévesque, M.; Rigling, A.; Bugmann, H.; Weber, P.; Brang, P. Growth response of five co-occurring conifers to drought across a wide climatic gradient in Central Europe. *Agricultural and Forest Meteorology* **2014**, *197*, 1–12, doi:10.1016/j.agrformet.2014.06.001.
12. Zhang, Y.; Peng, C.; Li, W.; Fang, X.; Zhang, T.; Zhu, Q.; Chen, H.; Zhao, P. Monitoring and estimating drought-induced impacts on forest structure, growth, function, and ecosystem services using remote-sensing data: recent progress and future challenges. *Environ. Rev.* **2013**, *21*, 103–115, doi:10.1139/er-2013-0006.

13. Frey, C.M.; Kuenzer, C.; Dech, S. Quantitative comparison of the operational NOAA-AVHRR LST product of DLR and the MODIS LST product V005. *International Journal of Remote Sensing* **2012**, *33*, 7165–7183, doi:10.1080/01431161.2012.699693.
14. Song, Z.; Kuenzer, C.; Zhu, H.; Zhang, Z.; Jia, Y.; Sun, Y.; Zhang, J. Analysis of coal fire dynamics in the Wuda syncline impacted by fire-fighting activities based on in-situ observations and Landsat-8 remote sensing data. *International Journal of Coal Geology* **2015**, *141–142*, 91–102, doi:10.1016/j.coal.2015.03.008.
15. Menenti, M.; Malamiri, H.R.G.; Shang, H.; Alfieri, S.M.; Maffei, C.; Jia, L. Observing the Response of Terrestrial Vegetation to Climate Variability Across a Range of Time Scales by Time Series Analysis of Land Surface Temperature. In *Multitemporal remote sensing: Methods and applications / Yifang Ban, editor; Ban, Y., Ed.*; Springer: Cham, Switzerland, 2016; pp 277–315, ISBN 978-3-319-47035-1.
16. Huffman, G.J.; Adler, R.F.; Bolvin, D.T.; Nelkin, E.J. The TRMM Multi-Satellite Precipitation Analysis (TMPA). In *Satellite Rainfall Applications for Surface Hydrology*; Gebremichael, M., Hossain, F., Eds.; Springer Netherlands: Dordrecht, 2010; pp 3–22, ISBN 978-90-481-2914-0.
17. Kuenzer, C.; Dech, S.; Wagner, W. Remote Sensing Time Series Revealing Land Surface Dynamics: Status Quo and the Pathway Ahead. In *Remote sensing time series: Revealing land surface dynamics / Claudia Kuenzer, Stefan Dech, Wolfgang Wagner, editors; Kuenzer, C., Dech, S.W., Wagner, W., Eds.*; Springer: Cham, 2015; pp 1–24, ISBN 978-3-319-15966-9.
18. Verbesselt, J.; Hyndman, R.; Newnham, G.; Culvenor, D. Detecting trend and seasonal changes in satellite image time series. *Remote Sensing of Environment* **2010**, *114*, 106–115, doi:10.1016/j.rse.2009.08.014.
19. Nagarajan, R. *Drought assessment*; Springer: Dordrecht, 2009, ISBN 9789048125005.
20. Wilhite, D.A.; Buchanan-Smith, M. Drought as hazard: Understanding the natural and social context. In *Drought and Water Crises: Science, Technology, and Management Issues*; Wilhite, D.A., Ed.; CRC Press, 2005; pp 3–29, ISBN 9780429120091.
21. Squires, V.R. Chapter 2: Desertification and Drought. In *Handbook of Drought and Water Scarcity*; Eslamian, S., Eslamian, F., Eds.; CRC Press: London, 2017; pp 13–26, ISBN 9781498731027.
22. Dalezios, N.R.; Gobin, A.; Tarquis Alfonso, A.M.; Eslamian, S. Chapter 5: Agricultural Drought Indices: Combining Crop, Climate, and Soil Factors. In *Handbook of Drought and Water Scarcity*; Eslamian, S., Eslamian, F., Eds.; CRC Press: London, 2017; pp 73–89, ISBN 9781498731027.
23. Luce, C.H.; Pederson, N.; Campbell, J.; Millar, C.; Kormos, P.; Vose, J.M.; Woods, R. Chapter 2: Characterizing Drought for Forested Landscapes and Streams. *Effects of drought on forests and rangelands in the United States: a comprehensive science synthesis*; U.S. Department of Agriculture, Forest Service: Washington, DC, 2016; pp 16–48.
24. Domingo, C.; Pons, X.; Cristóbal, J.; Ninyerola, M.; Wardlow, B. Integration of climate time series and MODIS data as an analysis tool for forest drought detection. In *Drought: Research and science-policy interfacing Paredes-Arquiola, David Haro-Monteagudo, Henny van Lanen, 1st; Andreu, J., Solera, A., Paredes-Arquiola, J., Haro-Monteagudo, D., van Lanen, H.A.J., Eds.*; CRC Press: Boca Raton, 2015, ISBN 9781138027794.

- 
25. Dalezios, N.R. Drought and Remote Sensing. In *Remote Sensing of Hydrometeorological Hazards*, 1st ed.; Petropoulos, G.P., Islam, T., Eds.; CRC Press: Milton, 2017; pp 3–31, ISBN 9781498777582.
  26. Gao, S.; Liu, R.; Zhou, T.; Fang, W.; Yi, C.; Lu, R.; Zhao, X.; Luo, H. Dynamic responses of tree-ring growth to multiple dimensions of drought. *Glob. Chang. Biol.* **2018**, *24*, 5380–5390, doi:10.1111/gcb.14367.
  27. Jong, R. de; Schaepman, M.E.; Furrer, R.; Bruin, S. de; Verburg, P.H. Spatial relationship between climatologies and changes in global vegetation activity. *Glob. Chang. Biol.* **2013**, *19*, 1953–1964, doi:10.1111/gcb.12193.
  28. Tucker, C.J. Red and photographic infrared linear combinations for monitoring vegetation. *Remote Sensing of Environment* **1979**, *8*, 127–150, doi:10.1016/0034-4257(79)90013-0.
  29. Gao, B.-c. NDWI—A normalized difference water index for remote sensing of vegetation liquid water from space. *Remote Sensing of Environment* **1996**, *58*, 257–266, doi:10.1016/S0034-4257(96)00067-3.
  30. Xu, L.; Samanta, A.; Costa, M.H.; Ganguly, S.; Nemani, R.R.; Myneni, R.B. Widespread decline in greenness of Amazonian vegetation due to the 2010 drought. *Geophys. Res. Lett.* **2011**, *38*, n/a-n/a, doi:10.1029/2011GL046824.
  31. Atkinson, P.M.; Dash, J.; Jeganathan, C. Amazon vegetation greenness as measured by satellite sensors over the last decade. *Geophys. Res. Lett.* **2011**, *38*, n/a-n/a, doi:10.1029/2011GL049118.
  32. McDowell, N.; Pockman, W.T.; Allen, C.D.; Breshears, D.D.; Cobb, N.; Kolb, T.; Plaut, J.; Sperry, J.; West, A.; Williams, D.G.; et al. Mechanisms of plant survival and mortality during drought: why do some plants survive while others succumb to drought? *New Phytol.* **2008**, *178*, 719–739, doi:10.1111/j.1469-8137.2008.02436.x.
  33. Pasho, E.; Camarero, J.J.; Luis, M. de; Vicente-Serrano, S.M. Impacts of drought at different time scales on forest growth across a wide climatic gradient in north-eastern Spain. *Agricultural and Forest Meteorology* **2011**, *151*, 1800–1811, doi:10.1016/j.agrformet.2011.07.018.
  34. Vicente-Serrano, S.M.; Gouveia, C.; Camarero, J.J.; Beguería, S.; Trigo, R.; López-Moreno, J.I.; Azorín-Molina, C.; Pasho, E.; Lorenzo-Lacruz, J.; Revuelto, J.; et al. Response of vegetation to drought time-scales across global land biomes. *Proc. Natl. Acad. Sci. U. S. A.* **2013**, *110*, 52–57, doi:10.1073/pnas.1207068110.
  35. Flower, A.; Gavin, D.G.; Heyerdahl, E.K.; Parsons, R.A.; Cohn, G.M. Drought-triggered western spruce budworm outbreaks in the interior Pacific Northwest: A multi-century dendrochronological record. *Forest Ecology and Management* **2014**, *324*, 16–27, doi:10.1016/j.foreco.2014.03.042.
  36. Millar, C.I.; Stephenson, N.L. Temperate forest health in an era of emerging megadisturbance. *Science* **2015**, *349*, 823–826, doi:10.1126/science.aaa9933.
  37. Ward, S.F.; Aukema, B.H. Anomalous outbreaks of an invasive defoliator and native bark beetle facilitated by warm temperatures, changes in precipitation and interspecific interactions. *Ecography* **2019**, *31*, 348, doi:10.1111/ecog.04239.
  38. Bonan, G.B. Forests and climate change: forcings, feedbacks, and the climate benefits of forests. *Science* **2008**, *320*, 1444–1449, doi:10.1126/science.1155121.

39. Adams, H.D.; Guardiola-Claramonte, M.; Barron-Gafford, G.A.; Villegas, J.C.; Breshears, D.D.; Zou, C.B.; Troch, P.A.; Huxman, T.E. Temperature sensitivity of drought-induced tree mortality portends increased regional die-off under global-change-type drought. *Proc. Natl. Acad. Sci. U. S. A.* **2009**, *106*, 7063–7066, doi:10.1073/pnas.0901438106.
40. McDowell, N.G. Mechanisms linking drought, hydraulics, carbon metabolism, and vegetation mortality. *Plant Physiol.* **2011**, *155*, 1051–1059, doi:10.1104/pp.110.170704.
41. Luce, C.H.; Vose, J.M.; Pederson, N.; Campbell, J.; Millar, C.; Kormos, P.; Woods, R. Contributing factors for drought in United States forest ecosystems under projected future climates and their uncertainty. *Forest Ecology and Management* **2016**, *380*, 299–308, doi:10.1016/j.foreco.2016.05.020.
42. Galiano, L.; Timofeeva, G.; Saurer, M.; Siegwolf, R.; Martínez-Vilalta, J.; Hommel, R.; Gessler, A. The fate of recently fixed carbon after drought release: towards unravelling C storage regulation in *Tilia platyphyllos* and *Pinus sylvestris*. *Plant Cell Environ.* **2017**, *40*, 1711–1724, doi:10.1111/pce.12972.
43. Ciesla, W.M.; Donaubauer, E. *Decline and dieback of trees and forests: A global overview*; Food & Agriculture Org., 1994, ISBN 9251035024.
44. Allen, C.D.; Macalady, A.K.; Chenchouni, H.; Bachelet, D.; McDowell, N.; Vennetier, M.; Kitzberger, T.; Rigling, A.; Breshears, D.D.; Hogg, E.H.; et al. A global overview of drought and heat-induced tree mortality reveals emerging climate change risks for forests. *Forest Ecology and Management* **2010**, *259*, 660–684, doi:10.1016/j.foreco.2009.09.001.
45. Anderegg, W.R.L.; Kane, J.M.; Anderegg, L.D.L. Consequences of widespread tree mortality triggered by drought and temperature stress. *Nature Clim Change* **2013**, *3*, 30–36, doi:10.1038/nclimate1635.
46. Choat, B.; Jansen, S.; Brodribb, T.J.; Cochard, H.; Delzon, S.; Bhaskar, R.; Bucci, S.J.; Feild, T.S.; Gleason, S.M.; Hacke, U.G.; et al. Global convergence in the vulnerability of forests to drought. *Nature* **2012**, *491*, 752–755, doi:10.1038/nature11688.
47. Saatchi, S.; Asefi-Najafabady, S.; Malhi, Y.; Aragão, L.E.O.C.; Anderson, L.O.; Myneni, R.B.; Nemani, R. Persistent effects of a severe drought on Amazonian forest canopy. *Proc. Natl. Acad. Sci. U. S. A.* **2013**, *110*, 565–570, doi:10.1073/pnas.1204651110.
48. Bradford, J.B.; Bell, D.M. A window of opportunity for climate-change adaptation: easing tree mortality by reducing forest basal area. *Front Ecol Environ* **2017**, *15*, 11–17, doi:10.1002/fee.1445.
49. Paradis, A.; Elkinton, J.; Hayhoe, K.; Buonaccorsi, J. Role of winter temperature and climate change on the survival and future range expansion of the hemlock woolly adelgid (*Adelges tsugae*) in eastern North America. *Mitig Adapt Strateg Glob Change* **2008**, *13*, 541–554, doi:10.1007/s11027-007-9127-0.
50. Trần, J.K.; Ylioja, T.; Billings, R.F.; Régnière, J.; Ayres, M.P. Impact of minimum winter temperatures on the population dynamics of *Dendroctonus frontalis*. *Ecological Applications* **2007**, *17*, 882–899, doi:10.1890/06-0512.
51. Pureswaran, D.S.; Roques, A.; Battisti, A. Forest Insects and Climate Change. *Curr Forestry Rep* **2018**, *4*, 35–50, doi:10.1007/s40725-018-0075-6.

- 
52. Kolb, T.E.; Fettig, C.J.; Ayres, M.P.; Bentz, B.J.; Hicke, J.A.; Mathiasen, R.; Stewart, J.E.; Weed, A.S. Observed and anticipated impacts of drought on forest insects and diseases in the United States. *Forest Ecology and Management* **2016**, *380*, 321–334, doi:10.1016/j.foreco.2016.04.051.
  53. Kulakowski, D.; Jarvis, D. Low-severity fires increase susceptibility of lodgepole pine to mountain pine beetle outbreaks in Colorado. *Forest Ecology and Management* **2013**, *289*, 544–550, doi:10.1016/j.foreco.2012.10.020.
  54. McCarley, T.R.; Kolden, C.A.; Vaillant, N.M.; Hudak, A.T.; Smith, A.M.S.; Kreidler, J. Landscape-scale quantification of fire-induced change in canopy cover following mountain pine beetle outbreak and timber harvest. *Forest Ecology and Management* **2017**, *391*, 164–175, doi:10.1016/j.foreco.2017.02.015.
  55. Hicke, J.A.; Johnson, M.C.; Hayes, J.L.; Preisler, H.K. Effects of bark beetle-caused tree mortality on wildfire. *Forest Ecology and Management* **2012**, *271*, 81–90, doi:10.1016/j.foreco.2012.02.005.
  56. Chen, G.; He, Y.; Santis, A. de; Li, G.; Cobb, R.; Meentemeyer, R.K. Assessing the impact of emerging forest disease on wildfire using Landsat and KOMPSAT-2 data. *Remote Sensing of Environment* **2017**, *195*, 218–229, doi:10.1016/j.rse.2017.04.005.
  57. Agne, M.C.; Woolley, T.; Fitzgerald, S. Fire severity and cumulative disturbance effects in the post-mountain pine beetle lodgepole pine forests of the Pole Creek Fire. *Forest Ecology and Management* **2016**, *366*, 73–86, doi:10.1016/j.foreco.2016.02.004.
  58. Meigs, G.W.; Campbell, J.L.; Zald, H.S.J.; Bailey, J. d.; Shaw, D.C.; Kennedy, R.E. Does wildfire likelihood increase following insect outbreaks in conifer forests? *Ecosphere* **2015**, *6*, art118, doi:10.1890/ES15-00037.1.
  59. Kane, J.M.; Varner, J.M.; Metz, M.R.; van Mantgem, P.J. Characterizing interactions between fire and other disturbances and their impacts on tree mortality in western U.S. Forests. *Forest Ecology and Management* **2017**, *405*, 188–199, doi:10.1016/j.foreco.2017.09.037.
  60. Ahern, F.J. The effects of bark beetle stress on the foliar spectral reflectance of lodgepole pine. *International Journal of Remote Sensing* **1988**, *9*, 1451–1468, doi:10.1080/01431168808954952.
  61. Carter, G.A. Responses of leaf spectral reflectance to plant stress. *American Journal of Botany* **1993**, *80*, 239–243, doi:10.1002/j.1537-2197.1993.tb13796.x.
  62. Carter, G.A.; Knapp, A.K. Leaf optical properties in higher plants: linking spectral characteristics to stress and chlorophyll concentration. *Am. J. Bot.* **2001**, *88*, 677–684, doi:10.2307/2657068.
  63. Rullán-Silva, C.; Olthoff, A.E.; Pando, V.; Pajares, J.A.; Delgado, J.A. Remote monitoring of defoliation by the beech leaf-mining weevil *Rhynchaenus fagi* in northern Spain. *Forest Ecology and Management* **2015**, *347*, 200–208, doi:10.1016/j.foreco.2015.03.005.
  64. Townsend, P.A.; Singh, A.; Foster, J.R.; Rehberg, N.J.; Kingdon, C.C.; Eshleman, K.N.; Seagle, S.W. A general Landsat model to predict canopy defoliation in broadleaf deciduous forests. *Remote Sensing of Environment* **2012**, *119*, 255–265, doi:10.1016/j.rse.2011.12.023.
  65. Hashimoto, H.; Nemani, R.R.; White, M.A.; Jolly, W.M.; Piper, S.C.; Keeling, C.D.; Myneni, R.B.; Running, S.W. El Niño-Southern Oscillation-induced variability in terrestrial carbon cycling. *J. Geophys. Res.* **2004**, *109*, 116, doi:10.1029/2004JD004959.

66. Breshears, D.D.; Cobb, N.S.; Rich, P.M.; Price, K.P.; Allen, C.D.; Balice, R.G.; Romme, W.H.; Kastens, J.H.; Floyd, M.L.; Belnap, J.; et al. Regional vegetation die-off in response to global-change-type drought. *Proc. Natl. Acad. Sci. U. S. A.* **2005**, *102*, 15144–15148, doi:10.1073/pnas.0505734102.
67. Camarero, J.J.; Gazol, A.; Sangüesa-Barreda, G.; Oliva, J.; Vicente-Serrano, S.M. To die or not to die: early warnings of tree dieback in response to a severe drought. *J Ecol* **2015**, *103*, 44–57, doi:10.1111/1365-2745.12295.
68. Stimson, H.C.; Breshears, D.D.; Ustin, S.L.; Kefauver, S.C. Spectral sensing of foliar water conditions in two co-occurring conifer species: *Pinus edulis* and *Juniperus monosperma*. *Remote Sensing of Environment* **2005**, *96*, 108–118, doi:10.1016/j.rse.2004.12.007.
69. Verbesselt, J.; Robinson, A.; Stone, C.; Culvenor, D. Forecasting tree mortality using change metrics derived from MODIS satellite data. *Forest Ecology and Management* **2009**, *258*, 1166–1173, doi:10.1016/j.foreco.2009.06.011.
70. Byer, S.; Jin, Y. Detecting Drought-Induced Tree Mortality in Sierra Nevada Forests with Time Series of Satellite Data. *Remote Sensing* **2017**, *9*, 929, doi:10.3390/rs9090929.
71. Wu, D.; Zhao, X.; Liang, S.; Zhou, T.; Huang, K.; Tang, B.; Zhao, W. Time-lag effects of global vegetation responses to climate change. *Glob. Chang. Biol.* **2015**, *21*, 3520–3531, doi:10.1111/gcb.12945.
72. Andujar, E.; Krakauer, N.Y.; Yi, C.; Kogan, F. Ecosystem Drought Response Timescales from Thermal Emission versus Shortwave Remote Sensing. *Advances in Meteorology* **2017**, *2017*, 1–10, doi:10.1155/2017/8434020.
73. Anselin, L. *Modern spatial econometrics in practice. A guide to GeoDa, GeoDaSpace and PySAL*; GeoDa Press, 2014, ISBN 0986342106.
74. Fotheringham, A.S.; Brunson, C.; Charlton, M. *Geographically weighted regression. The analysis of spatially varying relationships*, 1st edn.; John Wiley & Sons Ltd.: West Sussex, England, 2002, ISBN 978-0-471-49616-8.
75. Adelabu, S.; Mutanga, O.; Adam, E. Evaluating the impact of red-edge band from Rapideye image for classifying insect defoliation levels. *ISPRS Journal of Photogrammetry and Remote Sensing* **2014**, *95*, 34–41, doi:10.1016/j.isprsjprs.2014.05.013.
76. Dash, J.P.; Watt, M.S.; Pearse, G. d.; Heaphy, M.; Dungey, H.S. Assessing very high resolution UAV imagery for monitoring forest health during a simulated disease outbreak. *ISPRS Journal of Photogrammetry and Remote Sensing* **2017**, *131*, 1–14, doi:10.1016/j.isprsjprs.2017.07.007.
77. Friedman, J.H. Stochastic gradient boosting. *Computational Statistics & Data Analysis* **2002**, *38*, 367–378, doi:10.1016/S0167-9473(01)00065-2.
78. Hastie, Robert Tibshirani, and Jerome Friedman. The elements of statistical learning: data mining, inference and prediction. *The Mathematical Intelligencer* **2005**, *27*, 83–85, doi:10.1007/BF02985802.
79. Hay, G.J.; Castilla, G. Geographic Object-Based Image Analysis (GEOBIA): A new name for a new discipline. In *Object-based image analysis: Spatial concepts for knowledge-driven remote sensing applications / edited by Thomas Blaschke, Stefan Lang, Geoffrey Hay*; Blaschke, T., Lang, S., Hay, G.J., Eds.; Springer: Berlin, Germany, London, UK, 2008; pp 75–89, ISBN 978-3-540-77057-2.

- 
80. UNESCO. World Heritage: Hyrcanian Forests. <https://whc.unesco.org/en/list/1584/> (accessed on 10/26/2019).
  81. Akhani, H.; Djamali, M.; Ghorbanalizadeh, A.; Ramezani, E. Plant biodiversity of Hyrcanian relict forests, N Iran: an overview of the flora, vegetation, palaeoecology and conservation **2010**, *42*, 231–258.
  82. Sagheb Talebi, K.; Sajedi, T.; Pourhashemi, M. *Forests of Iran. A Treasure from the Past, a Hope for the Future*; Springer Netherlands; Imprint; Springer: Dordrecht, 2014, ISBN 978-94-007-7371-4.
  83. Shirvani, Z.; Abdi, O.; Buchroithner, M.F.; Pradhan, B. Analysing Spatial and Statistical Dependencies of Deforestation Affected by Residential Growth: Gorganrood Basin, Northeast Iran. *Land Degrad. Develop.* **2017**, *28*, 2176–2190, doi:10.1002/ldr.2744.
  84. Abdi, O.; Kamkar, B.; Shirvani, Z.; Teixeira da Silva, J.A.; Buchroithner, M.F. Spatial-statistical analysis of factors determining forest fires: a case study from Golestan, Northeast Iran. *Geomatics, Natural Hazards and Risk* **2018**, *9*, 267–280, doi:10.1080/19475705.2016.1206629.
  85. Kia-Daliri, H.; Kazemi-Najafi, S.; Ahangaran, Y. The effect of leaf feeder moth (*Erannis defoliaria* & *Operophtera brumata*) on radial growth of 3 tree species in north of Iran (case study: Mashalak, Nowshahr). *Iranian Journal of Forest and Poplar Research* **2007**, *15*, 301–309.
  86. Ahmadi, A.; Kavosi, M.R.; Soltanloo, H. Zelkova carpinifolia reservoir from Hyrcanian Forests, Northern Iran, a new sacrifice of *Ophiostoma novo-ulmi*. *Biodiversitas* **2014**, *15*, 48–52, doi:10.13057/biodiv/d150107.
  87. Mirabolfathy, M.; Groenewald, J.Z.; Crous, P.W. The Occurrence of Charcoal Disease Caused by *Biscogniauxia mediterranea* on Chestnut-Leaved Oak (*Quercus castaneifolia*) in the Golestan Forests of Iran. *Plant Dis.* **2011**, *95*, 876, doi:10.1094/PDIS-03-11-0153.
  88. Alkhatib, A.A.A. A Review on Forest Fire Detection Techniques. *International Journal of Distributed Sensor Networks* **2014**, *10*, 597368, doi:10.1155/2014/597368.
  89. Abdi, O.; Shetaee, S.H.; Shirvani, Z.; Naghavi, M.R. Forest management impacts on forest fires in Golestan province by GIS application. *Iranian Journal of Forest and Range Protection Research* **2012**, *9*, 100–108.
  90. Eskandari, S. Investigation on the relationship between climate change and fire in the forests of Golestan Province. *Iranian Journal of Forest and Range Protection Research* **2015**, *13*, 1–10.
  91. Pew, K.L.; Larsen, C.P.S. GIS analysis of spatial and temporal patterns of human-caused wildfires in the temperate rain forest of Vancouver Island, Canada. *Forest Ecology and Management* **2001**, *140*, 1–18, doi:10.1016/S0378-1127(00)00271-1.
  92. Bonazountas, M.; Kallidromitou, D.; Kassomenos, P.; Passas, N. A decision support system for managing forest fire casualties. *J. Environ. Manage.* **2007**, *84*, 412–418, doi:10.1016/j.jenvman.2006.06.016.
  93. Duane, A.; Piqué, M.; Castellnou, M.; Brotons, L. Predictive modelling of fire occurrences from different fire spread patterns in Mediterranean landscapes. *Int. J. Wildland Fire* **2015**, *24*, 407, doi:10.1071/WF14040.

94. Cardille, J.A.; Ventura, S.J.; Turner, M.G. Environmental and social factors influencing wildfires in the Upper Midwest, United States. *Ecological Applications* **2001**, *11*, 111–127, doi:10.1890/1051-0761(2001)011[0111:EASFIW]2.0.CO;2.
95. Dickson, B.G.; Prather, J.W.; Xu, Y.; Hampton, H.M.; Aumack, E.N.; Sisk, T. d. Mapping the probability of large fire occurrence in northern Arizona, USA. *Landscape Ecol* **2006**, *21*, 747–761, doi:10.1007/s10980-005-5475-x.
96. Syphard, A. d.; Radeloff, V.C.; Keuler, N.S.; Taylor, R.S.; Hawbaker, T.J.; Stewart, S.I.; Clayton, M.K. Predicting spatial patterns of fire on a southern California landscape. *Int. J. Wildland Fire* **2008**, *17*, 602, doi:10.1071/WF07087.
97. Alvarez, A.; Gracia, M.; Castellnou, M.; Retana, J. Variables That Influence Changes in Fire Severity and Their Relationship with Changes Between Surface and Crown Fires in a Wind-Driven Wildfire. *Forest Science* **2013**, *59*, 139–150, doi:10.5849/forsci.10-140.
98. Jung, J.; Kim, C.; Jayakumar, S.; Kim, S.; Han, S.; Kim, D.H.; Heo, J. Forest fire risk mapping of Kolli Hills, India, considering subjectivity and inconsistency issues. *Nat Hazards* **2013**, *65*, 2129–2146, doi:10.1007/s11069-012-0465-1.
99. Zarekar, A.; Vahidi, H.; Kazemi, B.; Ghorbani, Z.S.; Jafari, H. Forest fire hazard mapping using fuzzy Ahp and GIS study area: Gilan Province of Iran. *International Journal on "Technical and Physical Problems of Engineering" (IJTPE)* **2012**, *4*, 47–55.
100. Beverly, J.L.; Herd, E.P.K.; Conner, J.R. Modeling fire susceptibility in west central Alberta, Canada. *Forest Ecology and Management* **2009**, *258*, 1465–1478, doi:10.1016/j.foreco.2009.06.052.
101. Oliveira, S.; Oehler, F.; San-Miguel-Ayanz, J.; Camia, A.; Pereira, J.M.C. Modeling spatial patterns of fire occurrence in Mediterranean Europe using Multiple Regression and Random Forest. *Forest Ecology and Management* **2012**, *275*, 117–129, doi:10.1016/j.foreco.2012.03.003.
102. Chou, Y.H.; Minnich, R.A.; Chase, R.A. Mapping probability of fire occurrence in San Jacinto Mountains, California, USA. *Environmental Management* **1993**, *17*, 129–140, doi:10.1007/BF02393801.
103. Garcia, C.V.; Woodard, P.M.; Titus, S.J.; Adamowicz, W.L.; Lee, B.S. A Logit Model for Predicting the Daily Occurrence of Human Caused Forest-Fires. *Int. J. Wildland Fire* **1995**, *5*, 101, doi:10.1071/WF9950101.
104. Mohammadi, F.; Bavaghar, M.P.; Shabaniyan, N. Forest Fire Risk Zone Modeling Using Logistic Regression and GIS: An Iranian Case Study. *Small-scale Forestry* **2013**, *13*, 117–125, doi:10.1007/s11842-013-9244-4.
105. Sakr, G.E.; Elhajj, I.H.; Mitri, G. Efficient forest fire occurrence prediction for developing countries using two weather parameters. *Engineering Applications of Artificial Intelligence* **2011**, *24*, 888–894, doi:10.1016/j.engappai.2011.02.017.
106. Núñez-Regueira, L.; Rodríguez Añón, J.A.; Proupín Castiñeiras, J. Design of risk index maps as a tool to prevent forest fires. *Bioresource Technology* **2000**, *71*, 51–62, doi:10.1016/S0960-8524(99)00052-8.
107. La Riva, J. de; Pérez-Cabello, F.; Lana-Renault, N.; Koutsias, N. Mapping wildfire occurrence at regional scale. *Remote Sensing of Environment* **2004**, *92*, 288–294, doi:10.1016/j.rse.2004.06.013.



- 
108. Haight, R.G.; Cleland, D.T.; Hammer, R.B.; Radeloff, V.C.; Rupp, T.S. Assessing fire risk in the wildland-urban interface **2004**, *102*, 41–48.
  109. Arkle, R.S.; Pilliod, D.S.; Welty, J.L. Pattern and process of prescribed fires influence effectiveness at reducing wildfire severity in dry coniferous forests. *Forest Ecology and Management* **2012**, *276*, 174–184, doi:10.1016/j.foreco.2012.04.002.
  110. Jaiswal, R.K.; Mukherjee, S.; Raju, K. d.; Saxena, R. Forest fire risk zone mapping from satellite imagery and GIS. *International Journal of Applied Earth Observation and Geoinformation* **2002**, *4*, 1–10, doi:10.1016/S0303-2434(02)00006-5.
  111. Dong, X.; Li-min, D.; Guo-fan, S.; Lei, T.; Hui, W. Forest fire risk zone mapping from satellite images and GIS for Baihe Forestry Bureau, Jilin, China. *Journal of Forestry Research* **2005**, *16*, 169–174, doi:10.1007/BF02856809.
  112. Portillo-Quintero, C.; Sanchez-Azofeifa, A.; Marcos do Espirito-Santo, M. Monitoring deforestation with MODIS Active Fires in Neotropical dry forests: An analysis of local-scale assessments in Mexico, Brazil and Bolivia. *Journal of Arid Environments* **2013**, *97*, 150–159, doi:10.1016/j.jaridenv.2013.06.002.
  113. Zhang, Z.X.; Zhang, H.Y.; Zhou, D.W. Using GIS spatial analysis and logistic regression to predict the probabilities of human-caused grassland fires. *Journal of Arid Environments* **2010**, *74*, 386–393, doi:10.1016/j.jaridenv.2009.09.024.
  114. Mozaffarian, V. *Dictionary of Iranian plant names Latin–English–Persian*, 5th ed.; Farhang Moaser: Tehran, 2007, ISBN 978-964-5545-40-4.
  115. Jensen, J.R. *Introductory digital image processing. A remote sensing perspective* / John R. Jensen, 3rd ed.; Prentice Hall: Upper Saddle River, N.J., 2005, ISBN 9780131453616.
  116. Raafatnia, N.A. *Forest and mountain roads (design and project)*, 1st ed.; University of Mazandaran: Babolsar, 1989.
  117. Rezai, A. *Concepts of probability and statistics*, 7th ed.; Mashhad: Mashhad, 2009, ISBN 9789646157125.
  118. FAO. *International handbook on forest fire protection. Technical guide for the countries of the Mediterranean basin*, 2001. [www.fao.org/forestry/27221-06293a5348df37bc8b14e24472df64810.pdf](http://www.fao.org/forestry/27221-06293a5348df37bc8b14e24472df64810.pdf) (accessed on 17 January 2016).
  119. Schoennagel, T.; Veblen, T.T.; Romme, W.H. The Interaction of Fire, Fuels, and Climate across Rocky Mountain Forests. *Ecological Applications* **2004**, *54*, 661, doi:10.1641/0006-3568(2004)054[0661:TIOFFA]2.0.CO;2.
  120. FAO. Fire management global assessment 2006. <http://www.fao.org/3/a0969e/a0969e00.htm> (accessed on 17 January 2016).
  121. Aldersley, A.; Murray, S.J.; Cornell, S.E. Global and regional analysis of climate and human drivers of wildfire. *Sci. Total Environ.* **2011**, *409*, 3472–3481, doi:10.1016/j.scitotenv.2011.05.032.
  122. Ireland, K.B.; Stan, A.B.; Fulé, P.Z. Bottom-up control of a northern Arizona ponderosa pine forest fire regime in a fragmented landscape. *Landscape Ecol* **2012**, *27*, 983–997, doi:10.1007/s10980-012-9753-0.

123. Alvarez, A.; Gracia, M.; Vayreda, J.; Retana, J. Patterns of fuel types and crown fire potential in *Pinus halepensis* forests in the Western Mediterranean Basin. *Forest Ecology and Management* **2012**, *270*, 282–290, doi:10.1016/j.foreco.2011.01.039.
124. Lecina-Diaz, J.; Alvarez, A.; Retana, J. Extreme fire severity patterns in topographic, convective and wind-driven historical wildfires of Mediterranean pine forests. *PLoS ONE* **2014**, *9*, e85127, doi:10.1371/journal.pone.0085127.
125. Alexander, J. d.; Seavy, N.E.; Ralph, C.J.; Hogoboom, B. Vegetation and topographical correlates of fire severity from two fires in the Klamath-Siskiyou region of Oregon and California. *Int. J. Wildland Fire* **2006**, *15*, 237, doi:10.1071/WF05053.
126. Lentile, L.B.; Smith, F.W.; Shepperd, W.D. Influence of topography and forest structure on patterns of mixed severity fire in ponderosa pine forests of the South Dakota Black Hills, USA. *Int. J. Wildland Fire* **2006**, *15*, 557, doi:10.1071/WF05096.
127. Lee, B.; Kim, S.Y.; Chung, J.; Park, P.S. Estimation of fire severity by use of Landsat TM images and its relevance to vegetation and topography in the 2000 Samcheok forest fire. *Journal of Forest Research* **2008**, *13*, 197–204, doi:10.1007/s10310-008-0072-x.
128. Holden, Z.A.; Morgan, P.; Evans, J.S. A predictive model of burn severity based on 20-year satellite-inferred burn severity data in a large southwestern US wilderness area. *Forest Ecology and Management* **2009**, *258*, 2399–2406, doi:10.1016/j.foreco.2009.08.017.
129. Price, O.F.; Bradstock, R.A. The effect of fuel age on the spread of fire in sclerophyll forest in the Sydney region of Australia. *Int. J. Wildland Fire* **2010**, *19*, 35, doi:10.1071/WF08167.
130. Narayanaraj, G.; Wimberly, M.C. Influences of forest roads on the spatial patterns of human- and lightning-caused wildfire ignitions. *Applied Geography* **2012**, *32*, 878–888, doi:10.1016/j.apgeog.2011.09.004.
131. Hann, W.; Jones, J.; Karl, M.; et al. Landscape dynamics of the basin. In *An assessment of ecosystem components in the interior Columbia basin and portions of the Klamath and Great Basins: volume 2*; Quigley, T.M., Arbelbide, S.J., Eds.; pp 337–1055.
132. Narayanaraj, G.; Wimberly, M.C. Influences of forest roads on the spatial pattern of wildfire boundaries. *Int. J. Wildland Fire* **2011**, *20*, 792, doi:10.1071/WF10032.
133. Yang, J.; He, H.S.; Shifley, S.R. Spatial controls of occurrence and spread of wildfires in the Missouri Ozark Highlands. *Ecological Applications* **2008**, *18*, 1212–1225, doi:10.1890/07-0825.1.
134. Jacob, A.L.; Wilson, S.J.; Lewis, S.L. Ecosystem services: Forests are more than sticks of carbon. *Nature* **2014**, *507*, 306, doi:10.1038/507306c.
135. Madani, K.; AghaKouchak, A.; Mirchi, A. Iran's Socio-economic Drought: Challenges of a Water-Bankrupt Nation. *Iranian Studies* **2016**, *49*, 997–1016, doi:10.1080/00210862.2016.1259286.
136. Bari Abarghouei, H.; Asadi Zarch, M.A.; Dastorani, M.T.; Kousari, M.R.; Safari Zarch, M. The survey of climatic drought trend in Iran. *Stoch Environ Res Risk Assess* **2011**, *25*, 851–863, doi:10.1007/s00477-011-0491-7.
137. Shahabfar, A.; Eitzinger, J. Spatio-Temporal Analysis of Droughts in Semi-Arid Regions by Using Meteorological Drought Indices. *Atmosphere* **2013**, *4*, 94–112, doi:10.3390/atmos4020094.

- 
138. Dashtpajardi, M.M.; Kousari, M.R.; Vagharfard, H.; Ghonchehpour, D.; Hosseini, M.E.; Ahani, H. An investigation of drought magnitude trend during 1975–2005 in arid and semi-arid regions of Iran. *Environ Earth Sci* **2015**, *73*, 1231–1244, doi:10.1007/s12665-014-3477-1.
139. Kazemzadeh, M.; Malekian, A. Spatial characteristics and temporal trends of meteorological and hydrological droughts in northwestern Iran. *Nat Hazards* **2016**, *80*, 191–210, doi:10.1007/s11069-015-1964-7.
140. Ghaffari, A. *A review of drought impacts on rainfed field crops and horticulture crops (vegetables and orchards) and of their socioeconomic consequences on the farming communities; and analysis of the policies aimed at rehabilitation of the sector* National consultancy under TCP/IRA/3003, 2006.
141. Golian, S.; Mazdiyasni, O.; AghaKouchak, A. Trends in meteorological and agricultural droughts in Iran. *Theor Appl Climatol* **2015**, *119*, 679–688, doi:10.1007/s00704-014-1139-6.
142. Adab, H.; Kanniah, K.D.; Solaimani, K.; Sallehuddin, R. Modelling static fire hazard in a semi-arid region using frequency analysis. *Int. J. Wildland Fire* **2015**, *24*, 763, doi:10.1071/WF13113.
143. Zoljoodi, M.; Didevarasl, A. Evaluation of Spatial-Temporal Variability of Drought Events in Iran Using Palmer Drought Severity Index and Its Principal Factors (through 1951–2005). *ACS* **2013**, *03*, 193–207, doi:10.4236/acs.2013.32021.
144. Asner, G.P.; Alencar, A. Drought impacts on the Amazon forest: the remote sensing perspective. *New Phytol.* **2010**, *187*, 569–578, doi:10.1111/j.1469-8137.2010.03310.x.
145. McDowell, N.G.; Coops, N.C.; Beck, P.S.A.; Chambers, J.Q.; Gangodagamage, C.; Hicke, J.A.; Huang, C.-y.; Kennedy, R.; Krofcheck, D.J.; Litvak, M.; et al. Global satellite monitoring of climate-induced vegetation disturbances. *Trends Plant Sci.* **2015**, *20*, 114–123, doi:10.1016/j.tplants.2014.10.008.
146. Ogaya, R.; Barbeta, A.; Bařnou, C.; Peñuelas, J. Satellite data as indicators of tree biomass growth and forest dieback in a Mediterranean holm oak forest. *Annals of Forest Science* **2015**, *72*, 135–144, doi:10.1007/s13595-014-0408-y.
147. Ji, L.; Peters, A.J. Assessing vegetation response to drought in the northern Great Plains using vegetation and drought indices. *Remote Sensing of Environment* **2003**, *87*, 85–98, doi:10.1016/S0034-4257(03)00174-3.
148. Jong, R. de; Bruin, S. de; Wit, A. de; Schaepman, M.E.; Dent, D.L. Analysis of monotonic greening and browning trends from global NDVI time-series. *Remote Sensing of Environment* **2011**, *115*, 692–702, doi:10.1016/j.rse.2010.10.011.
149. Tadesse, T.; Demisse, G.B.; Zaitchik, B.; Dinku, T. Satellite-based hybrid drought monitoring tool for prediction of vegetation condition in Eastern Africa: A case study for Ethiopia. *Water Resour. Res.* **2014**, *50*, 2176–2190, doi:10.1002/2013WR014281.
150. Justice, C.O.; Giglio, L.; Korontzi, S.; Owens, J.; Morisette, J.T.; Roy, D.; Descloitres, J.; Alleaume, S.; Petitcolin, F.; Kaufman, Y. The MODIS fire products. *Remote Sensing of Environment* **2002**, *83*, 244–262, doi:10.1016/S0034-4257(02)00076-7.
151. Wardlow, B.; Anderson, M.; Tadesse, C.; Hain, W.; Rodell, M.; Thenkabail, P.S. Remote sensing of drought: Emergence of a satellite-based monitoring toolkit for the United States. In *Remote*

- sensing of water resources, disasters, and urban studies*, 1st; Thenkabail, P.S., Ed.; CRC Press: Boca Raton, 2015; pp 367–400, ISBN 9781482217919.
152. Anderson, L.O.; Malhi, Y.; Aragão, L.E.O.C.; Ladle, R.; Arai, E.; Barbier, N.; Phillips, O. Remote sensing detection of droughts in Amazonian forest canopies. *New Phytol.* **2010**, *187*, 733–750.
  153. Brando, P.M.; Goetz, S.J.; Baccini, A.; Nepstad, D.C.; Beck, P.S.A.; Christman, M.C. Seasonal and interannual variability of climate and vegetation indices across the Amazon. *Proc. Natl. Acad. Sci. U. S. A.* **2010**, *107*, 14685–14690, doi:10.1073/pnas.0908741107.
  154. Domingo, C.; Pons, X.; Cristóbal, J.; Ninyerola, M.; Wardlow, B. Integration of climate time series and MODIS data as an analysis tool for forest drought detection. In *Drought: Research and science-policy interfacing Paredes-Arquiola, David Haro-Monteagudo, Henny van Lanen*, 1st; Andreu, J., Solera, A., Paredes-Arquiola, J., Haro-Monteagudo, D., van Lanen, H.A.J., Eds.; CRC Press: Boca Raton, 2015, ISBN 9781138027794.
  155. Rimkus, E.; Stonevicius, E.; Kilpys, J.; Maciulyte, V.; Valiukas, D. Drought identification in the eastern Baltic region using NDVI. *Earth Syst. Dynam.* **2017**, *8*, 627–637, doi:10.5194/esd-8-627-2017.
  156. Gu, Y.; Brown, J.F.; Verdin, J.P.; Wardlow, B. A five-year analysis of MODIS NDVI and NDWI for grassland drought assessment over the central Great Plains of the United States. *Geophys. Res. Lett.* **2007**, *34*, 1225, doi:10.1029/2006GL029127.
  157. van Niel, T.G.; McVicar, T.R.; Fang, H.; Liang, S. Calculating environmental moisture for per-field discrimination of rice crops. *International Journal of Remote Sensing* **2003**, *24*, 885–890, doi:10.1080/0143116021000009921.
  158. Solano, R.; Didan, K.; Jacobson, A.; Huete, A. MODIS Vegetation Indices (MOD13) C5 User's Guide. <https://www.ctahr.hawaii.edu/grem/mod13ug/> (accessed on 2 December 2017).
  159. Samanta, A.; Ganguly, S.; Hashimoto, H.; Devadiga, S.; Vermote, E.; Knyazikhin, Y.; Nemani, R.R.; Myneni, R.B. Amazon forests did not green-up during the 2005 drought. *Geophys. Res. Lett.* **2010**, *37*, n/a-n/a, doi:10.1029/2009GL042154.
  160. Asner, G.P.; Nepstad, D.; Cardinot, G.; Ray, D. Drought stress and carbon uptake in an Amazon forest measured with spaceborne imaging spectroscopy. *Proc. Natl. Acad. Sci. U. S. A.* **2004**, *101*, 6039–6044, doi:10.1073/pnas.0400168101.
  161. Doughty, C.E.; Goulden, M.L. Seasonal patterns of tropical forest leaf area index and CO<sub>2</sub> exchange. *J. Geophys. Res.* **2008**, *113*, n/a-n/a, doi:10.1029/2007JG000590.
  162. Zhao, X.; Wei, H.; Liang, S.; Zhou, T.; He, B.; Tang, B.; Wu, D. Responses of Natural Vegetation to Different Stages of Extreme Drought during 2009–2010 in Southwestern China. *Remote Sensing* **2015**, *7*, 14039–14054, doi:10.3390/rs71014039.
  163. Caccamo, G.; Chisholm, L.A.; Bradstock, R.A.; Puotinen, M.L. Assessing the sensitivity of MODIS to monitor drought in high biomass ecosystems. *Remote Sensing of Environment* **2011**, *115*, 2626–2639, doi:10.1016/j.rse.2011.05.018.
  164. Sagheb-Talebi, K.; Sajedi, T.; Pourhashemi, M. *Forests of Iran. A treasure from the past, a hope for the future* / Khosro Sagheb Talebi, Toktam Sajedi, Mehdi Pourhashemi; Springer: Dordrecht, 2014, ISBN 9789400773714.

- 
165. Rahmati, O.; Haghizadeh, A.; Stefanidis, S. Assessing the Accuracy of GIS-Based Analytical Hierarchy Process for Watershed Prioritization; Gorganrood River Basin, Iran. *Water Resour Manage* **2016**, *30*, 1131–1150, doi:10.1007/s11269-015-1215-4.
166. Huete, A.; Didan, K.; Miura, T.; Rodriguez, E.P.; Gao, X.; Ferreira, L.G. Overview of the radiometric and biophysical performance of the MODIS vegetation indices. *Remote Sensing of Environment* **2002**, *83*, 195–213, doi:10.1016/S0034-4257(02)00096-2.
167. Oyana, T.J.; Margai, F.M. *Spatial analysis. Statistics, visualization, and computational methods* / Tonny J. Oyana, Florence Margai, 1st; CRC Press: Boca Raton, 2015, ISBN 9781498707633.
168. Lark, R.M. Estimating variograms of soil properties by the method-of-moments and maximum likelihood. *European Journal of Soil Science* **2000**, *51*, 717–728, doi:10.1046/j.1365-2389.2000.00345.x.
169. Deutsch, C.V.; Journel, A.G. *GSLIB. Geostatistical Software Library and user's guide* / Clayton V. Deutsch, André G. Journel, 2nd ed.; Oxford University Press: New York, Oxford, 1998, ISBN 0195100158.
170. Krivoruchko, K. Empirical Bayesian Kriging: Implemented in ArcGIS Geostatistical Analyst. <https://www.esri.com/news/arcuser/1012/empirical-byesian-kriging.html> (accessed on 8 December 2017).
171. Xie, Y.; Chen, T.-b.; Lei, M.; Yang, J.; Guo, Q.-j.; Song, B.; Zhou, X.-y. Spatial distribution of soil heavy metal pollution estimated by different interpolation methods: accuracy and uncertainty analysis. *Chemosphere* **2011**, *82*, 468–476, doi:10.1016/j.chemosphere.2010.09.053.
172. Webster, R.; Oliver, M.A. *Geostatistics for environmental scientists*, 2nd ed.; Wiley: Chichester, 2007, ISBN 0470028580.
173. Hussain, M.; Chen, D.; Cheng, A.; Wei, H.; Stanley, D. Change detection from remotely sensed images: From pixel-based to object-based approaches. *ISPRS Journal of Photogrammetry and Remote Sensing* **2013**, *80*, 91–106, doi:10.1016/j.isprsjprs.2013.03.006.
174. McKee, T.B.; Doesken, N.J.; Kleist, J. The relationship of drought frequency and duration to time scales. In *Proceedings of the 8th Conference on Applied Climatology*; American Meteorological Society: Boston, MA, 1993; pp 179–183.
175. Tadesse, T.; Wardlow, B.D.; Hayes, M.J.; Svoboda, M.D.; Brown, J.F. The Vegetation Outlook (VegOut): A New Method for Predicting Vegetation Seasonal Greenness. *GIScience & Remote Sensing* **2010**, *47*, 25–52, doi:10.2747/1548-1603.47.1.25.
176. Lloyd, C.D. *Local models for spatial analysis*, 2nd ed.; CRC Press: Boca Raton, Fla., 2011, ISBN 1439829195.
177. Lee, S.-I. Developing a bivariate spatial association measure: An integration of Pearson's r and Moran's I. *Journal of Geographical Systems* **2001**, *3*, 369–385, doi:10.1007/s101090100064.
178. Getis, A. Cliff, A.D. and Ord, J.K. 1973: Spatial autocorrelation. London: Pion. *Progress in Human Geography* **1995**, *19*, 245–249, doi:10.1177/030913259501900205.
179. Anselin, L.; Rey, S.J. *Modern spatial econometrics in practice. A guide to GeoDa, GeoDaSpace and PySAL*; GeoDa Press: Chicago, IL, 2014, ISBN 9780986342103.

180. Fernando, G.W. R. Causes of forest dieback in montane forests in Sri Lanka. *Economic Review* **2008**, *34*, 38–40.
181. Requardt, A.; Poker, J.; Köhl, M.; Schuck, A.; Janse, G.; Mavsar, R.; Päivinen, R. Feasibility study on means of combating forest dieback in the European Union. *BFH & EFI Technical Report* **2007**.
182. White, T.C.R. Weather, Eucalyptus dieback in New England, and a general hypothesis of the cause of dieback. *Pacific Science* **1986**, *40*, 58–78.
183. Auclair, A.N. d. Extreme climatic fluctuations as a cause of forest dieback in the pacific rim. *Water, Air, and Soil Pollution* **1993**, *66*, 207–229, doi:10.1007/BF00479846.
184. Rice, K.J.; Matzner, S.L.; Byer, W.; Brown, J.R. Patterns of tree dieback in Queensland, Australia: the importance of drought stress and the role of resistance to cavitation. *Oecologia* **2004**, *139*, 190–198, doi:10.1007/s00442-004-1503-9.
185. Galiano, L.; Martínez-Vilalta, J.; Lloret, F. Drought-Induced Multifactor Decline of Scots Pine in the Pyrenees and Potential Vegetation Change by the Expansion of Co-occurring Oak Species. *Ecosystems* **2010**, *13*, 978–991, doi:10.1007/s10021-010-9368-8.
186. Matusick, G.; Ruthrof, K.X.; Brouwers, N.C.; Dell, B.; St. Hardy, G.J. Sudden forest canopy collapse corresponding with extreme drought and heat in a mediterranean-type eucalypt forest in southwestern Australia. *Eur J Forest Res* **2013**, *132*, 497–510, doi:10.1007/s10342-013-0690-5.
187. Steinkamp, J.; Hickler, T. Is drought-induced forest dieback globally increasing? *J Ecol* **2015**, *103*, 31–43, doi:10.1111/1365-2745.12335.
188. Guada, G.; Camarero, J.J.; Sánchez-Salguero, R.; Cerrillo, R.M.N. Limited Growth Recovery after Drought-Induced Forest Dieback in Very Defoliated Trees of Two Pine Species. *Front. Plant Sci.* **2016**, *7*, 418, doi:10.3389/fpls.2016.00418.
189. Hember, R.A.; Kurz, W.A.; Coops, N.C. Relationships between individual-tree mortality and water-balance variables indicate positive trends in water stress-induced tree mortality across North America. *Glob. Chang. Biol.* **2017**, *23*, 1691–1710, doi:10.1111/gcb.13428.
190. Mazdiasni, O.; AghaKouchak, A.; Davis, S.J.; Madadgar, S.; Mehran, A.; Ragno, E.; Sadegh, M.; Sengupta, A.; Ghosh, S.; Dhanya, C.T.; et al. Increasing probability of mortality during Indian heat waves. *Sci. Adv.* **2017**, *3*, e1700066, doi:10.1126/sciadv.1700066.
191. Huete, A.; Didan, K.; Miura, T.; Rodriguez, E.P.; Gao, X.; Ferreira, L.G. Overview of the radiometric and biophysical performance of the MODIS vegetation indices. *Remote Sensing of Environment* **2002**, *83*, 195–213, doi:10.1016/S0034-4257(02)00096-2.
192. Chandrasekar, K.; Sessa Sai, M.V.R.; Roy, P.S.; Dwevedi, R.S. Land Surface Water Index (LSWI) response to rainfall and NDVI using the MODIS Vegetation Index product. *International Journal of Remote Sensing* **2010**, *31*, 3987–4005, doi:10.1080/01431160802575653.
193. Gu, Y.; Hunt, E.; Wardlow, B.; Basara, J.B.; Brown, J.F.; Verdin, J.P. Evaluation of MODIS NDVI and NDWI for vegetation drought monitoring using Oklahoma Mesonet soil moisture data. *Geophys. Res. Lett.* **2008**, *35*, 395, doi:10.1029/2008GL035772.
194. Garbulsky, M.F.; Peñuelas, J.; Ogaya, R.; Filella, I. Leaf and stand-level carbon uptake of a Mediterranean forest estimated using the satellite-derived reflectance indices EVI and PRI. *International Journal of Remote Sensing* **2013**, *34*, 1282–1296, doi:10.1080/01431161.2012.718457.

195. Bajgain, R.; Xiao, X.; Wagle, P.; Basara, J.; Zhou, Y. Sensitivity analysis of vegetation indices to drought over two tallgrass prairie sites. *ISPRS Journal of Photogrammetry and Remote Sensing* **2015**, *108*, 151–160, doi:10.1016/j.isprsjprs.2015.07.004.
196. Senay, G.B.; Budde, M.E.; Verdin, J.P. Enhancing the Simplified Surface Energy Balance (SSEB) approach for estimating landscape ET: Validation with the METRIC model. *Agricultural Water Management* **2011**, *98*, 606–618, doi:10.1016/j.agwat.2010.10.014.
197. Moran, M.S. Thermal infrared measurement as an indicator of plant ecosystem health. *Thermal Remote Sensing in Land Surface Processing*; CRC Press, 2004; pp 303–328.
198. Anderson, M.C.; Hain, C.R.; Wardlow, B.D.; Pimstein, A.; Mecikalski, J.R.; Kustas, W.P. Thermal-based evaporative stress index for monitoring surface moisture depletion. In *Remote Sensing of Drought: Innovative Monitoring Approaches*; Wardlow, B.D., Anderson, M.C., Verdin, J.P., Eds.; CRC Press, 2012, ISBN 9781439835609.
199. Anderson, M.C.; Zolin, C.A.; Hain, C.R.; Semmens, K.; Tugrul Yilmaz, M.; Gao, F. Comparison of satellite-derived LAI and precipitation anomalies over Brazil with a thermal infrared-based Evaporative Stress Index for 2003–2013. *Journal of Hydrology* **2015**, *526*, 287–302, doi:10.1016/j.jhydrol.2015.01.005.
200. Senay, G.B.; Bohms, S.; Singh, R.K.; Gowda, P.H.; Velpuri, N.M.; Alemu, H.; Verdin, J.P. Operational Evapotranspiration Mapping Using Remote Sensing and Weather Datasets: A New Parameterization for the SSEB Approach. *J Am Water Resour Assoc* **2013**, *49*, 577–591, doi:10.1111/jawr.12057.
201. Otkin, J.A.; Anderson, M.C.; Hain, C.; Mladenova, I.E.; Basara, J.B.; Svoboda, M. Examining Rapid Onset Drought Development Using the Thermal Infrared–Based Evaporative Stress Index. *J. Hydrometeor* **2013**, *14*, 1057–1074, doi:10.1175/JHM-D-12-0144.1.
202. Toomey, M.; Roberts, D.A.; Still, C.; Goulden, M.L.; McFadden, J.P. Remotely sensed heat anomalies linked with Amazonian forest biomass declines. *Geophys. Res. Lett.* **2011**, *38*, n/a–n/a, doi:10.1029/2011GL049041.
203. Jimenez-Munoz, J.C.; Sobrino, J.A.; Mattar, C.; Malhi, Y. Multi-temporal analysis of MODIS Land Products over the Amazon region. In *IEEE International Geoscience and Remote Sensing Symposium (IGARSS), 2012. IGARSS 2012 - 2012 IEEE International Geoscience and Remote Sensing Symposium*, Munich, Germany, 7/22/2012 - 7/27/2012; IEEE: Piscataway, NJ, 7/22/2012 - 7/27/2012; pp 6439–6442, ISBN 978-1-4673-1159-5.
204. Xu, L.; Samanta, A.; Costa, M.H.; Ganguly, S.; Nemani, R.R.; Myneni, R.B. Widespread decline in greenness of Amazonian vegetation due to the 2010 drought. *Geophys. Res. Lett.* **2011**, *38*, n/a–n/a, doi:10.1029/2011GL046824.
205. Rimkus, E.; Stonevicius, E.; Kilpys, J.; Maciulyte, V.; Valiukas, D. Drought identification in the eastern Baltic region using NDVI. *Earth Syst. Dynam.* **2017**, *8*, 627–637, doi:10.5194/esd-8-627-2017.
206. Abdi, O.; Shirvani, Z.; Buchroithner, M.F. Spatiotemporal drought evaluation of Hyrcanian deciduous forests and semi-steppe rangelands using moderate resolution imaging spectroradiometer time series in Northeast Iran. *Land Degrad. Develop.* **2018**, *29*, 2525–2541, doi:10.1002/ldr.3025.



207. Mitchell, P.J.; O'Grady, A.P.; Hayes, K.R.; Pinkard, E.A. Exposure of trees to drought-induced die-off is defined by a common climatic threshold across different vegetation types. *Ecol. Evol.* **2014**, *4*, 1088–1101, doi:10.1002/ece3.1008.
208. Boyer, J.S. Biochemical and biophysical aspects of water deficits and the predisposition to disease. *Annu. Rev. Phytopathol.* **1995**, *33*, 251–274, doi:10.1146/annurev.py.33.090195.001343.
209. Brodribb, T.J.; Bowman, D.J.M.S.; Nichols, S.; Delzon, S.; Burlett, R. Xylem function and growth rate interact to determine recovery rates after exposure to extreme water deficit. *New Phytol.* **2010**, *188*, 533–542, doi:10.1111/j.1469-8137.2010.03393.x.
210. Vose, J.M.; Miniati, C.F.; Luce, C.H.; Asbjornsen, H.; Caldwell, P.V.; Campbell, J.L.; Grant, G.E.; Isaak, D.J.; Loheide, S.P.; Sun, G. Ecohydrological implications of drought for forests in the United States. *Forest Ecology and Management* **2016**, *380*, 335–345, doi:10.1016/j.foreco.2016.03.025.
211. Scott, M.L.; Shafroth, P.B.; Auble, G.T. Responses of Riparian Cottonwoods to Alluvial Water Table Declines. *Environmental Management* **1999**, *23*, 347–358, doi:10.1007/s002679900191.
212. David, T.S.; Pinto, C.A.; Nadezhkina, N.; David, J.S. Water and forests in the Mediterranean hot climate zone: a review based on a hydraulic interpretation of tree functioning. *Forest Syst* **2016**, *25*, eR02, doi:10.5424/fs/2016252-08899.
213. Anderson, L.O.; Malhi, Y.; Aragão, L.E.O.C.; Ladle, R.; Arai, E.; Barbier, N.; Phillips, O. Remote sensing detection of droughts in Amazonian forest canopies. *New Phytol.* **2010**, *187*, 733–750, doi:10.1111/j.1469-8137.2010.03355.x.
214. Samanta, A.; Ganguly, S.; Hashimoto, H.; Devadiga, S.; Vermote, E.; Knyazikhin, Y.; Nemani, R.R.; Myneni, R.B. Amazon forests did not green-up during the 2005 drought. *Geophys. Res. Lett.* **2010**, *37*, n/a–n/a, doi:10.1029/2009GL042154.
215. Klein, T.; Yakir, D.; Buchmann, N.; Grünzweig, J.M. Towards an advanced assessment of the hydrological vulnerability of forests to climate change-induced drought. *New Phytol.* **2014**, *201*, 712–716, doi:10.1111/nph.12548.
216. Spinoni, J.; Naumann, G.; Carrao, H.; Barbosa, P.; Vogt, J. World drought frequency, duration, and severity for 1951–2010. *Int. J. Climatol* **2014**, *34*, 2792–2804, doi:10.1002/joc.3875.
217. Brito, S.S.B.; Cunha, A.P.M.A.; Cunningham, C.C.; Alvalá, R.C.; Marengo, J.A.; Carvalho, M.A. Frequency, duration and severity of drought in the Semiarid Northeast Brazil region. *Int. J. Climatol* **2018**, *38*, 517–529, doi:10.1002/joc.5225.
218. Diffenbaugh, N.S.; Pal, J.S.; Trapp, R.J.; Giorgi, F. Fine-scale processes regulate the response of extreme events to global climate change. *Proc. Natl. Acad. Sci. U. S. A.* **2005**, *102*, 15774–15778, doi:10.1073/pnas.0506042102.
219. Park Williams, A.; Allen, C.D.; Macalady, A.K.; Griffin, D.; Woodhouse, C.A.; Meko, D.M.; Swetnam, T.W.; Rauscher, S.A.; Seager, R.; Grissino-Mayer, H.D.; et al. Temperature as a potent driver of regional forest drought stress and tree mortality. *Nature Clim Change* **2013**, *3*, 292–297, doi:10.1038/nclimate1693.
220. Malone, S. Monitoring Changes in Water Use Efficiency to Understand Drought Induced Tree Mortality. *Forests* **2017**, *8*, 365, doi:10.3390/f8100365.



- 
221. Rosbakh, S.; Leingärtner, A.; Hoiss, B.; Krauss, J.; Steffan-Dewenter, I.; Poschlod, P. Contrasting Effects of Extreme Drought and Snowmelt Patterns on Mountain Plants along an Elevation Gradient. *Front. Plant Sci.* **2017**, *8*, 1478, doi:10.3389/fpls.2017.01478.
222. Mueller, R.C.; Scudder, C.M.; Porter, M.E.; Talbot Trotter, I.; Catherine, A.G.; Whitham, T.G. Differential tree mortality in response to severe drought: evidence for long-term vegetation shifts. *J Ecol* **2005**, *93*, 1085–1093, doi:10.1111/j.1365-2745.2005.01042.x.
223. Oyana, T.J.; Margai, F. *Spatial Analysis. Visualization, and Computational Methods*; CRC Press: Boca Raton, 2015, ISBN 9780429069369.
224. McKee, T.B.; Doesken, N.J.; Kleist, J. The relationship of drought frequency and duration to time scales. In *Proceedings of the 8th Conference on Applied Climatology*; American Meteorological Society: Boston, MA, 1993; pp 179–183.
225. Nalbantis, I. Evaluation of a hydrological drought index. *European Water* **2008**, *23*, 67–77.
226. Bhuiyan, C. Various drought indices for monitoring drought condition in Aravalli terrain of India. In *Proceedings of the XXth ISPRS Congress*, Istanbul, Turkey, July 12–23, 2004; Orhan Altan, Ed.; ISPRS: Istanbul, Turkey, 2004; pp 12–23.
227. Wan, Z.; Hook, S.; Hulley, G. *MOD11A2 MODIS/Terra Land Surface Temperature/Emissivity 8-Day L3 Global 1km SIN Grid V006*, 2015.
228. Tadesse, T.; Wardlow, B.D.; Hayes, M.J.; Svoboda, M.D.; Brown, J.F. The Vegetation Outlook (VegOut): A New Method for Predicting Vegetation Seasonal Greenness. *GIScience & Remote Sensing* **2010**, *47*, 25–52, doi:10.2747/1548-1603.47.1.25.
229. ESRI. How Fuzzy Membership Works. <http://desktop.arcgis.com/en/arcmap/10.5/tools/spatial-analyst-toolbox/how-fuzzy-membership-works.htm> (accessed on 4 April 2019).
230. Simpson, E.H. Measurement of Diversity. *Nature* **1949**, *163*, 688, doi:10.1038/163688a0.
231. Boenigk, J.; Wodniok, S.; Glücksman, E. *Biodiversity and Earth History*; Springer Berlin Heidelberg: Berlin, Heidelberg, 2015, ISBN 978-3-662-46393-2.
232. Anselin, L. Local Indicators of Spatial Association-LISA. *Geographical Analysis* **1995**, *27*, 93–115, doi:10.1111/j.1538-4632.1995.tb00338.x.
233. Anselin, L. *SpaceStat tutorial: a workbook for using SpaceStat in the analysis of spatial data*; Urbana-Champaign: University of Illinois, 1992.
234. Burridge, P. On the Cliff-Ord test for spatial correlation. *Journal of the Royal Statistical Society. Series B (Methodological)* **1980**, 107–108.
235. Corlett, R.T. Impacts of warming on tropical lowland rainforests. *Trends Ecol. Evol. (Amst)* **2011**, *26*, 606–613, doi:10.1016/j.tree.2011.06.015.
236. Clyatt, K.A.; Crotteau, J.S.; Schaedel, M.S.; Wiggins, H.L.; Kelley, H.; Churchill, D.J.; Larson, A.J. Historical spatial patterns and contemporary tree mortality in dry mixed-conifer forests. *Forest Ecology and Management* **2016**, *361*, 23–37, doi:10.1016/j.foreco.2015.10.049.
237. Rullan-Silva, C.D.; Olthoff, A.E.; La Delgado de Mata, J.A.; Pajares-Alonso, J.A. Remote Monitoring of Forest Insect Defoliation -A Review-. *Forest Syst* **2013**, *22*, 377, doi:10.5424/fs/2013223-04417.

238. Hall, R.J.; Castilla, G.; White, J.C.; Cooke, B.J.; Skakun, R.S. Remote sensing of forest pest damage: a review and lessons learned from a Canadian perspective. *Can Entomol* **2016**, *148*, S296-S356, doi:10.4039/tce.2016.11.
239. Senf, C.; Seidl, R.; Hostert, P. Remote sensing of forest insect disturbances: Current state and future directions. *Int. J. Appl. Earth Obs. Geoinf.* **2017**, *60*, 49–60, doi:10.1016/j.jag.2017.04.004.
240. Abatzoglou, J.T.; Dobrowski, S.Z.; Parks, S.A.; Hegewisch, K.C. TerraClimate, a high-resolution global dataset of monthly climate and climatic water balance from 1958-2015. *Sci. Data* **2018**, *5*, 170191, doi:10.1038/sdata.2017.191.
241. Latifi, H.; Fassnacht, F.E.; Schumann, B.; Dech, S. Object-based extraction of bark beetle (*Ips typographus* L.) infestations using multi-date LANDSAT and SPOT satellite imagery. *Progress in Physical Geography: Earth and Environment* **2014**, *38*, 755–785, doi:10.1177/0309133314550670.
242. Meddens, A.J.H.; Hicke, J.A. Spatial and temporal patterns of Landsat-based detection of tree mortality caused by a mountain pine beetle outbreak in Colorado, USA. *Forest Ecology and Management* **2014**, *322*, 78–88, doi:10.1016/j.foreco.2014.02.037.
243. De Beurs, K.M.; Townsend, P.A. Estimating the effect of gypsy moth defoliation using MODIS. *Remote Sensing of Environment* **2008**, *112*, 3983–3990, doi:10.1016/j.rse.2008.07.008.
244. Babst, F.; Esper, J.; Parlow, E. Landsat TM/ETM+ and tree-ring based assessment of spatiotemporal patterns of the autumnal moth (*Epirrita autumnata*) in northernmost Fennoscandia. *Remote Sensing of Environment* **2010**, *114*, 637–646, doi:10.1016/j.rse.2009.11.005.
245. Meddens, A.J.H.; Hicke, J.A.; Vierling, L.A.; Hudak, A.T. Evaluating methods to detect bark beetle-caused tree mortality using single-date and multi-date Landsat imagery. *Remote Sensing of Environment* **2013**, *132*, 49–58, doi:10.1016/j.rse.2013.01.002.
246. Vastaranta, M.; Kantola, T.; Lyytikäinen-Saarenmaa, P.; Holopainen, M.; Kankare, V.; Wulder, M.; Hyypä, J.; Hyypä, H. Area-Based Mapping of Defoliation of Scots Pine Stands Using Airborne Scanning LiDAR. *Remote Sensing* **2013**, *5*, 1220–1234, doi:10.3390/rs5031220.
247. Goodwin, N.R.; Coops, N.C.; Wulder, M.A.; Gillanders, S.; Schroeder, T.A.; Nelson, T. Estimation of insect infestation dynamics using a temporal sequence of Landsat data. *Remote Sensing of Environment* **2008**, *112*, 3680–3689, doi:10.1016/j.rse.2008.05.005.
248. Paritsis, J.; Veblen, T.T.; Smith, J.M.; Holz, A. Spatial prediction of caterpillar (*Ormiscodes*) defoliation in Patagonian *Nothofagus* forests. *Landscape Ecol* **2011**, *26*, 791–803, doi:10.1007/s10980-011-9608-0.
249. Thayn, J.B. Using a remotely sensed optimized Disturbance Index to detect insect defoliation in the Apostle Islands, Wisconsin, USA. *Remote Sensing of Environment* **2013**, *136*, 210–217, doi:10.1016/j.rse.2013.05.008.
250. Heurich, M.; Ochs, T.; Andresen, T.; Schneider, T. Object-orientated image analysis for the semi-automatic detection of dead trees following a spruce bark beetle (*Ips typographus*) outbreak. *Eur J Forest Res* **2010**, *129*, 313–324, doi:10.1007/s10342-009-0331-1.
251. Latifi, H.; Schumann, B.; Kautz, M.; Dech, S. Spatial characterization of bark beetle infestations by a multirate synergy of SPOT and Landsat imagery. *Environ. Monit. Assess.* **2014**, *186*, 441–456, doi:10.1007/s10661-013-3389-7.

- 
252. Ryan, M.G.; Vose, J.M. *Effects of climatic variability and change*; Effects of climatic variability and change on forest ecosystems: a comprehensive science synthesis for the U.S. forest sector PNW-GTR-870, 2012. <https://www.fs.usda.gov/treearch/pubs/42651> (accessed on 2 August 2019).
253. Jepsen, J.U.; Kapari, L.; Hagen, S.B.; Schott, T.; Vindstad, O.P.L.; Nilssen, A.C. and Ims, R.A. Rapid northwards expansion of a forest insect pest attributed to spring phenology matching with sub-Arctic birch. *Glob. Chang. Biol.* **2011**, *17*, 2071–2083, doi:10.1111/j.1365-2486.2010.02370.x.
254. Rouault, G.; Candau, J.-N.; Lieutier, F.; Nageleisen, L.-M.; Martin, J.-C.; Warzée, N. Effects of drought and heat on forest insect populations in relation to the 2003 drought in Western Europe. *Ann. For. Sci.* **2006**, *63*, 613–624, doi:10.1051/forest:2006044.
255. Ryerson, D.E.; Swetnam, T.W.; Lynch, A.M. A tree-ring reconstruction of western spruce budworm outbreaks in the San Juan Mountains, Colorado, U.S.A. *Can. J. For. Res.* **2003**, *33*, 1010–1028, doi:10.1139/x03-026.
256. Thomson, A.J.; Shepherd, R.F.; Harris, J.W.E.; Silversides, R.H. Relating weather to outbreaks of western spruce budworm, *Choristoneura occidentalis* (Lepidoptera: Tortricidae), in British Columbia. *Can Entomol* **1984**, *116*, 375–381, doi:10.4039/Ent116375-3.
257. Abdi, O.; Shirvani, Z.; Buchroithner, M.F. Forest drought-induced diversity of Hyrcanian individual-tree mortality affected by meteorological and hydrological droughts by analyzing moderate resolution imaging spectroradiometer products and spatial autoregressive models over northeast Iran. *Agricultural and Forest Meteorology* **2019**, *275*, 265–276, doi:10.1016/j.agrformet.2019.05.029.
258. Setayeshgar, F. The attack of *Lymantria dispar* to 420 hectares of Hyrcanian forests: Outbreak of defoliators in the forests. <http://khorasannews.com/?nid=18724&type=0> (accessed on 1-July 2014).
259. F.A.O. *Food Chain Crisis Early Warning Bulletin. Alerts on threats to the food chain affecting food security in countries and regions* No. 18, 2016. [www.fao.org/food-chain-crisis](http://www.fao.org/food-chain-crisis) (accessed on 20 July 2019).
260. U.S. Geological Survey, Earth Resources Observation Science Center. *Collection-1 Landsat OLI Level-2 Surface Reflectance (SR) Science Product*, 2019 (accessed on 1 June 2019).
261. ASF DAAC. *PALSAR\_Radiometric\_Terrain\_Corrected\_high\_res; Includes Material* © JAXA/METI 2007, 2019 (accessed on 1 June 2019).
262. Department of Natural Resources and Watershed Management of Golestan. *The Booklets of Forest Management Plans: Jafarabad, Golriz, Tavir, Kohmian, Zarringol, Sorkhdari, Rezaeian, Qalemorian, Daland, Vatan, Nodeh-Bon-Qale, Minudasht, Takht, Loveh, Sijan-Kiaram, Korankaftar, Terjenli; Gorgan*, 1981-2011 (accessed on 12 April 2015).
263. Google earth pro V 7.3.2.5491. *Sousara, Golestan Province. 37° 00' 47.58"N, 55° 16' 30.88"E, Eye alt 10.17 km.*; Google LLC: Mountain View, USA, 2019.
264. eCognition Developer, T. 9.0 User Guide. *Trimble Germany GmbH: Munich, Germany* **2014**.
265. Crippen, R. Calculating the vegetation index faster. *Remote Sensing of Environment* **1990**, *34*, 71–73, doi:10.1016/0034-4257(90)90085-Z.
266. Pinty, B.; Verstraete, M.M. GEMI: a non-linear index to monitor global vegetation from satellites. *Vegetatio* **1992**, *101*, 15–20, doi:10.1007/BF00031911.

267. Kaufman, Y.J.; d. Tanre. Atmospherically resistant vegetation index (ARVI) for EOS-MODIS. *IEEE Trans. Geosci. Remote Sensing* **1992**, *30*, 261–270, doi:10.1109/36.134076.
268. Gitelson, A.A.; Kaufman, Y.J.; Merzlyak, M.N. Use of a green channel in remote sensing of global vegetation from EOS-MODIS. *Remote Sensing of Environment* **1996**, *58*, 289–298, doi:10.1016/S0034-4257(96)00072-7.
269. Jiang, Z.; Huete, A.R.; Didan, K.; Miura, T. Development of a two-band enhanced vegetation index without a blue band. *Remote Sensing of Environment* **2008**, *112*, 3833–3845, doi:10.1016/j.rse.2008.06.006.
270. Singh, A.; Harrison, A. Standardized principal components. *International Journal of Remote Sensing* **1985**, *6*, 883–896, doi:10.1080/01431168508948511.
271. Kauth, R.J.; Thomas, G.S. The tasselled cap-a graphic description of the spectral-temporal development of agricultural crops as seen by landsat. Purdue University: West Lafayette, USA, 1976.
272. Haralick, R.M.; Shanmugam, K.; Dinstein, I.H. Textural Features for Image Classification. *IEEE Trans. Syst., Man, Cybern.* **1973**, *SMC-3*, 610–621, doi:10.1109/TSMC.1973.4309314.
273. Navulur, K. *Multispectral Image Analysis Using the Object-Oriented Paradigm*; CRC Press, 2006, ISBN 9780429146305.
274. Moore, I. d.; Grayson, R.B.; Ladson, A.R. Digital terrain modelling: A review of hydrological, geomorphological, and biological applications. *Hydrol. Process.* **1991**, *5*, 3–30, doi:10.1002/hyp.3360050103.
275. Wilson, John, P.; Gallant, John, C. *Terrain analysis. Principles and applications*; John Wiley & Sons: New York, 2000, ISBN 978-0-471-32188-0.
276. Riley, S. J., DeGloria, S. D., & Elliot, R. Index that quantifies topographic heterogeneity. **1999**, *5*, 23–27.
277. Salford Systems Ltd. *Salford Predictive Modeler 8.3*; Salford Systems Ltd.: San Diego, USA, 2018.
278. Kandel, K.; Huettmann, F.; Suwal, M.K.; Ram Regmi, G.; Nijman, V.; Nekaris, K.A.I.; Lama, S.T.; Thapa, A.; Sharma, H.P.; Subedi, T.R. Rapid multi-nation distribution assessment of a charismatic conservation species using open access ensemble model GIS predictions: Red panda (*Ailurus fulgens*) in the Hindu-Kush Himalaya region. *Biological Conservation* **2015**, *181*, 150–161, doi:10.1016/j.biocon.2014.10.007.
279. ESRI. How Fuzzy Overlay works. <http://desktop.arcgis.com/en/arcmap/10.5/tools/spatial-analyst-toolbox/how-fuzzy-overlay-works.htm> (accessed on 1 May 2019).
280. Key, C.H.; Benson, N.C. *Landscape assessment: Remote sensing of severity, the Normalized Burn Ratio; FIREMON: Fire effects monitoring and inventory system RMRS-GTR-164-CD: LA 1-51*, 2006. <http://pubs.er.usgs.gov/publication/2002085> (accessed on 8 February 2019).
281. Miller, J. d.; Thode, A.E. Quantifying burn severity in a heterogeneous landscape with a relative version of the delta Normalized Burn Ratio (dNBR). *Remote Sensing of Environment* **2007**, *109*, 66–80, doi:10.1016/j.rse.2006.12.006.

- 
282. Elhorst, J.P. Spatial Panel Data Models. In *Spatial Econometrics: From Cross-Sectional Data to Spatial Panels*; Elhorst, J.P., Ed.; Springer Berlin Heidelberg: Berlin, Heidelberg, 2014; pp 37–93, ISBN 978-3-642-40340-8.
283. Greene, W.H. *Econometric analysis*, 5th ed.; Prentice Hall: Upper Saddle River, NJ, 2002, ISBN 0-13-066189-9.
284. Elhorst, J.P. Spatial Panel Data Models. In *Handbook of Applied Spatial Analysis*; Fischer, M.M., Getis, A., Eds.; Springer Berlin Heidelberg: Berlin, Heidelberg, 2010; pp 377–407, ISBN 978-3-642-03646-0.
285. Bell, A.; Jones, K. Explaining Fixed Effects: Random Effects Modeling of Time-Series Cross-Sectional and Panel Data. *PSRM* **2015**, *3*, 133–153, doi:10.1017/psrm.2014.7.
286. Hausman, J.A. Specification Tests in Econometrics. *Econometrica* **1978**, *46*, 1251, doi:10.2307/1913827.
287. Baltagi, B.H. *Econometric analysis of panel data*, 4th ed.; John Wiley & Sons: Chichester, UK, 2008, ISBN 0-470-01456-3.
288. Carter, G.A. Responses of Leaf Spectral Reflectance to Plant Stress. *American Journal of Botany* **1993**, *80*, 239, doi:10.2307/2445346.
289. Carter, G.A.; Cibula, W.G.; Miller, R.L. Narrow-band Reflectance Imagery Compared with Thermal Imagery for Early Detection of Plant Stress. *Journal of Plant Physiology* **1996**, *148*, 515–522, doi:10.1016/S0176-1617(96)80070-8.
290. Muchoney, D.M.; Haack, B.N. Change Detection for Monitoring Forest Defoliation. *Photogrammetric engineering and remote sensing* **1994**, *60*, 1243–1252.
291. Moskal, L.M.; Franklin, S.E. Relationship between airborne multispectral image texture and aspen defoliation. *International Journal of Remote Sensing* **2004**, *25*, 2701–2711, doi:10.1080/01431160310001642304.
292. Lottering, R.; Mutanga, O.; Peerbhay, K.; Ismail, R. Detecting and mapping *Gonipterus scutellatus* induced vegetation defoliation using WorldView-2 pan-sharpened image texture combinations and an artificial neural network. *J. Appl. Rem. Sens.* **2019**, *13*, 1, doi:10.1117/1.JRS.13.014513.
293. Olsson, P.-O.; Jönsson, A.M.; Eklundh, L. A new invasive insect in Sweden – *Physokermes inopinatus*: Tracing forest damage with satellite based remote sensing. *Forest Ecology and Management* **2012**, *285*, 29–37, doi:10.1016/j.foreco.2012.08.003.



# Appendix A

---

**Supplementary Tables and Figures of Chapter 3**

**Table 3.S1** Cross-validation of monthly precipitation estimation based on the different semi-variogram models from rain gauges from 1987 to 2016.

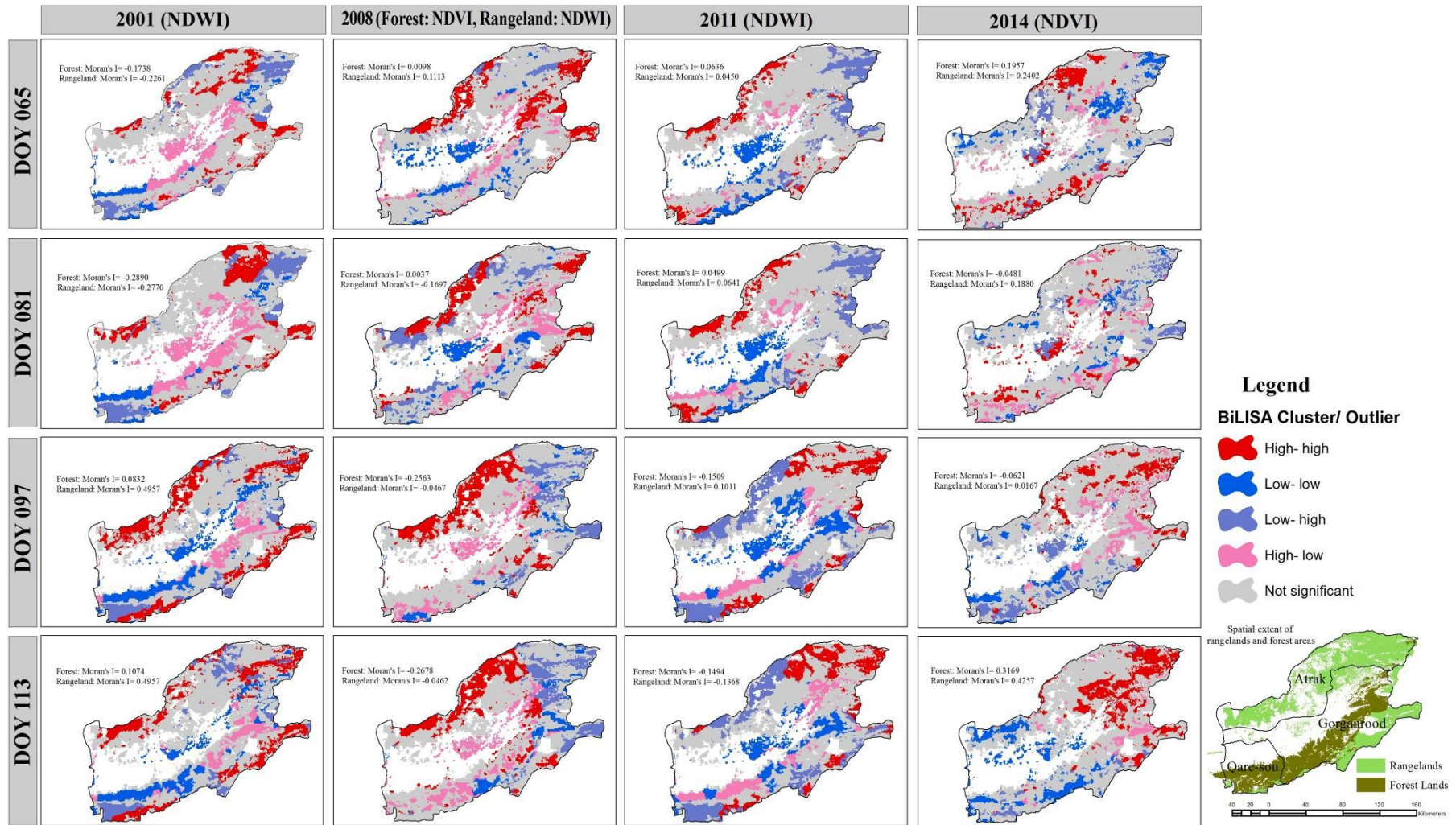
YEAR		Jan.			Feb.			Mar.			Apr.			May			Jun.	
	Model*	ME (mm)	RMSSE	Model*	ME (mm)	RMSSE	Model*	ME (mm)	RMSSE	Model*	ME (mm)	RMSSE	Model*	ME (mm)	RMSSE	Model*	ME (mm)	RMSSE
1987	S - G	0.96	1.19	S - G	2.05	1.01	S - G	3.86	0.80	S	6.36	0.73	S	1.35	0.87	S	0.45	0.84
1988	S - G	0.52	1.04	S - G	0.90	0.99	S - G	2.65	0.78	S - G	2.32	1.00	S - G	1.88	1.03	S	0.10	0.91
1989	S - G	0.49	1.17	S - G	0.39	0.98	S - G	-2.05	1.03	S - G	1.62	0.92	S - G	0.09	1.12	EBK	0.01	0.93
1990	S - G	0.05	0.93	S - G	-1.54	1.08	S - G	0.38	1.02	S - G	1.42	0.84	S - G	-0.63	1.03	EBK	1.12	0.94
1991	S	1.95	1.00	S - G	0.96	0.91	S - G	1.08	0.90	S - G	0.85	1.07	S - G	0.64	0.97	SRG	0.17	0.97
1992	G - S	-0.14	0.93	S - G	0.89	0.98	S - G	0.012	0.98	S	2.32	0.95	S	4.18	0.96	PS	0.79	0.96
1993	G	-1.41	1.05	G	-1.09	1.02	S - G	0.23	0.97	PS	0.29	1.11	S	2.56	0.91	G	1.94	1.04
1994	PS	1.13	1.03	G	1.13	1.03	G	1.16	0.91	S	1.92	0.83	G	0.47	1.12	EBK	0.16	0.99
1995	G	0.73	1.15	S	1.68	0.81	G	-0.01	1.04	S	-0.29	0.98	S	-0.01	0.87	EBK	0.14	0.95
1996	G	0.29	0.95	S	0.09	1.02	S	0.52	0.99	S	0.48	1.15	EBK	0.72	0.96	PS	0.35	1.00
1997	EBK	-0.13	0.93	RG	-0.56	1.22	G	2.78	0.99	S	1.76	0.97	PS	1.69	0.95	G	0.51	0.87
1998	TS	0.19	1.09	S	0.98	0.96	S	-0.13	1.06	G	0.88	1.03	G	1.54	0.99	EBK	0.51	0.96
1999	EBK	0.5	0.96	G	1.22	1.00	S	2.58	1.00	S	0.61	0.99	G	1.28	1.04	EBK	-0.06	1.00
2000	G	0.37	1.05	G	0.83	1.04	S	2.18	1.17	EBK	0.11	0.95	EBK	0.61	0.97	S	0.41	1.09
2001	S	0.11	1.07	G	1.12	1.06	S	0.93	0.93	S	1.94	1.01	G	0.87	1.00	EBK	0.77	0.95
2002	EBK	0.60	0.96	G	1.15	1.00	EBK	0.84	0.97	S	1.63	0.93	G	0.90	1.03	EBK	0.70	1.00
2003	PS	0.58	1.10	G	0.86	1.00	ST	1.41	1.02	G	0.53	0.96	S	1.59	0.98	S	1.19	1.04
2004	RG	0.51	1.22	S	1.43	0.94	S	0.98	1.05	TS	2.06	0.94	G	0.11	1.04	TS	0.77	0.88
2005	S	1.02	1.05	G	0.75	1.05	PS	1.37	0.92	S	3.19	1.05	S	1.34	0.99	S	1.33	0.99
2006	S	1.27	1.01	S	0.80	1.00	G	0.52	0.92	S	1.56	1.05	S	0.89	1.01	EBK	-0.09	0.96
2007	S	0.80	0.99	EBK	0.47	0.93	PS	1.10	0.95	S	0.27	1.01	S	0.57	0.99	EBK	0.73	0.90
2008	G	0.09	1.01	EBK	0.48	1.05	G	0.45	0.93	G	-0.03	1.04	G	0.03	0.98	PS	0.47	0.94
2009	G	0.21	0.98	RG	1.37	0.91	EBK	0.42	0.97	S	0.74	0.99	EBK	0.40	0.97	EBK	0.082	0.93
2010	TS	0.29	0.89	S	0.90	1.06	S	1.09	1.08	G	0.10	1.01	S	0.86	1.00	EBK	6.23	1.01
2011	G	0.90	1.08	G	0.21	0.95	G	0.41	0.93	EBK	0.17	0.94	G	0.51	0.97	EBK	0.08	0.92
2012	G	0.28	0.92	G	1.02	1.01	S	0.79	0.93	S	1.44	0.83	G	-0.05	1.01	PS	0.72	0.90
2013	G	0.77	0.99	G	0.97	0.83	G	2.55	0.82	G	0.15	1.04	S	0.84	0.96	EBK	0.03	0.91
2014	EBK	0.03	0.92	S	0.15	0.99	G	1.94	1.00	EBK	1.37	0.99	EBK	-0.004	1.00	EBK	0.04	0.94
2015	EBK	0.15	0.98	S	1.12	0.90	EBK	0.78	1.01	EBK	-0.25	0.98	EBK	1.11	0.99	EBK	-0.03	0.97
2016	EBK	0.07	0.97	EBK	0.34	0.98	EBK	1.14	0.98	EBK	0.78	1.00	G	0.51	0.97	PS	0.70	0.93
Mean		0.439	1.02		0.75	0.99		1.06	0.97		1.21	0.98		0.89	0.99		0.67	0.96



Table 3.S1 Continued

YEAR	Jul.			Aug.			Sep.			Oct.			Nov.			Dec.		
	Model*	ME (mm)	RMSSE	Model*	ME (mm)	RMSSE	Model*	ME (mm)	RMSSE	Model*	ME (mm)	RMSSE	Model*	ME (mm)	RMSSE	Model*	ME (mm)	RMSSE
1987	EBK	-0.56	1.02	EBK	1.25	0.92	EBK	3.47	0.96	S - G	1.22	0.85	S - G	0.91	1.04	S - G	0.029	0.96
1988	EBK	0.25	0.94	S - G	0.62	0.97	EBK	0.20	0.95	EBK	1.75	0.98	S - G	1.78	0.98	S - G	0.94	1.03
1989	EBK	-0.82	0.96	S	-1.36	1.03	S - G	0.78	0.98	S - G	-0.23	0.96	S - G	0.034	0.97	EBK	2.78	1.00
1990	EBK	0.17	1.00	EBK	0.96	0.60	S - G	0.29	0.91	S - G	0.08	1.01	S - G	1.04	1.07	S - G	-0.81	0.98
1991	EBK	0.68	0.93	EBK	0.026	0.94	EBK	0.32	0.94	S - G	1.01	0.96	S - G	-0.5	0.87	S - G	-0.07	0.87
1992	EBK	0.36	0.96	S	0.96	0.82	EBK	1.15	0.94	EBK	-0.002	0.90	EBK	-0.08	0.96	G	1.24	1.01
1993	S	0.23	1.01	EBK	0.87	0.96	S	0.005	0.92	EBK	-0.02	0.99	G	1.55	0.99	S	0.19	0.99
1994	S	0.33	0.96	EBK	0.39	1.00	S	0.97	0.96	G	1.16	1.07	G	0.17	1.02	PS	0.80	1.12
1995	S	0.37	0.91	EBK	0.32	0.96	PS	0.19	0.80	S	1.61	0.96	RG	1.09	0.81	G	1.01	0.94
1996	EBK	0.09	0.91	EBK	0.1	1.02	EBK	-0.39	1.004	G	1.81	1.04	G	1.67	1.08	RG	-1.37	1.04
1997	EBK	1.81	0.98	EBK	0.33	0.99	PS	1.11	1.00	S	0.33	0.96	G	1.26	1.01	G	-0.14	1.00
1998	EBK	0.77	0.97	EBK	-0.07	0.95	G	1.10	0.94	G	1.49	0.93	EBK	0.45	0.99	EBK	0.50	0.96
1999	G	0.39	0.94	G	-0.32	1.04	S	0.56	0.90	S	3.01	1.10	S	0.77	1.00	S	1.10	1.01
2000	EBK	0.11	0.96	S	1.29	0.85	S	2.07	0.94	RG	1.73	0.89	S	0.61	0.94	S	0.99	1.01
2001	EBK	-0.22	0.98	EBK	1.54	0.96	EBK	0.82	0.96	EBK	0.01	0.96	G	0.82	1.01	S	0.86	1.30
2002	EBK	0.36	0.95	ST	1.05	1.09	G	0.53	0.98	EBK	0.51	0.94	PS	0.42	1.09	G	1.02	0.92
2003	EBK	0.44	0.92	S	0.68	0.97	EBK	0.31	0.94	PS	0.84	0.93	G	1.27	0.97	G	0.87	0.92
2004	G	1.10	0.82	EBK	0.04	0.94	PS	0.66	0.99	G	0.36	0.95	PS	1.31	0.87	G	1.47	0.97
2005	EBK	0.08	0.97	EBK	0.94	0.96	EBK	0.32	0.89	PS	1.07	0.92	PS	1.47	0.98	PS	0.51	0.93
2006	EBK	0.09	0.91	EBK	0.026	0.911	SP	0.65	1.09	EBK	-0.02	0.97	S	3.06	0.93	TS	1.78	0.96
2007	EBK	0.39	0.93	EBK	-0.54	0.93	EBK	0.17	0.92	PS	0.95	1.02	EBK	0.32	0.91	S	1.07	1.02
2008	G	0.16	0.96	EBK	-0.01	1.04	EBK	-0.01	0.92	EBK	1.45	0.87	G	0.27	0.97	RG	0.77	1.00
2009	EBK	0.013	0.98	S	0.84	0.94	PS	0.60	0.97	TS	0.65	0.89	G	0.82	1.10	TS	1.65	0.98
2010	EBK	0.10	0.93	EBK	-0.006	0.90	EBK	0.67	1.00	EBK	0.51	0.92	EBK	0.29	0.94	EBK	0.21	0.96
2011	G	0.47	0.91	S	0.22	1.05	G	0.89	0.92	G	2.01	0.95	S	0.90	0.92	G	0.97	0.98
2012	G	5.82	0.93	EBK	0.13	0.91	G	0.70	0.92	S	1.56	1.00	G	0.85	1.00	G	0.48	1.07
2013	EBK	0.15	0.90	EBK	0.10	0.94	EBK	0.15	0.92	S	1.99	1.02	EBK	0.06	0.95	G	4.94	1.01
2014	EBK	0.003	1.01	EBK	0.08	0.97	EBK	0.39	0.97	EBK	0.19	0.96	RG	1.17	0.96	G	0.46	1.03
2015	EBK	0.13	1.00	EBK	0.04	0.98	EBK	-0.14	0.96	EBK	0.99	1.00	EBK	0.1	0.99	EBK	2.73	1.00
2016	G	0.04	1.02	S	0.17	1.03	SP	0.16	1.02	EBK	0.98	1.03	S	0.40	0.96	G	0.37	0.98
Mean		0.44	0.95		0.35	0.95		0.62	0.95		0.96	0.96		0.81	0.98		0.91	0.99

\*Semi-variogram models. S: Spherical; G: Gaussian; PS: Pentaspherical; TS: Tetrasheral; RQ: Rational Quadratic; EBK: Empirical Bayesian Kriging; ST: Stable



**Figure 3.S1** Spatial variations of BiLISA cluster/ outlier of DOY 65 to DOY 113 during drought periods (Significance level= 0.05, Randomization permutations= 499).



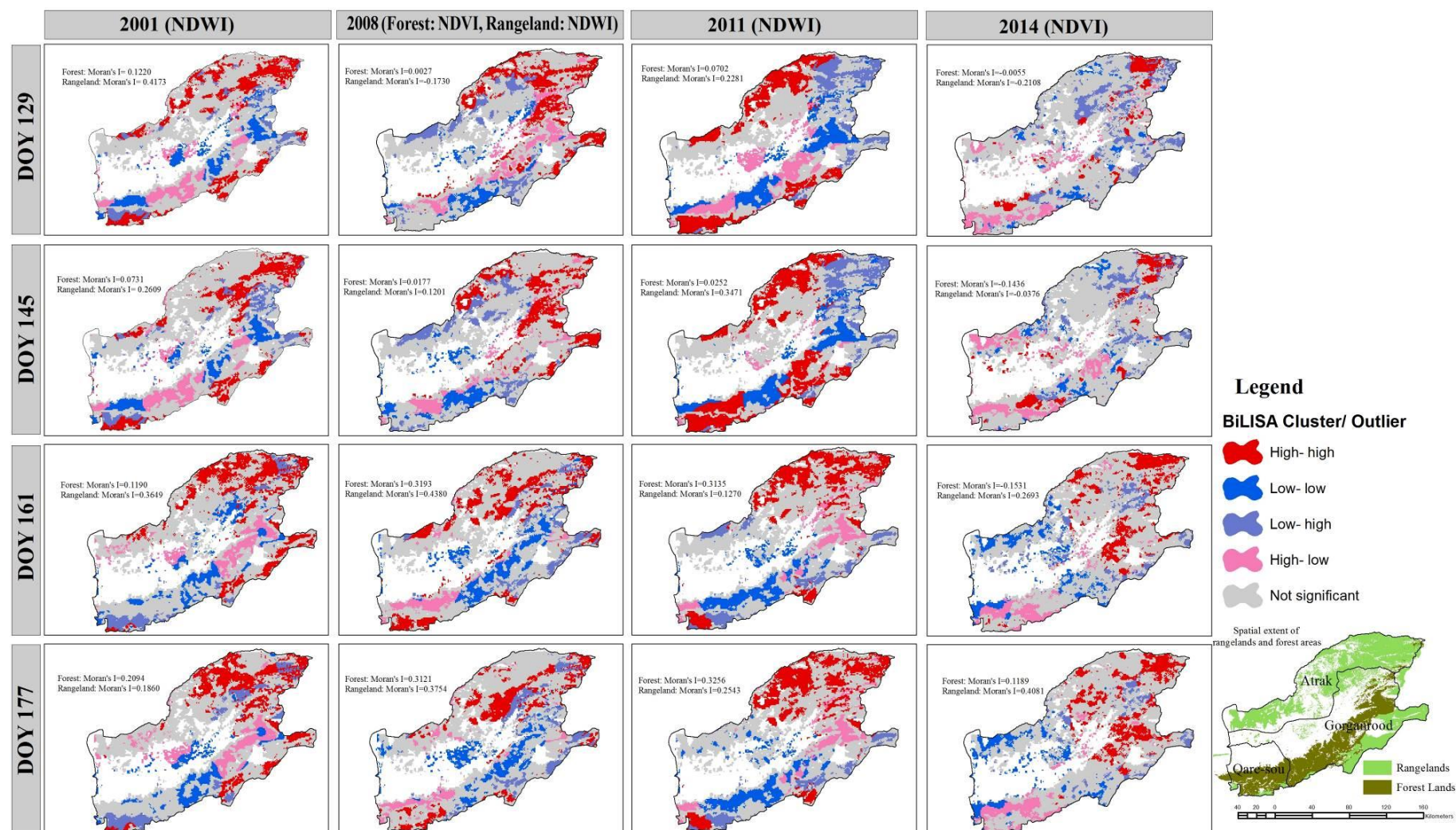


**Figure 3.S2** Spatial variations of BiLISA cluster/ outlier of DOY 129 to DOY 177 during drought periods (Significance level= 0.05, Randomization permutations= 499)

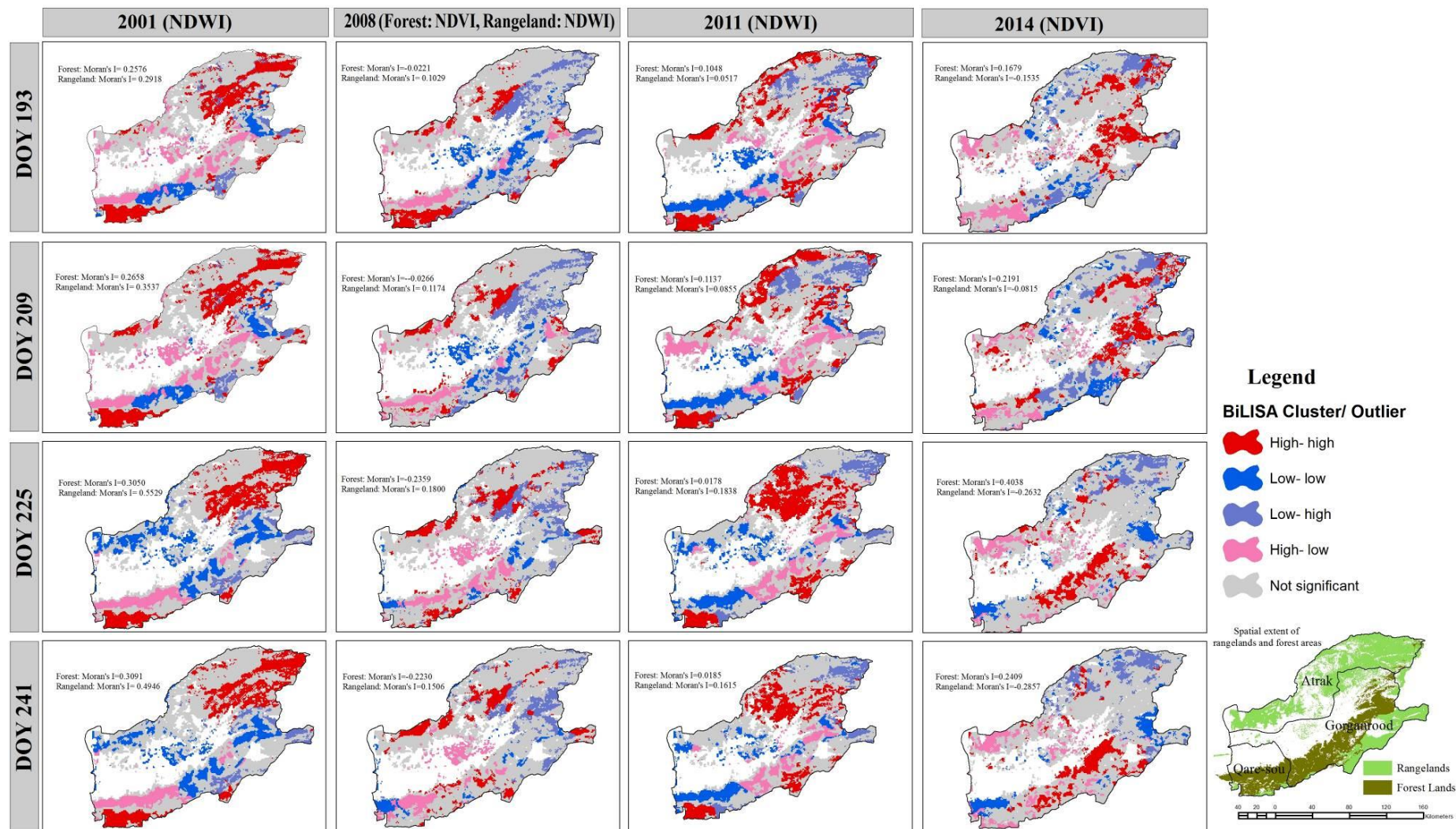


**Figure 3.S3** Spatial variations of BiLISA cluster/ outlier of DOY 193 to DOY 241 during drought periods (Significance level= 0.05, Randomization permutations= 499)



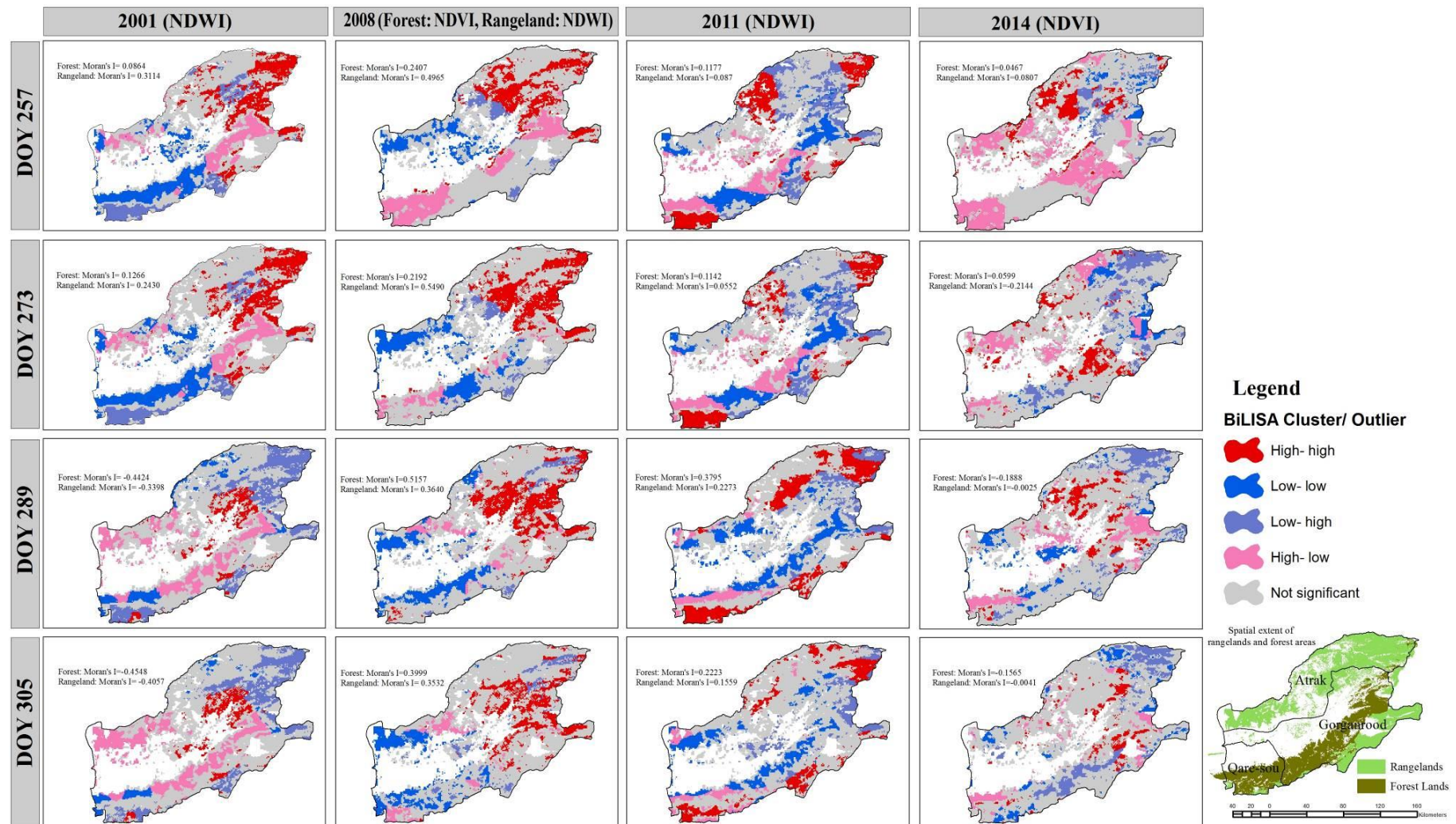


**Figure 3.S4** Spatial variations of BiLISA cluster/ outlier of DOY 257 to DOY 305 during drought periods (Significance level= 0.05, Randomization permutations= 499)



# Appendix B

## Supplementary Tables and Figures of Chapter 4

**Table 4.S1** Classification schemes of meteorological and hydrological droughts, and forest stress based on the first standard deviation.

Drought/ Stress class	SPI/ SDI	SWI	SDLST/ SNLST	SETa /SNDWI/ SNDVI
Extreme	$Y \leq -2.00$	$Y \geq 2.00$	$Y \geq 2.00$	$Y \leq -2.00$
Severe	$-2.00 < Y \leq -1.50$	$1.50 \leq Y < 2.00$	$1.00 \leq Y < 2.00$	$-2.00 < Y \leq -1.00$
Moderate	$-1.50 < Y \leq -1.00$	$1.00 \leq Y < 1.5$	$0.50 \leq Y < 1.00$	$-1.00 < Y \leq -0.50$
Mild	$-1.00 < Y < 0.00$	$0.00 \leq Y < 1.00$	$0.00 \leq Y < 0.50$	$-0.50 < Y < 0.00$
No	$0.00 \leq Y$	$0.00 > Y$	$0.00 > Y$	$0.00 \leq Y$

*Note.* SPI: standardized precipitation index; SDI: streamflow drought index; SWI: standardized water level index; SDLST: standardized-daily land surface temperature; SNLST: standardized-nightly land surface temperature; SETa: standardized actual evapotranspiration; SNDWI: standardized normalized difference water index; SNDVI: standardized normalized difference vegetation index.

**Table 4.S2** The values of test parameters for diagnosing of spatial dependence of regression models.

Test	Model I	Model II	Model III	Model IV	Model V	Model VI
Lagrange Multiplier (lag)	1704.52**	655.21**	5.6279*	5.2181*	2.7132 <sup>ns</sup>	13.1464**
Robust LM (lag)	7.0435**	2.0355 <sup>ns</sup>	2.790 <sup>ns</sup>	0.8708 <sup>ns</sup>	0.0073 <sup>ns</sup>	1.3842 <sup>ns</sup>
Lagrange Multiplier (error)	1915.06**	756.49**	2.8611 <sup>ns</sup>	5.7035*	7.6548**	16.6453**
Robust LM (error)	217.58**	103.32**	0.0232 <sup>ns</sup>	1.3562 <sup>ns</sup>	4.9489*	4.8832*

*Note:* \*\* p value < 0.01, \* p value < 0.05, and ns: not significant. Model I and II: spatial dependence between the hazard intensity of forest drought based on the NDWI and NDVI with meteorological and hydrological droughts; Model III to Model VI: spatial dependence between the diversity of tree mortality from low to high diebacks with the hazard intensity of forest drought.

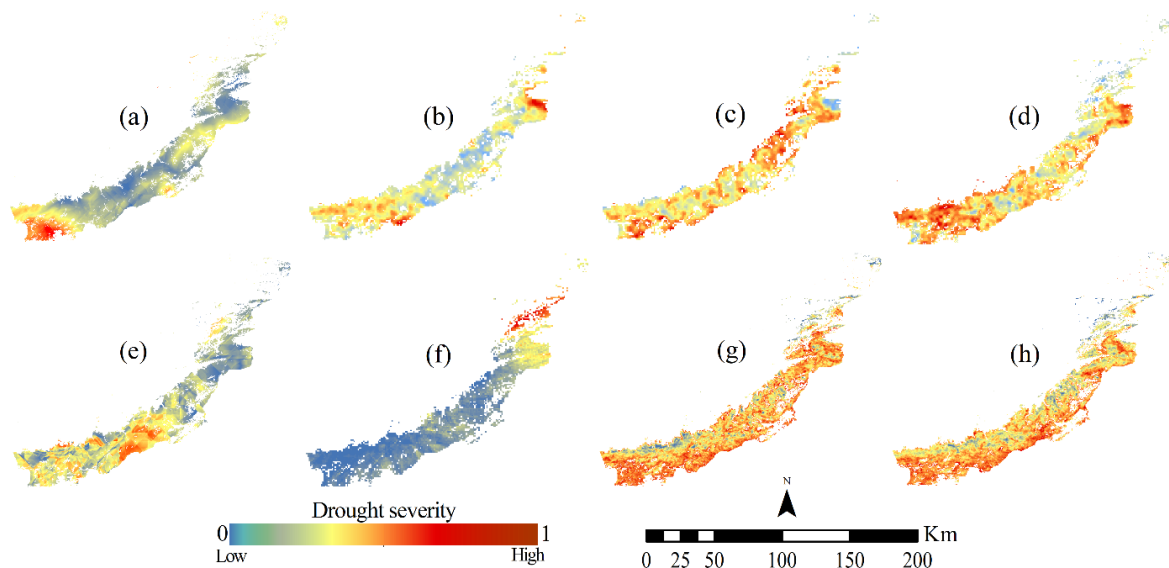


**Figure 4.S1** Spatial variations of the drought severity show that the higher values of negative anomalies are observed in the ETa (d), night-time LST (c), day-time LST (b) and the precipitation (a) among meteorological variables. The water surface anomaly (e) recorded higher negative values in comparison to the groundwater anomaly (f). Forest drought based on the normalized difference water index (NDWI) (g) was severe than forest drought based on the normalized difference vegetation index (NDVI) (h) in northeastern Iran.

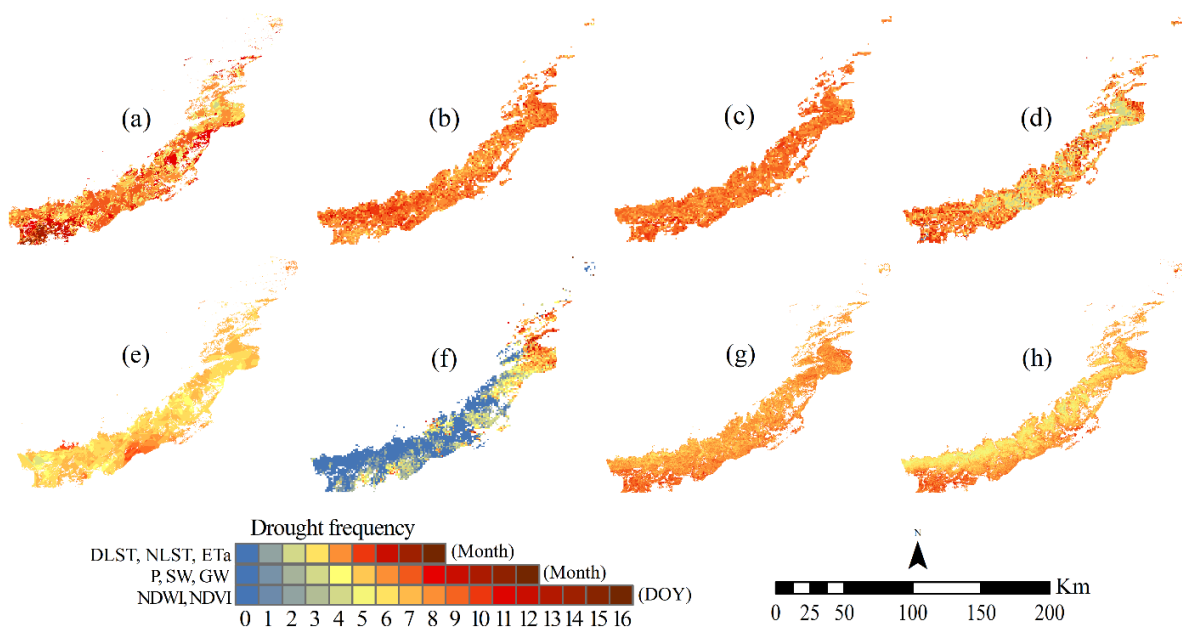


**Figure 4.S2** Spatial variations of the drought frequency of the meteorological droughts: the precipitation (P) (a), day-time LST (DLST) (b), night-time LST (NLST) (c), and the ETa (d); the hydrological droughts: the surface water (SW) (e) and groundwater (GW) (f) levels; and the forest droughts: the deficit of water-content (NDWI) (g) and loss of the greenness (NDVI) (h) during a hydrological year (from October of the previous year to September of the current year/ growing season (March–October) in northeastern Iran.



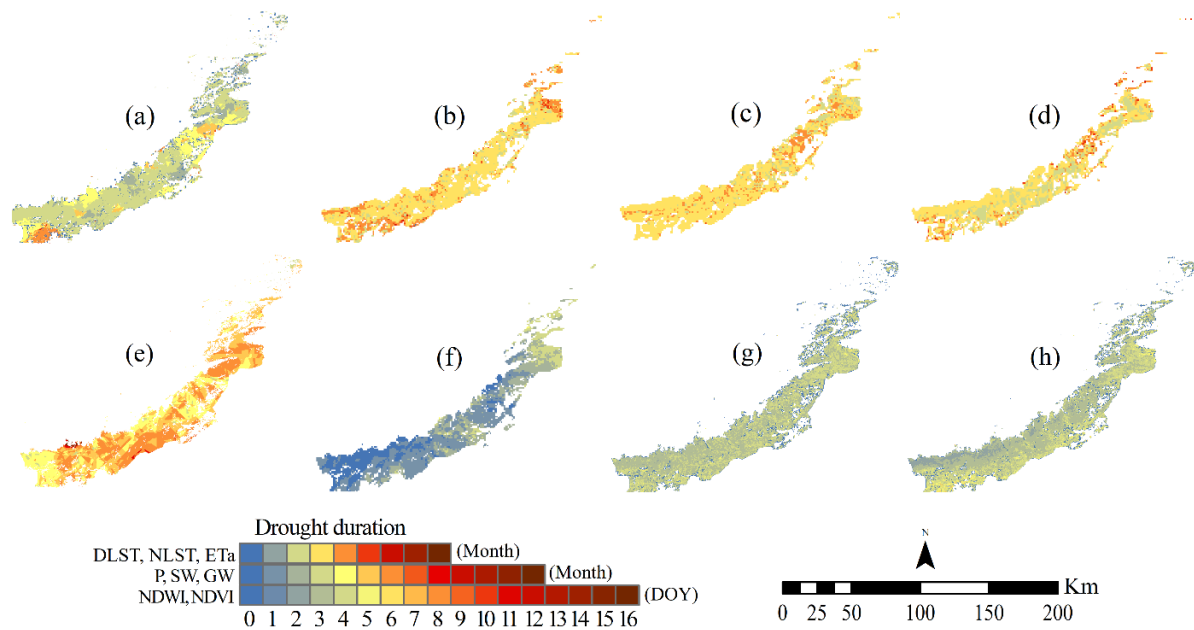


**Figure 4.S3** Spatial variations of the drought duration of the meteorological droughts: the precipitation (P) (a), day-time LST (DLST) (b), night-time LST (NLST) (c), and the ETa (d); the hydrological droughts: the surface water (SW) (e) and groundwater (GW) (f) levels; and the forest droughts: the deficit of water-content (NDWI) (g) and loss of the greenness (NDVI) (h) during a hydrological year (from October of the previous year to September of the current year/ growing season (March–October) in northeastern Iran.